Investigation of the Spatial and Temporal Structure of Internal Waves

Andy I Pickering

A dissertation
submitted in partial fulfillment of the
requirements for the degree of

Doctor of Philosophy

University of Washington

2014

Reading Committee:

Matthew H. Alford, Chair

Michael Gregg

Luc Rainville

Program Authorized to Offer Degree:
UW School of Oceanography

University of Washington

Abstract

Investigation of the Spatial and Temporal Structure
of Internal Waves

Andy I Pickering

Chair of the Supervisory Committee:
Professor Matthew H. Alford
School of Oceanography

A collection of field experiments and model simulations are used to investigate the spatial and temporal aspects of internal waves, with a focus on near-inertial waves and internal tides. First, the near-inertial wave field in the North Pacific is investigated using an array of 5 profiling moorings and shipboard ADCP transects. The ship transects reveal the horizontal structure of near-inertial shear, which is coherent over large distances ($\sim$ 80km) and exhibits a change in character crossing 28.9^{o}N. Second, the spatial structure of internal tidal beams is studied with repeated shipboard ADCP transects across Kaena Ridge, Hawaii. Harmonic fits are used to isolate the M_2 component of velocity, revealing a beam structure that compares well with theoretical ray paths and numerical simulations. Third, internal tides are investigated with moorings deployed in Luzon Strait, a major internal tide generation site with complex bathymetry and mesoscale variability. The coherence of internal tides over 4 spring-neap tidal cycles is quantified, and a model is used to diagnose the mechanisms responsible. Intrusions of the Kuroshio current shift large-scale patterns of internal tide pressure, leading to lower coherence and possibly affecting the wave field radiated from Luzon Strait. Finally, the turbulent mixing caused by tidal flow over topography in southern Luzon Strait is investigated with a profiling mooring and model simulations. Depth-integrated turbulent dissipation varies by an order of magnitude between spring and

neap tides. Model simulations show that turbulence is due to the formation and breaking of lee waves. Dissipation varies for similar barotropic forcing over the 50 day record, suggesting that mesoscale variability is important in modulating mixing.

TABLE OF CONTENTS

LIST OF FIGURES

LIST OF TABLES

ACKNOWLEDGMENTS

I wish to express my sincere appreciation to my advisor Matthew Alford. He always supported me and challenged me to do my best work. I have learned a great deal about how to be a better scientist and colleague, and this work would not have been possible without him. I would also like to thank my committee members Mike Gregg, Luc Rainville, James Murray, James Riley, and Eric D'Asaro for their support and insight.

The data used in these analyses were collected during multiple research cruises ranging from a few days to almost 40 days in length. These cruises and the successful measurements would not have been possible without the help of a huge number of crew members, engineers, scientists, students, and volunteers. I have included specific acknowledgements at the end of each chapter, and apologize in advance to anyone I may have omitted.

Finally, I would like to thank Kate Allstadt, by best friend and soulmate. I could not have done this without her constant support and encouragement through both good and bad times.

DEDICATION

To my parents who instilled in me a passion for learning and gave me the tools to succeed.

Chapter

INTRODUCTION

Internal waves, supported by the oceans density stratification, provide energy pathways from large-scale forcing to mixing and dissipation of energy at smaller scales. Locally, breaking internal waves can mix heat, salt and nutrients. They are also thought to provide a large fraction of the energy required to maintain the ocean's abyssal stratification and overturning circulation (Munk and Wunsch, 1998). The magnitude and location of mixing has been shown to impact the large-scale ocean circulation in general circulation models (Jayne, 2009; Melet et al., 2013a). However, this mixing and associated dissipation largely occurs on small scales not resolved by climate-scale models, and must be parameterized. A better understanding of processes affecting internal waves and associated mixing and dissipation is crucial in order to develop accurate parameterizations. This thesis focuses on two of the most energetic parts of the internal wave spectrum, near-inertial waves and internal tides.

1.0.1 Near-Inertial Waves

Near-inertial waves are internal waves with frequency close to the local inertial frequency, which varies with latitude as $f = 2\Omega \sin(\phi)$ where Ω is the Earth's rotation rate and ϕ is the latitude. They are limited to frequencies between f and N, where $N^2 = -\frac{g}{\rho_o}\frac{d\rho}{dz}$ is the stratification. Since f increases with latitude, near-inertial waves are generally limited from propagating poleward. One of the main sources of near-inertial waves is wind forcing at the surface (D'Asaro et al., 1995). The amount of energy input from wind to near-inertial motions can be estimated with slab models (D'Asaro, 1985). Global estimates for this energy input range from 0.3-1.4 TW (Watanabe and Hibiya, 2002; Alford, 2003b; Jiang et al., 2005), a

considerable fraction of the estimated 2 TW required to maintain the overturning circulation (Munk and Wunsch, 1998). However, the fraction of this energy that actually penetrates to depth is less well known. In addition to wind forcing, a variety of other mechanisms can generate near-inertial waves, including instabilities of the internal tide (MacKinnon and Winters, 2005), adjustment of fronts (Alford et al., 2013), and geostrophic flow over bottom topography (Nikurashin and Ferrari, 2010) . Chapter 2 investigates several aspects of near-inertial waves using data from an array of profiling moorings and shipboard transects during the Internal Waves Across the Pacific (IWAP) experiment north of Hawaii. Specifically, we compute low-mode near-inertial energy flux, examine the horizontal structure of near-inertial waves, and estimate the propagation directions of a set of near-inertial waves, expanding our understanding of this portion of the internal wave spectrum.

1.0.2 Internal Tides

Internal tides are internal waves at tidal frequencies, created when the barotropic tides force stratified water over undersea topography. Their generation depends on the barotropic flow, stratification, and topographic slope (Garrett and Kunze, 2006). Conversion of barotropic to baroclinic energy, which can be inferred from barotropic tidal models constrained with satellite altimetry, is concentrated at a small number of hotspots globally (Egbert and Ray, 2003). These regions are confirmed as internal tide generation sites by models Simmons et al. (2004) and observations such as the Hawaiian Ocean Mixing Experiment (HOME) (Rudnick et al., 2003).

Close to generation sites, internal tides have a beam-like structure formed by the superposition of many different modes (Martin and Rudnick, 2007; Cole et al., 2009). In chapter 3 repeated shipboard ADCP transects are used to study the spatial structure of these internal tide beams at Kaena Ridge, Hawaii. However, most of the of the energy transferred to internal tides at these locations goes into the lower modes, which can radiate far away from

the source. The fate of these low-mode waves is an open question; they may dissipate or scatter to higher modes in the basins, or shoal on distant continental slopes.

Although the astronomical forcing that generates internal tides is periodic and known precisely, changes in background stratification and currents introduce variability into internal tide generation and propagation. Remote internal tides can increase or decrease generation depending on their phasing with the local forcing (Kelly and Nash, 2010; Zilberman et al., 2011). Mesoscale eddies and currents can also alter generation, or affect the propagation of internal tides (Rainville and Pinkel, 2006b). Luzon Strait, where strong BT tides flow across two steep submarine ridges, is another major internal tide generation site. Frequent intrusions of the Kuroshio current make Luzon Strait an ideal setting to study the effects of mesoscale variability on internal wave generation, propagation, and dissipation. In chapter 4, internal tides in Luzon Strait are investigated with a combination of mooring and model data. In particular we focus on the coherence of the signals over several spring-neap cycles, and use a model to diagnose mechanisms leading to incoherence.

In the final chapter, we examine a mechanism that dissipates some energy locally in Luzon Strait. Tidal flow over sloping topography generates lee waves that become trapped and break, leading to turbulence and mixing (Legg and Klymak, 2008; Buijsman et al., 2012; Alford et al., 2014). Temperature, salinity, and velocity are observed from a profiling mooring, and turbulent dissipation is computed from the size of density overturns. Model simulations of the region confirm lee wave formation and show that flow over the slope is 3-dimensional and asymmetric, such that it would be difficult to estimate dissipation via existing 2-D parameterizations. The magnitude of turbulence varies for similar barotropic forcing, suggesting that mesoscale fields have an effect on lee wave formation and the resultant mixing.

Chapter

THE NEAR-INERTIAL WAVE FIELD OBSERVED DURING THE IWAP EXPERIMENT

2.1 Abstract

The near-inertial shear and strain field is examined in the upper 1400 m of the North Pacific during late spring with an array of 5 profiling moorings and shipboard transects spanning 25-37°N. The measurements were aligned with a strong beam of internal tidal energy propagating Northeast from the Hawaiian Ridge, but strong near-inertial motions were also observed. Shear in the upper 1400m was dominated by numerous high-mode ($\lambda_z \approx 250m$) near-inertial waves with upward- and downward propagation. Shipboard transects demonstrate that much of the near-inertial shear associated with these waves is laterally coherent over large distances ($O(80)$km). Depth-integrated near-inertial energy flux in modes 1 and 2 is northward at moorings below the diurnal turning latitude, where it is likely dominated by the diurnal internal tide. North of the turning latitude, near-inertial energy flux is equatorward, consistent with theory. However, when wavenumber, amplitude, and propagation directions of higher mode waves are computed by applying a plane-wave fitting technique to shear and strain, a variety of propagation directions are seen. Some waves propagate northward and a number of high-mode near inertial waves propagate upward in depth, suggesting they have a deep source rather than generation by wind-forcing at the surface.

2.2 Introduction

Near-inertial waves (NIW), internal waves with frequency near the local inertial frequency f, are one of the most energetic bands of variability in the ocean. Their tendency to dominate

the frequency spectrum of shear makes them potentially important in mixing both the deep and shallow ocean, but where and when this mixing occurs is not well known. Along with internal tides, near-inertial waves are thought to provide a large portion of the energy required to maintain the ocean's overturning circulation (Munk and Wunsch, 1998). Although ubiquitous in the ocean, the source of the near-inertial peak is still not completely understood. There are numerous possible generation mechanisms and sources of near-inertial energy, and their relative importance is not well known. Here we report observations of near-inertial waves from the Internal Waves Across the Pacific Experiment (IWAP) (Alford et al., 2007), investigating their amplitude, wavenumber, propagation directions, and other characteristics with the goal of better understanding their behavior over a wide latitude range in an area with variable bathymetry. The long term goal is to better understand how and where they are generated, where they propagate, and the ultimate fate and effects of the energy they carry.

One of the most well-known generation mechanisms is by wind forcing at the ocean surface. Wind-forced NIW arise when traveling storms set up inertially rotating motions in the mixed layer (D'Asaro, 1985). Spatial variability in the wind, mesoscale flows (Weller, 1982) and the β effect (D'Asaro, 1989) subsequently create sufficiently large lateral gradients in the mixed-layer flows to "pump" slightly superinertial motions below the mixed layer. Energy input from the wind to near-inertial motions during IWAP, estimated by a slab model (D'Asaro, 1985; Alford, 2001b) forced with National Centers for Environmental Prediction (NCEP) winds (Kalnay et al., 1996), was small compared to wintertime forcing, but increases poleward (Figure 2.1). The modal distribution of these motions depends on the stratification during the storm, but much of the energy is generally in low modes (D'Asaro and Perkins, 1984; Alford, 2010), which propagate large distances toward the equator (Alford, 2003a). Because these low modes travel quickly and have less shear, this energy presumably dissipates far from the storm that generated it, though the exact fate is unknown.

Another possible source of NIW is from Parametric Subharmonic Instability (PSI) of the internal tide, which generates two waves with half the frequency (Müller et al., 1986). For semidiurnal tides, this is possible at or equatorward of the "critical latitude," 28.8^o, and expected to be more efficient at the critical latitude λ_c where the inertial frequency is exactly half the M2 tidal frequency (MacKinnon and Winters, 2005; Simmons, 2008; Carter and Gregg, 2006; Alford et al., 2007). The observations reported on here span λ_c and were collected in part to observe this process. MacKinnon et al. (2013) concluded that PSI does occur, but at a lower rate than originally predicted.

In addition to the low modes, downward-propagating near-inertial motions with smaller vertical scales ($\lambda_z \approx 100 - 400$m) and higher shear are often observed in the upper ocean and attributed to wind forcing during storms (Pinkel, 1985; Hebert and Moum, 1994; Alford and Gregg, 2001; Alford, 2010). They propagate much more slowly than low modes and contain less energy. However, their high shear makes them potentially more susceptible to breaking and hence important for mixing. Energy input from the wind to near-inertial motions has been estimated globally (Alford, 2001b), though the fraction of that energy that penetrates to depth where it contributes to abyssal mixing is not well known. Some models have predicted the fraction to be small (Furuichi et al., 2008), although analysis of deep current meter records detected a seasonal cycle in near-inertial energy (Alford and Whitmont, 2007).

Recent observations also show upward propagating near-inertial waves at all depths (Alford, 2010). The source of these upward propagating waves is a mystery; they are likely not wind generated, as high-mode waves would not be expected to propagate that far and reflect off the bottom before dissipation. It is possible that some of these are generated at depth by PSI; another possible deep source of near-inertial motions is generation by geostrophic flows over bottom topography (Nikurashin and Ferrari, 2010).

Understanding the fate of both the low- and high- wavenumber aspects of the spectrum is an active area of research, with the ultimate goal of determining the degree and the

spatial distribution of mixing by NIW. As a step toward this goal, we report observations of NIW during the IWAP experiment (Alford et al., 2007). The experiment was designed to observe the propagation of internal tides northward from Hawaii, but also provided an opportunity to study and document numerous NIW. The depth coverage of the moorings allows us to compute the low-mode near-inertial energy flux. Simultaneous strain and shear measurements over a large depth range (100-1400m) allow calculation of individual wave properties including propagation directions, and spatial transects measure the horizontal structure of these waves.

In the following sections, we first outline the oceanographic context and data. An overview of the data and basic results are presented in section 4, including the raw and bandpass filtered shear and strain data from all moorings and frequency spectra of shear and strain. Section 5 focuses on the low-mode energy flux. In section 2.6 we present shipboard transects showing the horizontal spatial structure of near-inertial waves and their coherence over large distances. In section 2.7 we study the characteristics of higher-mode waves using a plane wave fitting method, and estimate their propagation directions from the phase between shear and strain. We end with a discussion and conclusions.

2.3 Oceanographic Setting and Data

The Internal Waves Across the Pacific (IWAP) experiment (Figure 2.1) was designed to examine the northward progression of internal tide energy from its generation region near French Frigate Shoals, Hawaii, past the critical latitude, and beyond. The experiment took place in two cruises spanning about 62 days from April to June, 2006. The general approach was to obtain simultaneous spatial and temporal information by steaming along the main line with the Hydrographic Doppler Sonar System (HDSS), a specialized, high-power Doppler sonar, while six moorings spaced along the line (MP1-MP6) sampled to ascertain temporal information. MP5 malfunctioned and is not included in this analysis. Analyses of internal

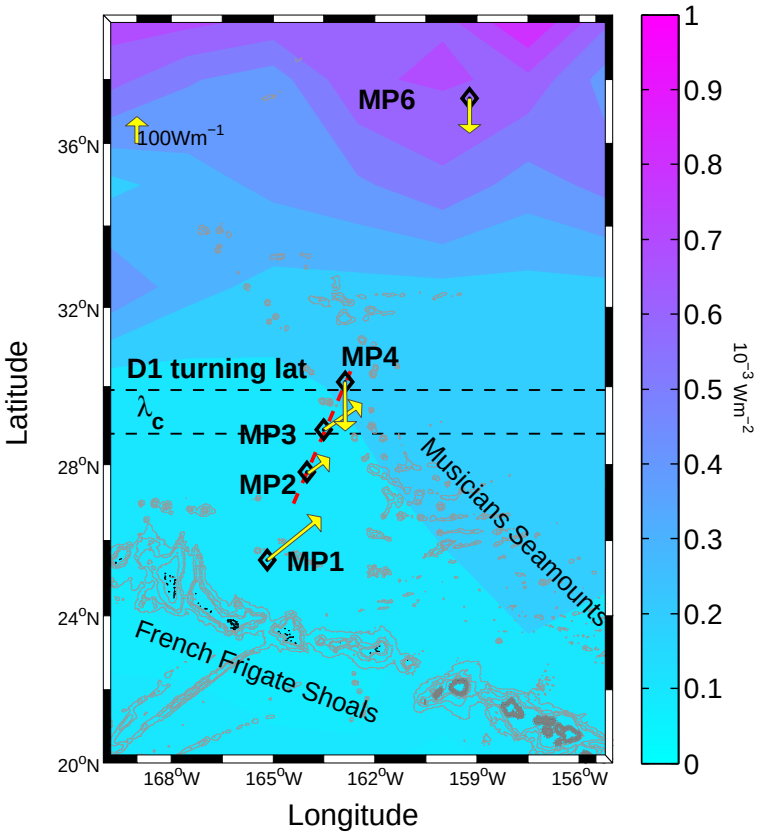

Figure 2.1: Location of IWAP moorings (black diamonds). Isobaths are contoured every 1000m from 0 to 4000m. Background color is the time-mean flux (10^{-3}Wm^{-2}) from the wind to near-inertial motions during the experiment, estimated from the Pollard and Millard (1970) slab model (see discussion). Yellow vectors show the time-mean depth-integrated near-inertial energy flux measured at the moorings. The 'critical latitude' λ_c and the diurnal turning latitude are indicated on the map. Red line shows extent of shipboard transects discussed in text.

tides during IWAP are reported in Alford et al. (2007), Zhao et al. (2010) and MacKinnon et al. (2013); this paper focuses on the near-inertial signals. Besides the Hawaiian Ridge, the bathymetry in the area includes large areas of rough bottom topography, notably the Musicians seamounts (Figure 2.1). Wind forcing during the experiment is characterized with the Pollard-Millard Slab model. The model is forced with 6-hr NCEP reanalysis winds. Wind forcing during the experiment was relatively weak, and increases poleward as expected.

2.3.1 Moored Array

Five moorings of similar design were deployed spanning latitudes 25-37°N. At 3000 m, an Aanderaa RCM8 current meter measured horizontal velocity every 10 minutes, and a Sea-Bird temperature logger measured temperature every 30 seconds. High wire tension ($\approx$ 500 kg) together with generally weak currents ensured mooring knockdown was less than 20 m at all sites.

The primary measurement on each mooring was a McLane Moored Profiler (MP), which climbed up and down through the water column along the mooring wire between 85 and 1400 m, completing one up or down profile each 1.5 h. Each MP carried a Falmouth Scientific CTD with vertical resolution of 2 m and a Neil Brown acoustic current meter with vertical resolution of about 10 m and precision of about 1cm/s, delivering profiles of density and velocity (Doherty et al., 1999; Silverthorne and Toole, 2009; Alford, 2010). The sawtooth pattern traced by the MP leads to a variable temporal resolution ranging from 3 hours at 85 and 1400 m depth to 1.5 hours at mid-depths. This is easily sufficient to resolve near-inertial motions, which have a period ranging from 20 to 28 hours over the latitude range of the moorings.

2.3.2 Hydrographic Doppler Sonar System

Spatial transects of velocity and shear ($\partial\vec{u}/\partial z$) in the upper 1000 m were measured along the mooring line with the HDSS Doppler sonar system. HDSS consists of a 140-KHz and a 50-KHz Doppler sonar reaching depths of approximately 250 and 1000 m, respectively. Velocity from the two sonars was merged and gridded in 8-m, five-minute bins (1.2 km horizontal resolution at a ship's speed of 4 m/s).

Velocity estimates from shipboard Doppler sonar systems are subject to errors at a strong intensity gradient (King et al., 2001, see also `http://currents.soest.hawaii.edu/reports/hdss_2006/hdss2006_report.html`). Biasing of the acoustic returns in the high-gradient region leads to a spurious signal in along-ship velocity. This signal is proportional to the ship speed and degree of pitching. The effect is problematic for much of the data collected while steaming at 12 knots (6 m/s), manifesting as a false shear layer at a depth of about 400 m. We therefore restrict analysis here to periods when the ship was steaming at only 7-8 knots (3.5-4 m/s) and the effect was negligible.

2.4 Overview of Mooring Data

2.4.1 Depth-time Data

We first examine depth-time maps of shear (Figure 2.2) and strain (Figure 2.3). Both are depth-derivatives, which emphasize the higher-mode features with shorter vertical wavelengths. Strong shear is seen at all moorings and all depths, displaying both upward and downward phase propagation. To isolate the near-inertial components, a fourth-order bandpass filter with a pass-band of [0.7-1.3]$\times f$ is applied. Depth-time maps of bandpass filtered shear at all moorings are similar in magnitude and appearance to total shear, evidence that the shear fields are dominated by near-inertial motions. Maps of near-inertial strain show

that, like shear, there appears to be a weaker underlying continuum with stronger intermittent bursts of near-inertial shear and strain that resemble plane waves over limited depth-time regions. Shear at MP3 appears qualitatively different, with large regions of 'checkerboard' shear that do not show clear upward or downward phase propagation. Alford et al. (2007) interpreted these as evidence of PSI occurring near the critical latitude. We examine low-mode fields in a later section by combining the upper-ocean observations from the MP with deeper velocity and temperature measurements.

2.4.2 Spectra

Frequency spectra of shear and strain also demonstrate the dominance of the near-inertial band (Figure 2.4). Spectra were calculated at each depth using the multi taper method (Riedel and Sidorenko, 1995), then WKB-scaled and depth-averaged. Shear and strain were WKB-scaled as

$$u_{zwkb}(z) = u_z\sqrt{N_o/\bar{N}(z)} \tag{2.1}$$

$$\gamma_{wkb}(z) = \gamma\sqrt{\bar{N}(z)/N_o} \tag{2.2}$$

respectively, where N_o is a reference buoyancy frequency (the same for all moorings) and $\bar{N}(z)$ is the time-mean stratification profile. Rotary spectra of shear at all moorings are dominated by peaks in the clockwise component around the local inertial frequency, which varies with latitude. Slight peaks are seen at the semidiurnal (M_2) frequency at some moorings. Small peaks at $f + M_2$ indicate vertical heaving of near-inertial shear by the M_2 tide (Alford, 2001a). The record length does not allow us to distinguish between diurnal and near-inertial frequencies at these latitudes. However the small expected shear of a low-mode internal tide suggests that the shear is related to NIW, not tidal signals. Additionally, MP4 and MP6 are poleward of the diurnal turning latitude, so internal tides are not expected there.

Spectra of strain (right) are also dominated by near-inertial peaks, but less so than shear, and have more significant peaks at the M_2 and $f+M_2$ frequencies. There is a slight tendency

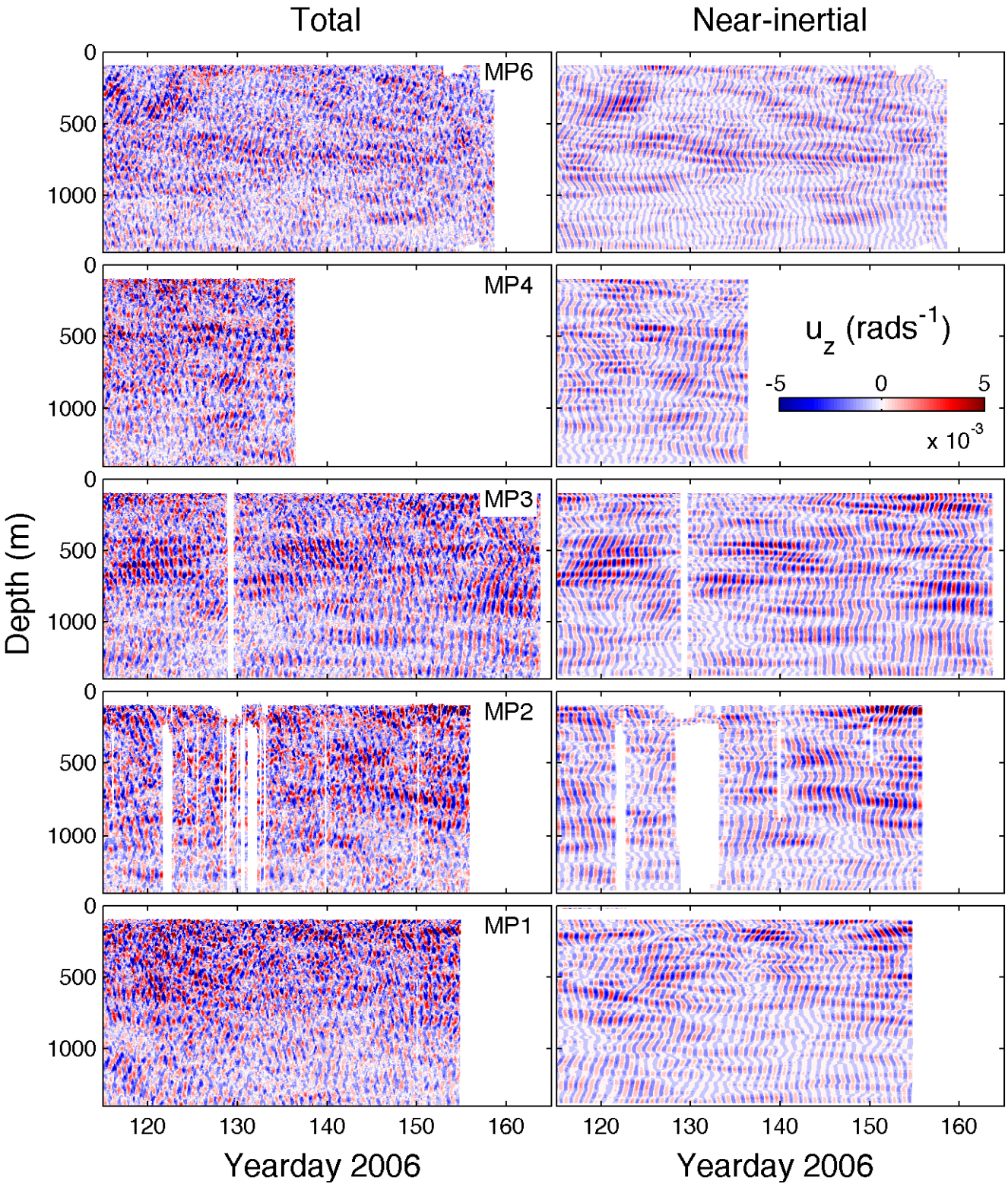

Figure 2.2: Depth-time maps of total (left) and near-inertial (right) zonal shear u_z at all moorings.

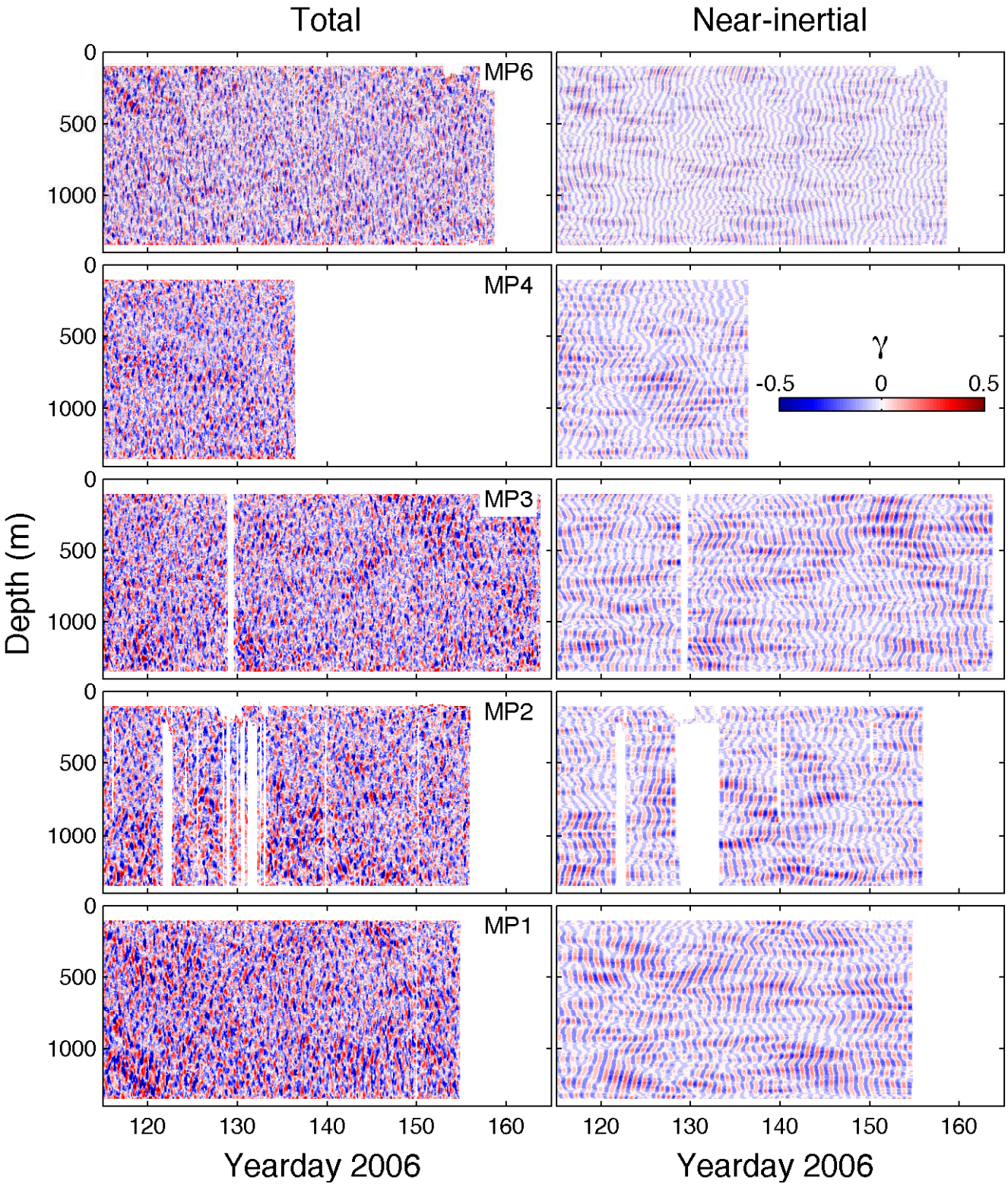

Figure 2.3: Total (left) and near-inertial (right) strain at IWAP moorings.

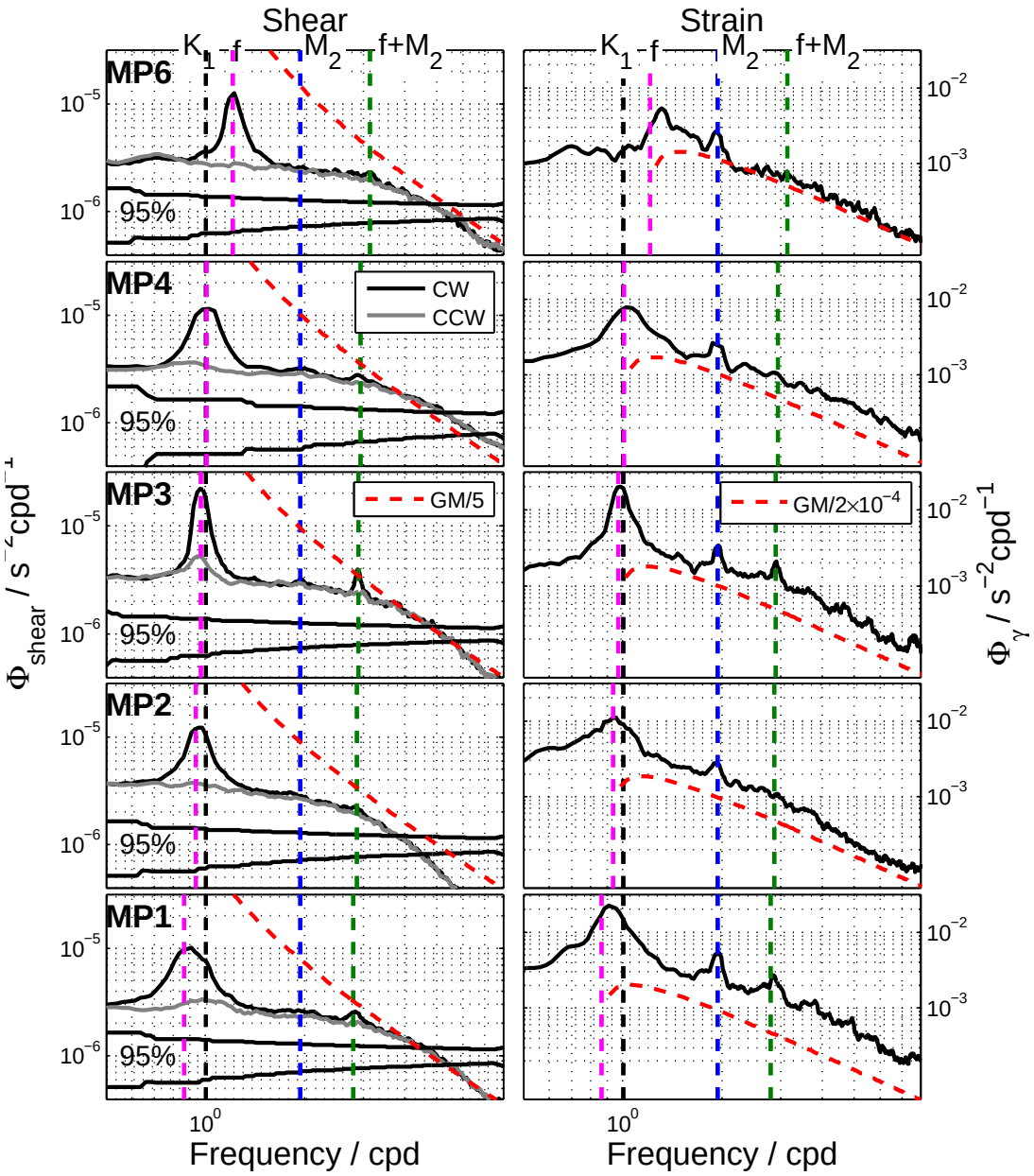

Figure 2.4: Frequency spectrum of shear and strain from all MP's. Spectra were wkb-scaled ($N_o = 0.0036\text{s}^{-1}$) and depth-averaged between 150m and 1300m. Magenta line marks the inertial frequency f. Dashed blue lines indicate the diurnal and semidiurnal tidal frequencies, as well as the sum of the inertial and semidiurnal frequencies $f + M_2$. Dashed red line on left shows the theoretical GM76 spectra for shear divided by 5. For strain on right, dashed red line is the GM76 displacement spectrum divided by 2×10^{-4}.

for the peak to lie slightly above f, which is expected since purely inertial motions would have no vertical displacement or strain. Apart from the near-inertial and tidal peaks, strain spectra fall off with a slope close to the theoretical GM76 spectrum (Garrett and Munk, 1975; Cairns and Williams, 1976). Strain levels also appear to be elevated more above GM at lower latitudes.

2.4.3 Mean Profiles of Kinetic Energy and Shear

The components of the internal waves with upward and downward energy propagation can be separated using Fourier analysis at each profile to separate the clockwise (CW) and anti-clockwise (ACW) motions (Leaman and Sanford, 1975). The time-mean profile of each is plotted in figure 2.5, together with the time-mean profile of buoyancy frequency (scaled, gray). Upward and downward shear magnitude both generally decrease with depth approximately as N. At MP6, CW shear is greater than ACW in the upper 700m, and less than ACW shear below 700m. The CW and ACW magnitudes are more similar at the other moorings, with the exception of a dominance of CW shear between 700-1100m at MP3. However, it is difficult to draw conclusions based on a short record, since the profiles can be dominated by a small number of wave 'packets' (for example the strong downward propagating between 100 and 500 m at the beginning of MP6 record).

2.5 Energy Flux

We next compute the near-inertial energy flux from bandpass filtered velocity and displacement fields. The deep velocity and temperature measurements allow us to fit the data to the first 2 vertical modes for velocity and displacement. Mode shapes are determined from the full-depth WOA climatological stratification (Levitus and Boyer, 2001), which compares well with measured stratification in the upper 100-1400m. Energy flux is then computed using standard methods (Kunze et al., 2002). Energy flux is defined as the covariance of velocity

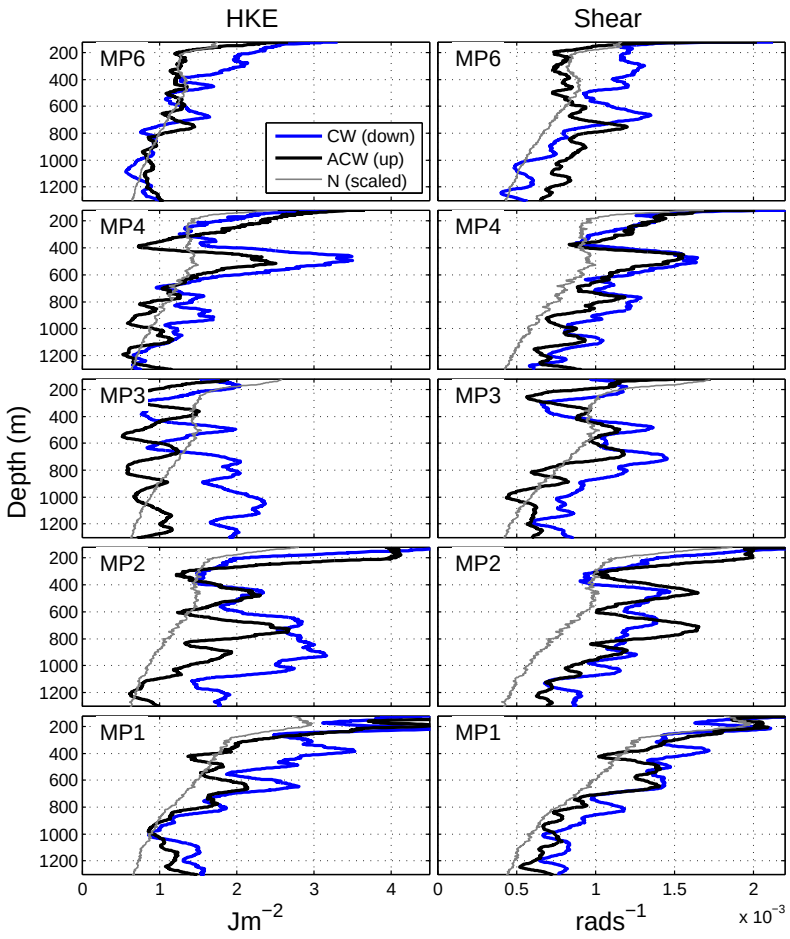

Figure 2.5: Time-mean profiles of CW (blue) and ACW (black) with depth components of horizontal kinetic energy (left) and shear (right) at IWAP moorings. Stratification, scaled to fit on the same axes, is also shown in gray.

and pressure perturbations:

$$\mathbf{F} =< \mathbf{u}'p' > \tag{2.3}$$

Perturbation pressure p' is computed as

$$p' = p_{surf} + \int_z^0 \rho' g dz \tag{2.4}$$

where the ρ' is the density perturbation.

The surface pressure p_{surf} is not measured but can be inferred from the baroclinicity condition that the depth-averaged pressure perturbation must vanish:

$$\frac{1}{H}\int_{-H}^0 p'(z,t)dz = 0 \tag{2.5}$$

We also compute the total energy flux over the upper 100-1400m measured by the MPs. The mode fits to pressure are used to determine the correct offset to use since p' cannot be integrated over the entire water column (Rainville and Pinkel, 2006a).

2.5.1 Results

Time-mean profiles of energy flux are shown in Figure 2.6, and depth-integrated values are listed in Table 2.1. The low-mode (modes 1 and 2) near-inertial energy flux is northeast at MP1-MP3 and south at MP4 and MP6. Note that the diurnal and inertial frequencies are too close at these latitudes to separate with the bandpass filter. The northeast flux at MP1-MP3 is likely dominated by the D1 internal tide propagating northward from Hawaii. However, it does not have a spring-neap cycle, possibly because the diurnal spring-neap cycle at the Hawaiian Ridge is weak. MP4 and MP6 are north of the D1 turning latitude, and the observed southward flux is likely actually near-inertial energy propagating equatorward. Profiles of total near-inertial flux are shown in blue. These include the low-mode flux, and appear similar but with more higher-mode oscillations with depth.

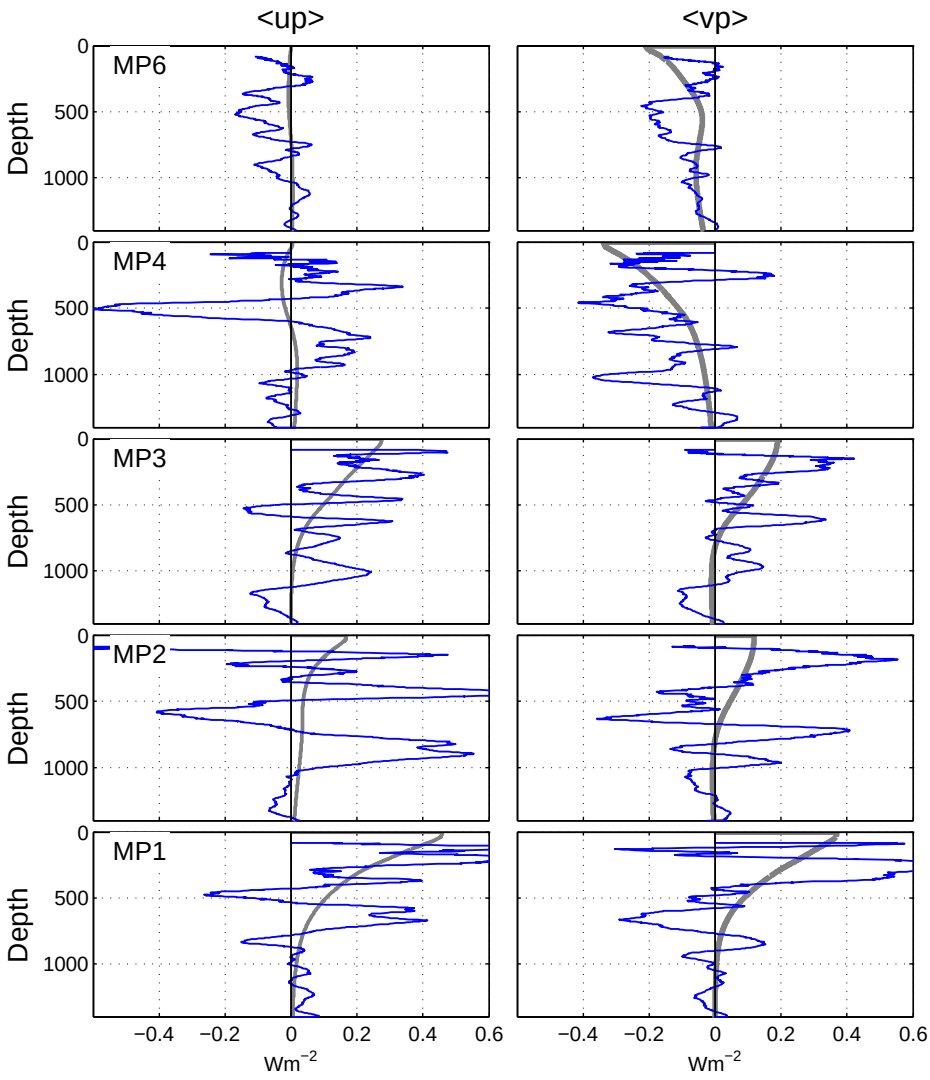

Figure 2.6: Time-mean near-inertial energy flux profiles at IWAP moorings. Gray line is the sum of modes 1 and 2. Blue is the total (not modal) energy flux; the correct p' offset is determined from the first 2 modes.

Table 2.1: Time-mean near-inertial band energy flux magnitude (F) and direction (θ) at IWAP moorings. Direction is given in degrees true (clockwise from North).

	MP1	MP2	MP3	MP4	MP6
F (Wm^{-1})	254.3	100	171.8	183.2	132.2
$\theta(^0\mathrm{T})$	51	54	55	179	180

2.6 Spatial sections and horizontal coherence

Shipboard sections of shear past the moorings provide a rare opportunity to examine the horizontal spatial structure of near-inertial waves. Profiles of velocity and shear from MP3 and the HDSS as the ship passed by the mooring (Figure 2.7) agree well, confirming that they are measuring the same features and allowing us to examine the horizontal structure of these waves. The agreement is due in part to the dominance of near-inertial waves in this region, and in part to their large horizontal scales.

Interpretation of the shipboard transects is complicated by the fact that the shear field rotates inertially as the ship steams past. Taking advantage of the observed near-inertial dominance of shear, we employ a technique known as inertial back-rotation (D'Asaro et al., 1995) to remove the rotation in time, giving a closer approximation of a spatial snapshot. If the measured shear field (written in complex notation, $w_z \equiv u_z + iv_z$) has a time and space structure given by

$$w_z(x, y, z, t) = \hat{w}_z(x, y, z)e^{-i\omega t}, \tag{2.6}$$

then multiplication by $e^{i\omega t}$ gives the backrotated field $\hat{w}_z(x, y, z)$. Backrotated shear is computed using the inertial frequency at MP3, $\omega = f(28.9^o)$. Since the correction is applied only over short intervals, the precise frequency used makes little difference. However, shear at frequencies other than f introduces errors.

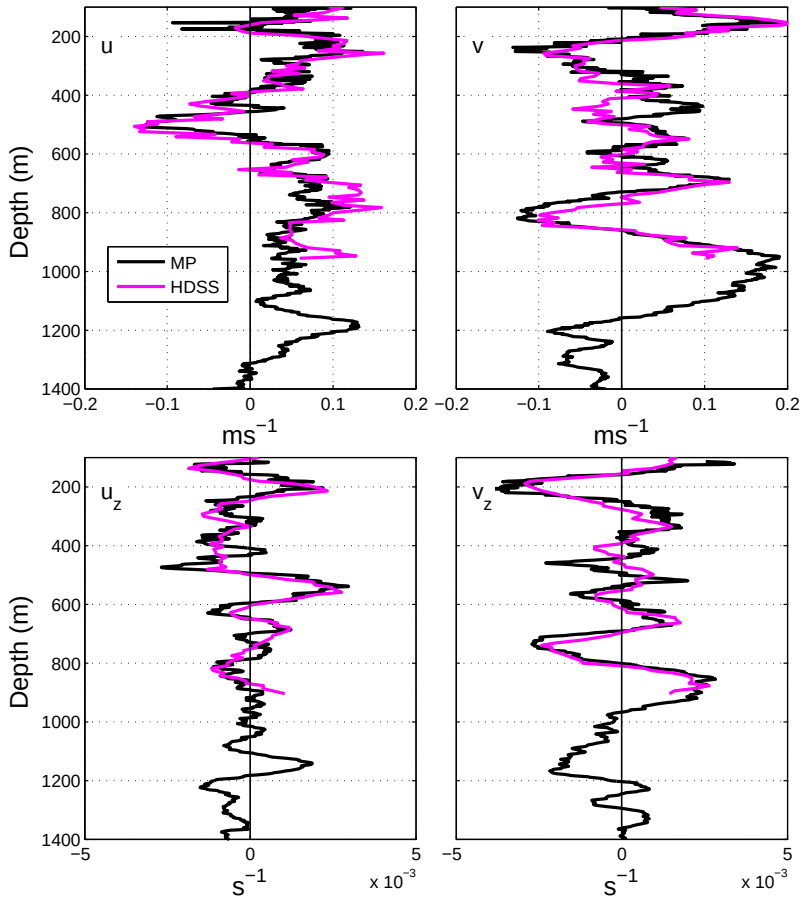

Figure 2.7: Comparison of velocity (left) and shear (right) profiles measured by moored profiler at MP3 (black) and HDSS (magenta) as ship passed the mooring. The profiles were measured on June 11 (yearday 161.84).

2.6.1 Ship Transects - Group 1

The first section of transects consisted of four transects between 27.8^{o}N and 30.4^{o}N, passing by moorings MP3 and MP4. Strong near-inertial features are seen in velocity and shear from MP3 during this time period (Figure 2.8 a,b). The backrotated shear at the moorings (c) largely consists of horizontal bands over this period, showing that the technique works to isolate the near-inertial motions. Semidiurnal oscillations of these bands shows the heaving of the near-inertial shear by the semidiurnal tide. One of the strongest features seen during this period is between 600 and 1000m, which shows dominantly upward phase propagation. Although noisier than shear, strain (d) shows a similar feature, clearest from days 159-163 and between 700 and 900m.

Spatial sections of back rotated shear past the mooring during this time show the lateral structure of these features (Figure 2.8, right), which have a variety of slopes. In spite of the vertical advection of these features by internal tides and other motions, backrotated shear at a given location remains fairly constant for most features between the successive occupations, suggesting that they are the same near-inertial features sampled multiple times. A persistent feature sloping upward to the north of MP3 is visible in all three transects, while more level or even upwards-toward-the-south features are seen to the south of MP3. Many features appear visually to be coherent over lateral scales of 50-100 km.

The upward phase propagation in time (b,d) indicates a downward propagating near-inertial wave, while the upward slope of the feature to the North also indicates that the wave direction has an equatorward component. Further evidence that the spatial features north of MP3 are associated with a downward propagating wave is obtained by separating HDSS profiles into components that rotate clockwise and counter-clockwise in depth. Based on linear wave theory, a downward propagating wave will have a velocity profile that rotates CW in depth. The upward sloping features north of MP3 are mainly associated with CW rotation (not shown), consistent with this interpretation. Theoretical internal wave ray paths

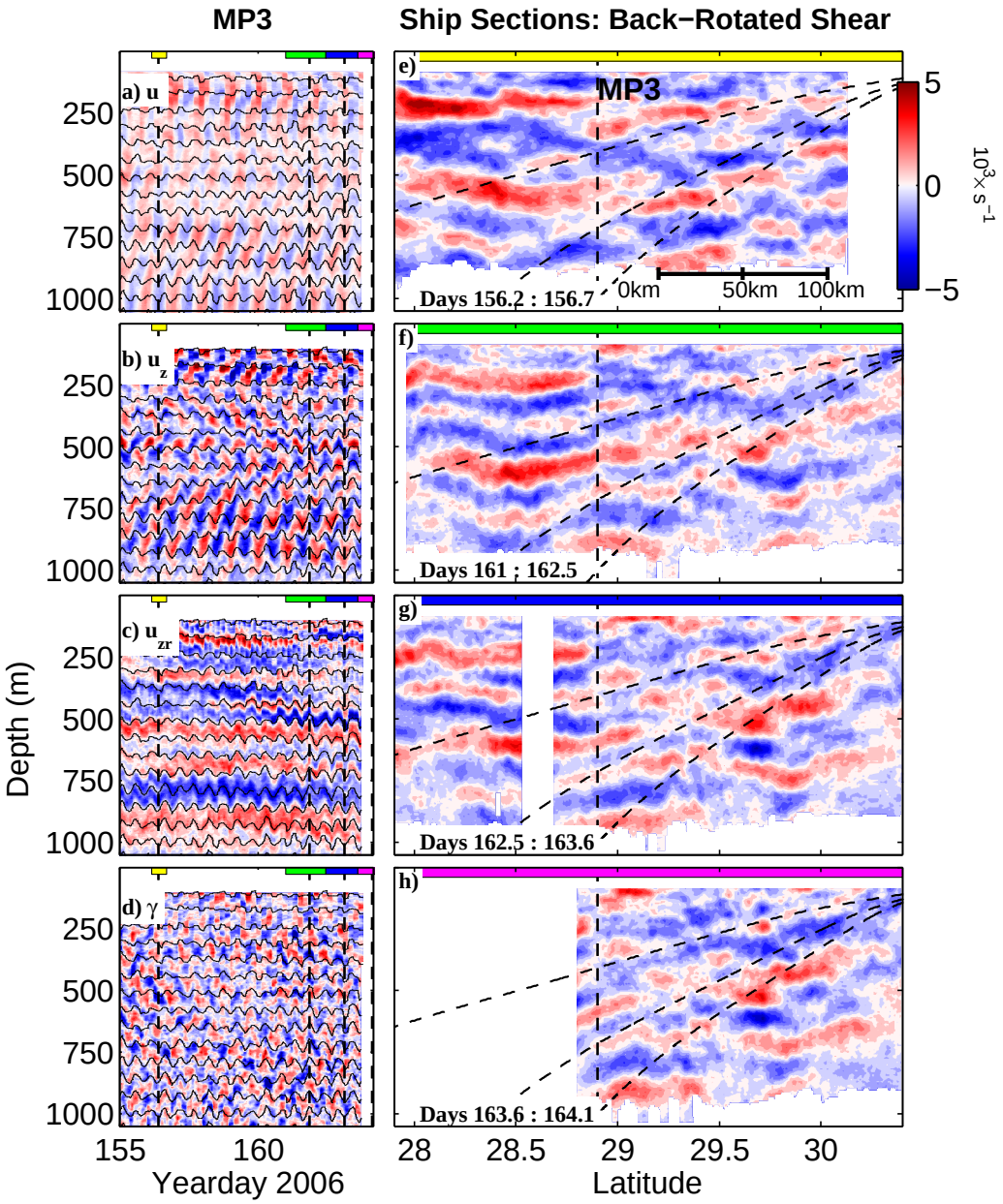

Figure 2.8: Moored data from MP3 (left), and shipboard spatial transects past MP3 (right). Left: Depth-time series of velocity, zonal shear, backrotated zonal shear, and strain. Vertical dashed lines indicate times that ship passed MP3 on each transect (leftmost corresponds to upper right panel, middle line to middle right panel, etc.). Isopycnals are plotted at 60m intervals. Right: Backrotated zonal shear measured on four consecutive shipboard transects, plotted versus latitude. Black curves are theoretical ray slopes for frequencies of ω_I = [1.01 1.03 1.05] $\times f$, using the mean N at MP3. Colored periods at the top of each ship transect correspond to time periods at of mooring panels.

were computed using the mean N at MP3. The slope of the features observed north of MP3 appears roughly consistent with a near-inertial wave with frequency $\sim 1.01 - 1.3 \times f$. The phase between shear and strain also suggests that this wave is propagating towards the southwest; this is discussed in more detail in section 6.

2.6.2 Ship Transects - Group 2

The second set of transects were made past MP2 and MP3 on year day 140 (Figure 2.9). Three of the transects spanned both moorings, while the fourth passed by MP3 only. Strong, nearly horizontal features are seen between MP2 and MP3, similar to the previous transect. The strongest features near 400-600m appear to be connected between the two moorings.

Shear at MP2 is noisier than at MP3 (possibly indicating more non-inertial motions), but generally agrees well with backrotated shear from the ship transects, notably the phase change from near 400m. Near-inertial shear at MP3 during this time is strong and checkerboard, with possibly a slight tendency for downward phase propagation. Back-rotated shear agrees well with transects in the 300-800m range, with the strongest feature near 500m.

2.6.3 Lateral Coherence

Qualitatively, many of the shear features seen in the transects appear to be laterally coherent/continuous over distances of 30-100km. To examine this more quantitatively, 2D wavenumber spectra of HDSS shear are computed from each transect. Data are interpolated to a vector of evenly-spaced horizontal distance in the direction of the transects, and the spectra are computed with a 2D Fourier transform. Spectra from both groups of transects show a broad peak centered near a vertical wavelength of 200 m and horizontal wavelength of 80 km. The spectra from the first group (Figure 2.10) are bluer than those from the second group (Figure 2.11) in horizontal wavenumber, which may be due to the sloping features present in the first group.

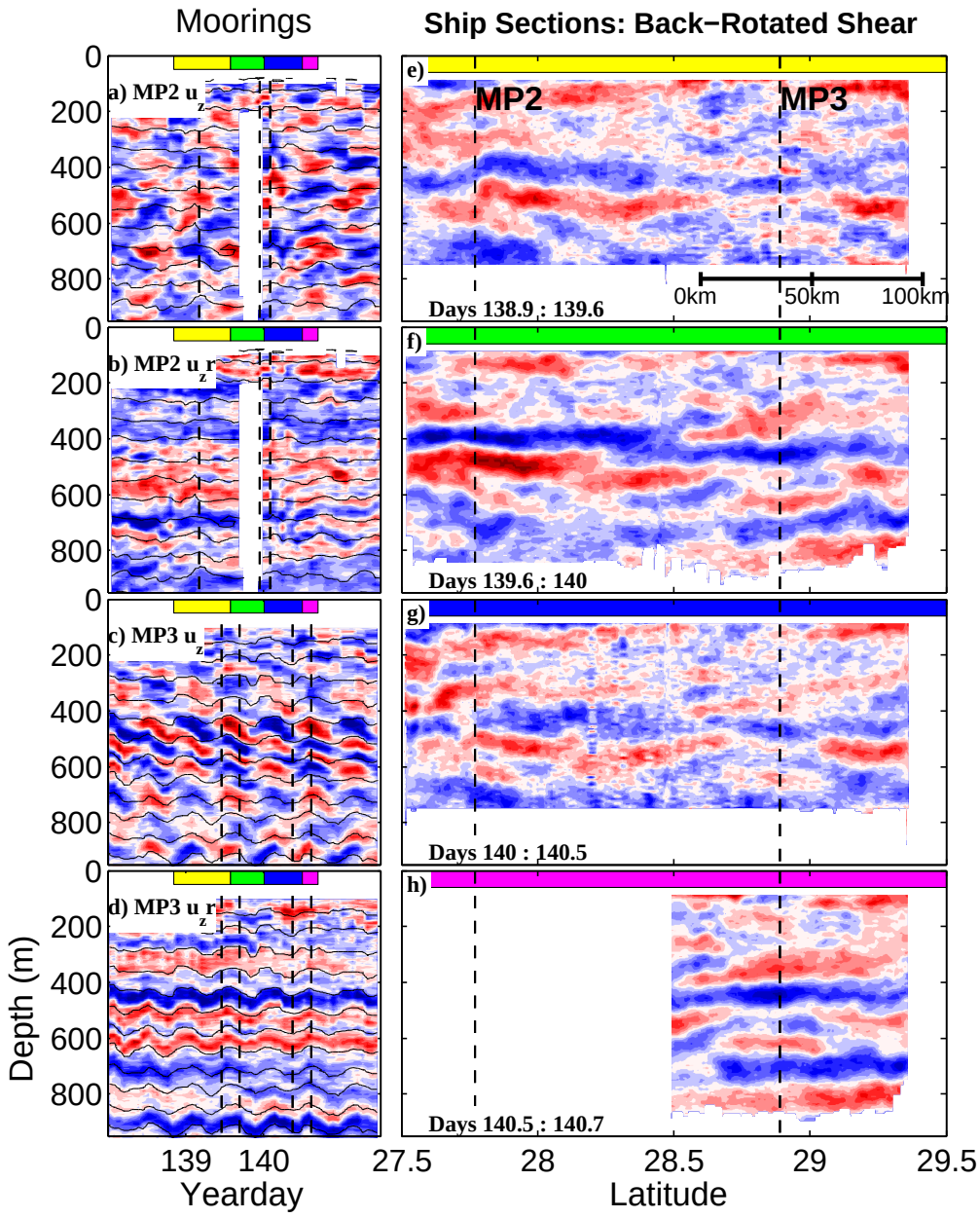

Figure 2.9: Moored data from MP2 and MP3 (left), and shipboard spatial transects past the moorings (right). Left: Time series of raw and backrotated zonal shear at MP2 and MP3. Isopycnals are plotted at 60m intervals. Vertical dashed lines indicate times that ship passed MP3 on each transect. Right: Backrotated zonal shear measured on four consecutive shipboard transects, plotted versus latitude. Colored periods at the top of each ship transect correspond to time periods at of mooring panels.

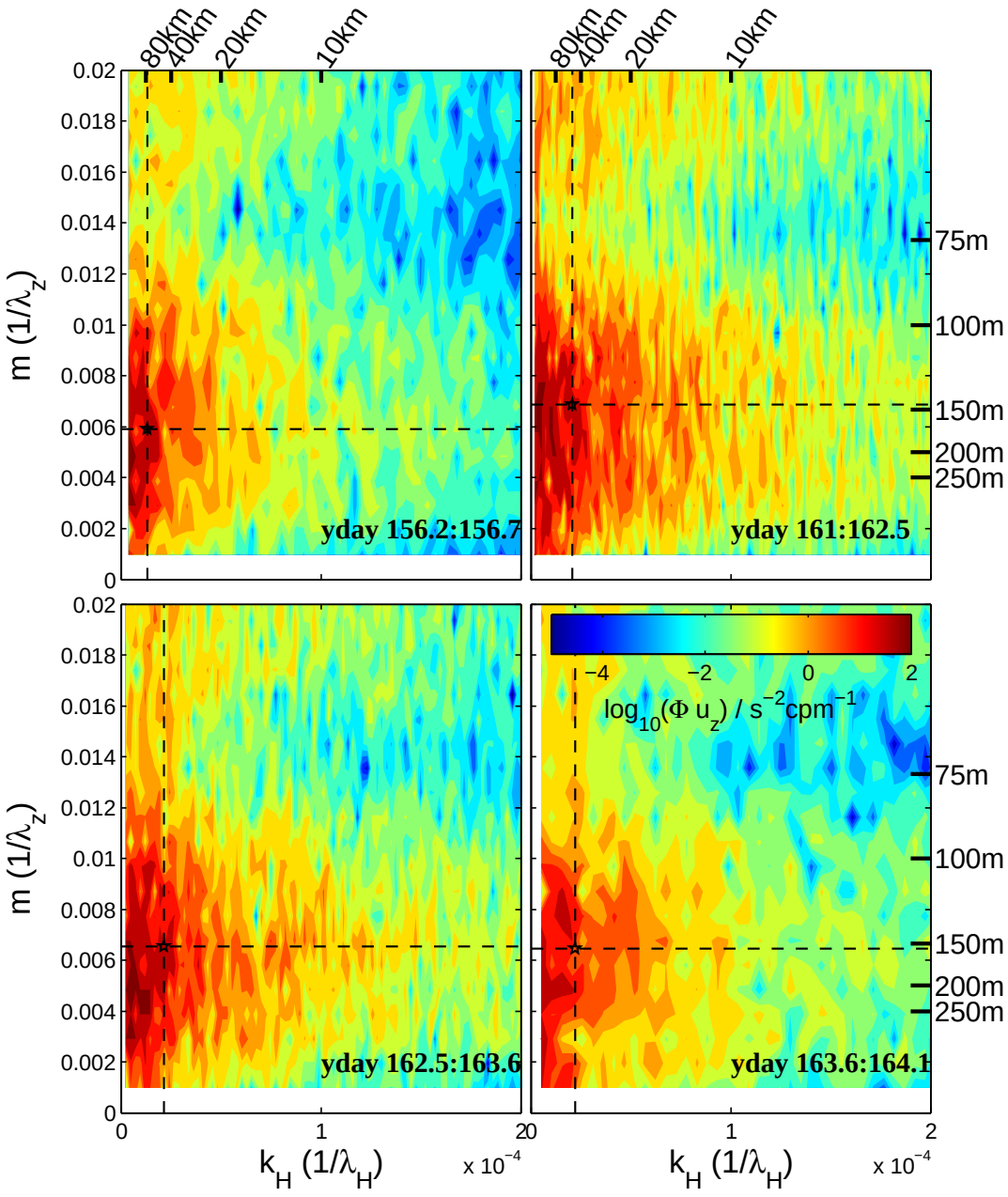

Figure 2.10: 2-D wavenumber spectra (k-m) of shipboard HDSS transects shown in Figure 2.8. Vertical and horizontal dashed lines indicate the centroid (weighted-mean) horizontal and vertical wavelengths.

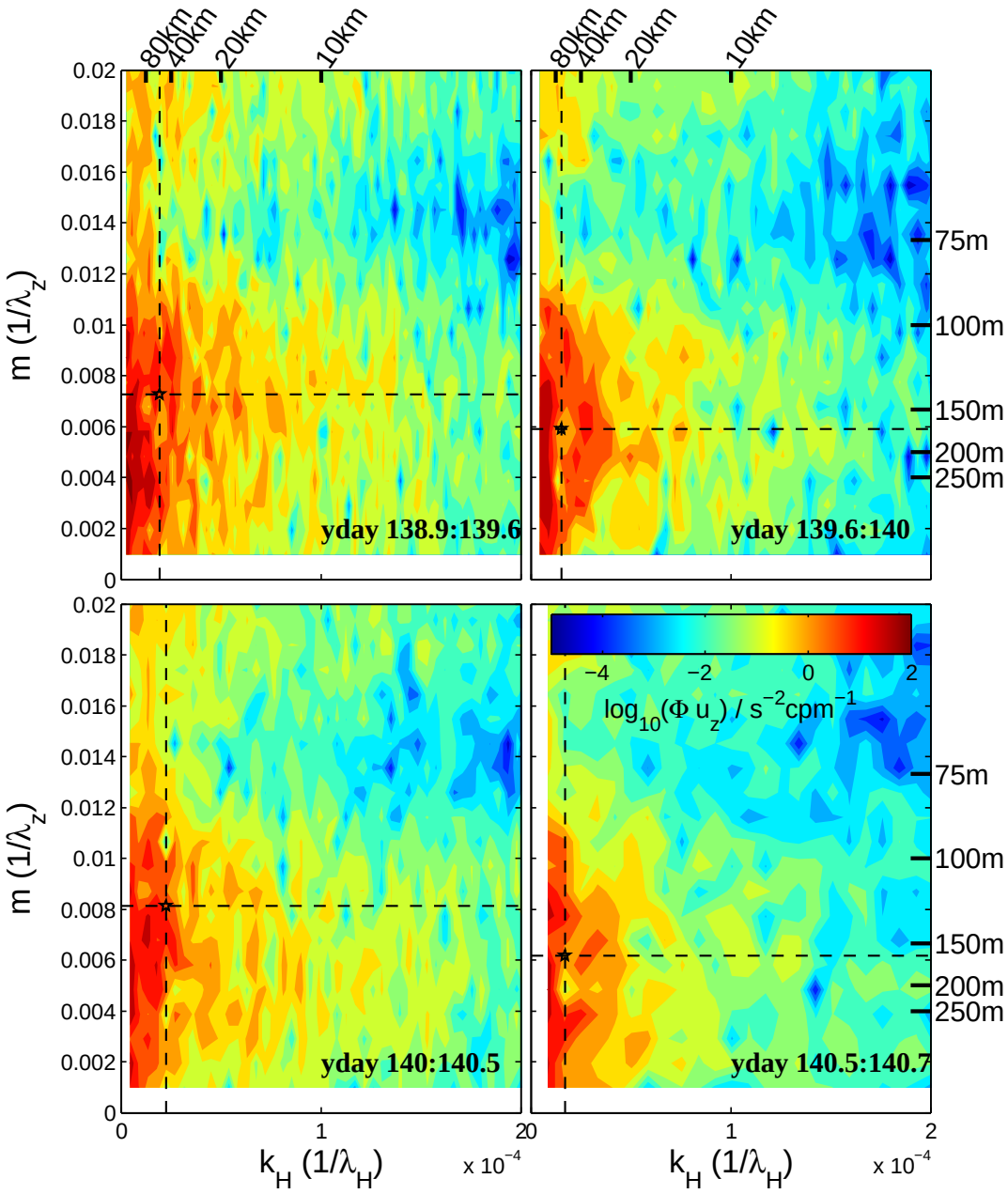

Figure 2.11: 2-D wavenumber spectra (k-m) of shipboard HDSS transects shown in Figure 2.9. Vertical and horizontal dashed lines indicate the centroid (weighted-mean) horizontal and vertical wavelengths.

2.6.4 Summary

Shipboard transects of shear reveal many strong, quasi-linear features that appear to be coherent over large horizontal distances (30-100km). Simultaneous mooring time series confirm that these features are near-inertial. There appears to be a change in character of the features near MP3, which is close to the critical latitude. Features observed north of MP3 slope upwards and are consistent with a downward propagating near-inertial wave. South of MP3, shear layers are more horizontal and appear to extend between MP2 and MP3.

2.7 Properties and Propagation Directions of High-mode Waves

We next employ a plane wave fitting method that allows us to study the characteristics of individual waves seen in depth-time maps on shorter timescales. The simultaneous measurement of shear and strain also allows us to estimate propagation directions for these waves based on their relative phase.

2.7.1 Methods

Planewave fits were performed using the Matlab optimization toolbox, which minimizes the error between data and a plane wave model with variable parameters. The fit model used is a combination of two plane waves, one with propagating upwards and the other propagating downward:

$$X = a + A_u \cos(\omega_u t - m_u z + \phi_u) + A_d \cos(\omega_d t - m_d z + \phi_d) \tag{2.7}$$

where a is a constant, $A_{u,d}$ are wave amplitudes, $\omega_{u,d}$ are the wave frequencies, $m_{u,d}$ are the vertical wave numbers, and $\phi_{u,d}$ are the phases of downward and upward waves, respectively. The fits are applied in overlapping windows with vertical extent of 200m and temporal extent of 3 inertial periods. Fits done over a range of similar vertical and temporal extents indicate that the results are not very sensitive to these exact parameters. The phase difference between the two components of shear, u_z and v_z, is constrained to be $\pi/2$. The fit is applied

to shear and strain together. Frequency and wavenumber are constrained to be the same for shear and strain. An example of the fit results at MP6 is shown in Figure 2.12. Histograms of fit quantities are shown in Figure 2.13.

2.7.2 Results: Wave Propagation Directions

Downward Propagating Waves

The simultaneous measurement of shear and strain allow us to estimate the propagation directions of high-mode near-inertial waves at each mooring (Figure 2.14). There are a variety of directions, but several stronger patterns emerge. At MP6 and MP1, the majority of the downward propagating waves (black) are heading towards the south and southwest. Most of the downward waves at MP4 are also heading towards the south but are more scattered. In contrast, most of the downward waves at MP2 exhibit northward propagation. At MP3, wave directions are more scattered but appear to be dominated by two groups heading towards the northwest and southeast, respectively.

Upward Propagating Waves

Overall, the direction of upward propagating waves appears more scattered than down going waves at most moorings. At MP3, the up going waves show a NW/SE pattern similar to the downward waves there. At MP2 they display a scattered northward preference, and at MP1 most up going waves are going east.

2.8 Discussion

We have presented a variety of observations with the aim of learning more about the near-inertial wave field. These observations shed some light, but also raise more questions, some of which we discuss next.

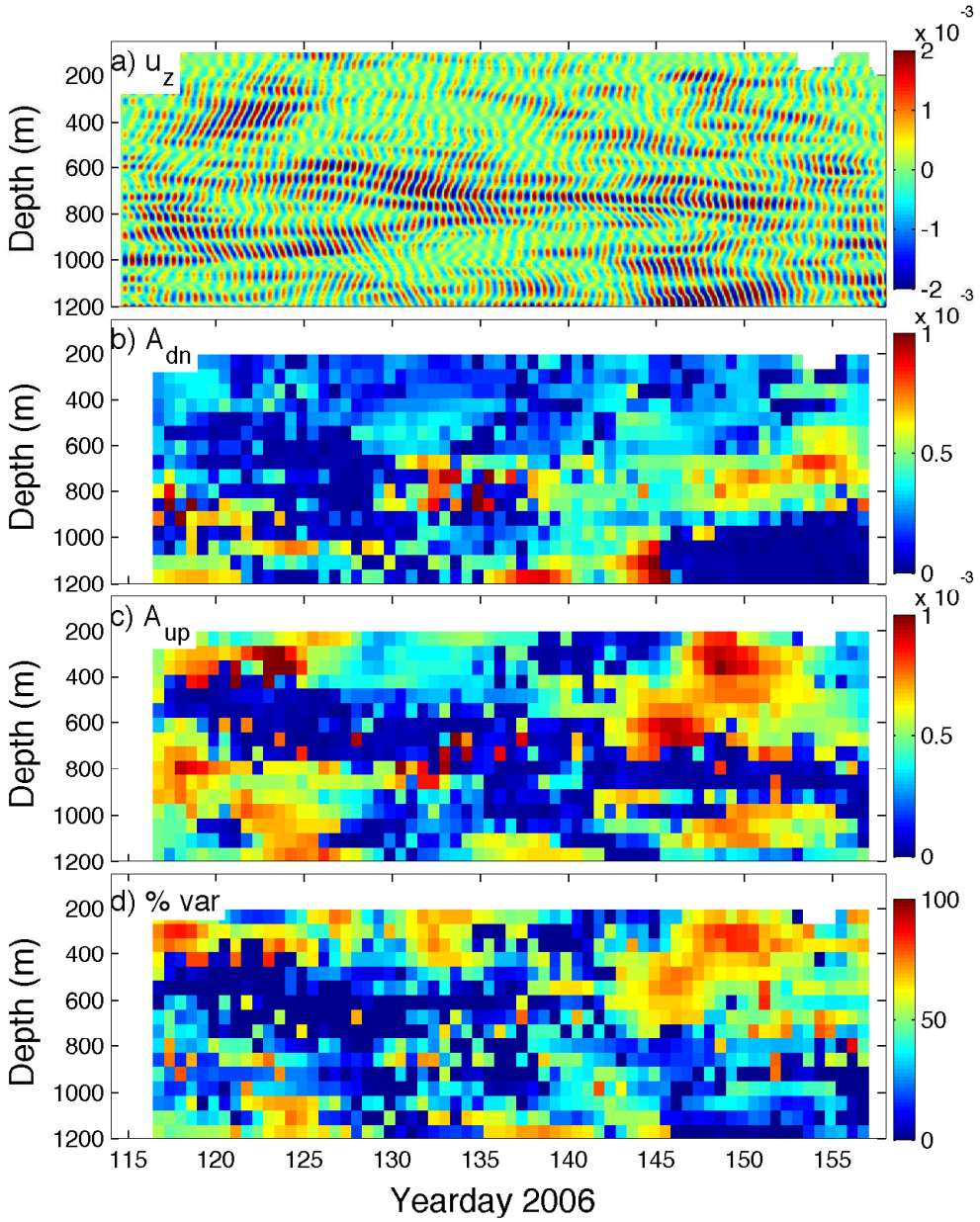

Figure 2.12: Results of sliding plane wave fit to shear at MP6. (a) Near-inertial shear. (b) Amplitude of downward wave fit. (c) Amplitude of upward wave fit. (d) Percent variance explained by fit.

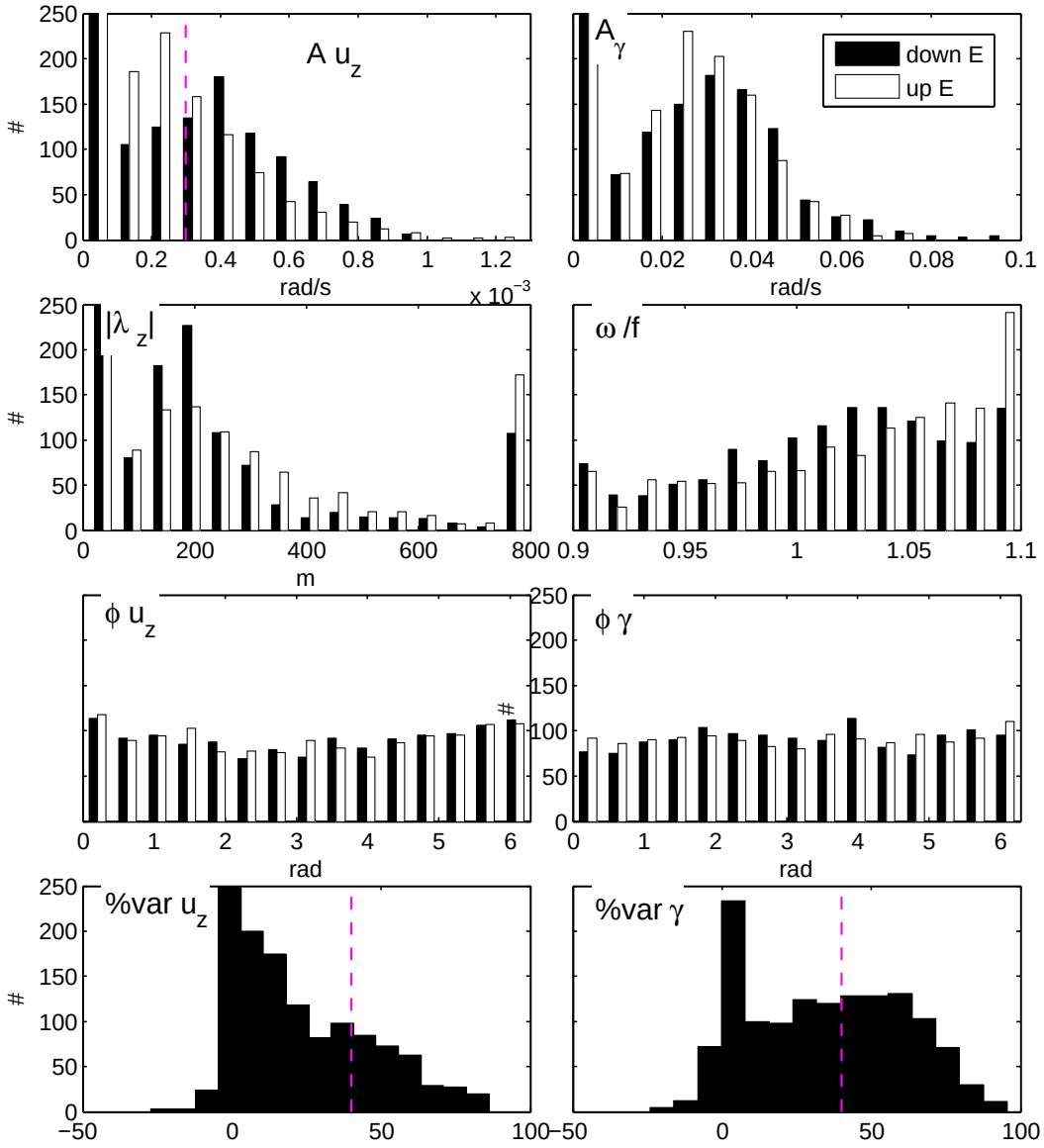

Figure 2.13: Histograms of fit results at MP6. Dashed lines indicate thresholds used to filter data used in Figure 2.14.

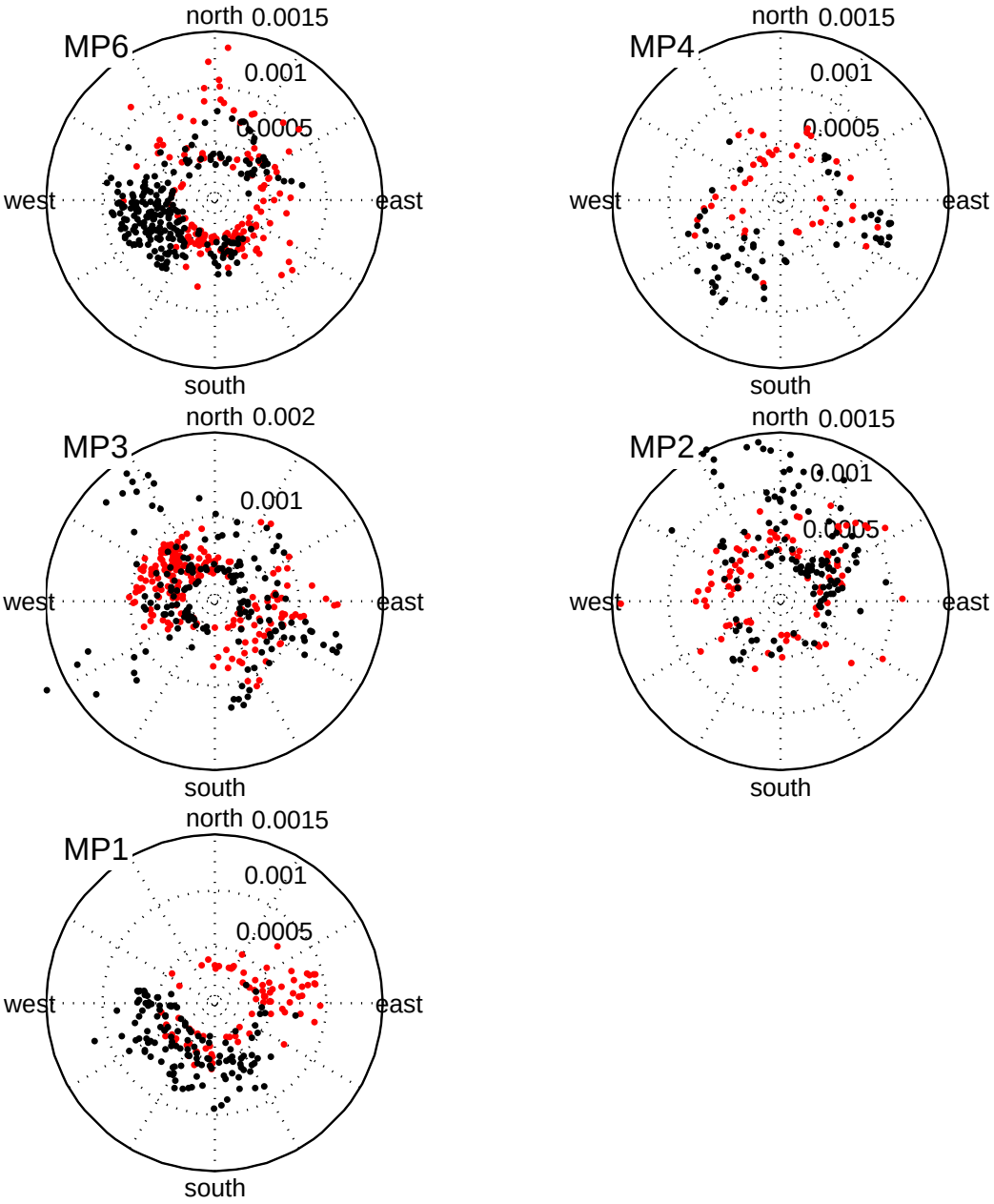

Figure 2.14: Estimated near-inertial wave propagation directions versus shear amplitude at all IWAP moorings, for upward (red) and downward (black) propagating waves that meet threshold for percent variance and amplitude. Note the different (larger) radial limits for MP3.

2.8.1 Low Mode Flux

Near-inertial waves are generally expected to propagate equatorward, since they quickly become sub-inertial if they propagate poleward. Alford (2003a) examined historical mooring records and found a tendency for low-mode near-inertial energy flux to be equatorward at those locations. Here low-mode energy flux was northward at moorings MP1, MP2, and MP3, which we attribute to diurnal internal tides. Energy flux was equatorward at MP4 and MP6, which are north of the diurnal turning latitude and therefore do not include near-inertial motions of tidal origin. Wind forcing during IWAP was relatively weak, but increased to the north. Based on the bandpass filter we used, near-inertial motions observed at MP6 could originate as far north as 43.9^o N (assuming they were generated at f). A rough comparison of the wind work to the observed low mode flux at MP6 can be made with a simple box model. Taking a box from 36-40N and 192-204 E and assuming all this energy goes into equator ward propagating low-mode waves results in an estimated depth-integrated flux of 270 Wm^{-1}. The observed mean equator ward flux at MP6 was 130 Wm^{-1}, 48% of the flux estimated from wind work. A similar calculation for MP4, using a box extending from the mooring north to 35.3 N (the northernmost originating latitude for the near-inertial band at MP4) gives a depth-integrated flux of 313 Wm^{-1}. The mean observed flux at MP4 was 180 Wm^{-1}, 57% of the wind estimate.

2.8.2 Source of Upward Propagating Waves

The source of the observed upward-propagating NIW is somewhat of a mystery. The higher mode waves examined here propagate slowly and should be more susceptible to dissipation due to their higher shear, making it unlikely that the upward propagating waves are wind-generated waves that have survived a bottom reflection. Other possible sources of NIW include generation by flow over rough topography (Nikurashin and Ferrari, 2010), PSI of the internal tide (MacKinnon et al., 2013), and adjustment of fronts (Alford et al., 2013).

We expect PSI to generate both upward and downward propagating near-inertial waves near MP3. MacKinnon et al. (2013) confirmed energy transfer through PSI at some depths and times. At the critical latitude, PSI should produce purely inertial motions, which would have no strain. Qualitatively, shear at MP3 appears more checkerboard, indicative of purely inertial motions, or of equal amplitude up and down going waves. However, the waves identified by the plane wave fitting technique must be slightly sub- or super- inertial, since they have a strain signature. These waves could be from PSI slightly south of the critical latitude, or near-inertial waves from other sources. It is interesting that both up and down wave directions at MP3 appear to be clustered in two groups (NW and SE), which are approximately perpendicular to the direction of the internal tide.

Another source of upward propagating waves could be deep generation by flow over topography. There are plenty of areas of rough topography in the region, including the Musician seamounts. The direction of waves generated via this mechanism would depend on the details of the near-bottom flow and topography. Newer model simulations with realistic deep flows (Arbic et al., 2009) might enable estimates of the importance of this process.

2.9 Conclusions

We have presented simultaneous depth-time observations of shear and strain in the upper ocean from profiling moorings, and shear from shipboard ADCP transects. The data are analyzed with the goal of learning more about near-inertial motions and their sources. Our conclusions based on the three main analyses in this paper are listed below:

1. Low-mode near-inertial energy flux was computed at 5 moorings. The record length is not sufficient to separate the diurnal and near-inertial frequencies at the southernmost three moorings. Low mode energy flux is northward at the three moorings south of the diurnal turning latitude (MP1,MP2, and MP3), suggesting that it is dominated by the diurnal internal tide. Energy flux at the two moorings north of the diur-

nal turning latitude (MP4,MP6) is southward, consistent with expected equatorward propagation of near-inertial energy. The average depth-integrated near-inertial energy flux is 180Wm^{-1} at MP4 and 130Wm^{-1} at MP6.

2. Shipboard transects of velocity and shear show the horizontal spatial structure of near-inertial waves. Simultaneous moored measurements confirm that the spatial features are near-inertial. Much of the near-inertial shear is coherent over large horizontal distances, on the order of 80 km. A change in character is seen near the critical latitude for PSI of the M_2 internal tide, close to MP3. Between MP2 and MP3, features are more horizontal. Features observed North of MP3 show a tendency to slope more and are consistent with a downward, equatorward propagating near-inertial wave.

3. A plane wave fitting method is used to characterize higher-mode NIW over temporal and vertical scales of $\sim$3 days and $\sim$250m, respectively. A large portion of the shear and strain variance is captured by these fits. The phase between shear and strain determined by these fits is used to estimate the propagation directions of waves. Downward propagating NIW show a tendency to propagate southward (equatorward) at MP1,MP4 and MP6. The direction of upward propagating waves is more scattered. MP3 appears different from the other moorings; shear amplitude is larger, and wave directions are clustered into two main groups, towards the northwest and southeast.

2.10 Acknowledgment

We are greatly thankful for the expertise, cheerful attitude and hard work of *R/V Revelle* captain, Tom Des Jardines, and crew, as well as Eric Slater, Mike Goldin, Mai Bui, Jon Pompa, Tyler Hughen, Eric Boget, Andrew Cookson, Dave Winkel, Oliver Sun, Kim Martini, Paola Eccheverri, Tom Peacock and Carl Mattson. This work was supported by NSF grant OCE-0424717.

2.11 *Appendix - Determining the Propagation Direction of Near-inertial Waves from the Phase between shear and strain*

Starting from the standard internal wave polarization relations for velocity and displacement, the polarization relations for shear and strain are

$$u_z = \frac{(N^2 - \sigma^2)}{(\sigma^2 - f^2)}(-ik + \frac{lf}{\sigma})w \tag{2.8}$$

$$v_z = \frac{(N^2 - \sigma^2)}{(\sigma^2 - f^2)}(-\frac{kf}{\sigma} - il)w \tag{2.9}$$

$$\gamma = \frac{\partial \eta}{\partial z} = im\eta = \frac{-m}{\sigma}w \tag{2.10}$$

where the vertical velocity $w = \exp[i(kx + ly + mz - \omega t)]$.

To match the sign convention used in the data, expressions for shear are multiplied by -1. The polarization relations for shear and strain, matching the data conventions, are then:

$$u_z = \frac{N^2 - \sigma^2}{(\sigma^2 - f^2)}(ik - \frac{lf}{\sigma})w \tag{2.11}$$

$$v_z = \frac{N^2 - \sigma^2}{(\sigma^2 - f^2)}(\frac{kf}{\sigma} + il)w \tag{2.12}$$

$$\gamma = \frac{\partial \eta}{\partial z} = im\eta = \frac{-m}{\sigma}w \tag{2.13}$$

$$\tag{2.14}$$

Computing the phase lag for all directions, we find expressions for the propagation direction θ:

$$\theta_{up} = -\delta\phi_{up} \tag{2.15}$$

$$\theta_{down} = 180 - \delta\phi_{down} \tag{2.16}$$

where θ is propagation direction in degrees true (CW from N) and $\delta\phi$ is the phase lag between zonal shear u_z and strain (positive if strain leads shear).

Chapter

VELOCITY STRUCTURE OF INTERNAL TIDE BEAMS EMANATING FROM KAENA RIDGE

3.1 Copyright Notice

3.2 Introduction

Internal tides are the focus of active research because they are believed to supply a significant fraction of the energy required for deep-ocean mixing (Munk and Wunsch, 1998; Wunsch and Ferrari, 2004). In the immediate vicinity of supercritical topographic features, the generated waves take the form of compact beams propagating upward and downward from the ridge flanks. In the farfield, the structure is dominated by the first and second vertical modes,

presumably because the higher modes needed to form the beams dissipate owing to their greater shear and slower propagation speeds. The transition between these two regimes is of interest since it provides information on the vertical and lateral structure of the dissipation in the vicinity of the ridge. The presence of low-frequency mesoscale flows modulates this picture in as-yet poorly understood ways, both by altering the stratification and therefore the location of the beams, and by refraction from the horizontal structure and vertical shear of the currents (Rainville and Pinkel, 2006b).

The structure of M_2 internal tides in the vicinity of Hawaii's Kaena Ridge (Figure 3.1) has been well documented in both models (e.g., Merrifield and Holloway, 2002) and a host of observations made during the Hawaii Ocean Mixing Experiment (Rudnick et al., 2003). The models indicate generation at locations along the ridge flanks where the topographic slope equals the semidiurnal characteristic slope, subsequent upward propagation toward the surface, and downward propagation after that before finally becoming dominated by the lowest modes. As seen in depth-integrated energy flux (Figure 3.1, colors) propagation is away from the ridge toward the north and south. In spite of hypotheses that the surface bounce might be a region of strong dissipation (New and Pingree, 1992), no elevated dissipation was observed there (Lee et al., 2006).

By repeatedly steaming along long sections perpendicular to the ridge while measuring velocity and isopycnal depth in the upper few hundred meters with a shipboard acoustic Doppler current profiler (ADCP) and an undulating CTD, Martin et al. (2006) and Cole et al. (2009) confirmed elevated semidiurnal energy along the upward characteristics and in the vicinity of the surface bounce, and downward radiation past that. Here we build upon their work by presenting results from three recent cruises aboard *R/V Kilo Moana*, whose 38-kHz ADCP often reaches to 1500m depth. The greater depth range of these measurements allow a substantially more detailed view of the beams than before. The observations are then compared with, and found to be in good agreement with, the results of a 3-D numerical

Table 3.1: Dates of three cruises during which ADCP transects were made.

Cruise	Year	Dates	Transects
1	2010	29 June - 4 July	1-4
2	2010	9 Oct. - 14 Oct.	5-7
3	2011	3 April - 5 April	8-11

model simulation. We introduce our measurements, present the results, and conclude with a brief discussion.

3.3 Methods

3.3.1 Velocity

Observations are from three cruises conducted over a period of about ten months (Table 3.1) while servicing a mooring located at Station ALOHA (N, Figure 3.1). Eleven transects (black line) were made, centered on and oriented approximately perpendicular to Kaena ridge. The survey track was located along a region of strong semidiurnal internal tide energy flux, as evident from the numerical simulations (color and arrows).

Horizontal velocity was measured with a hull-mounted RDI Ocean Surveyor 38 kHz ADCP, operating with interlaced narrowband and broadband pings. The broadband pings have greater vertical resolution and somewhat higher precision. However, we use the narrowband pings since their range is substantially greater. Velocity was recorded in 24-m bins, with range during the transects varying from 1000 to 1500 m depending on sea state and ship speed. The ship speed during the transects (10-12 knots) and the 5 minute averaging interval of the ADCP data result in a horizontal resolution of 1.5-1.8 km. Data from all transects were linearly interpolated onto a uniform grid from waypoints S to N with 1.5

km horizontal spacing. Velocity was then rotated into an along-track (towards 25°T) and cross-track (towards 115°T) coordinate system.

3.3.2 Model

We compare our observations to numerical simulations from the Princeton Ocean Model (POM), kindly provided by L. Rainville, S. Johnston and G. Carter. Details of the model setup, which are similar to that of Merrifield and Holloway (2002), are described in Rainville et al. (2010). The model is forced with barotropic tidal currents and elevations of the M_2 tide from the TPXO6.2 global tide model (Egbert and Erofeeva, 2002). The stratification is a 10-year average of data from the Hawaii Ocean time series, and is uniform throughout the domain. Horizontal resolution is $\sim$ 1km, and the model is run for 40 tidal cycles. A harmonic analysis is performed over the last six to extract M_2 components. Energy flux magnitude and vectors from the model are shown in Figure 3.1. Horizontal velocity sections are compared with our observations in section 3.4.1.

3.4 Results

All 11 sections of measured along-track velocity are shown in Figure 3.2. In addition to internal tides, measured velocity includes motion from a variety of processes, occurring at all resolved scales and timescales in the ocean at the time of each transect. However, many features in the raw data are clearly due to internal tides. These are first discussed in the context of the individual sections before isolating the M_2 motions in the next section with harmonic analysis.

Most sections show prominent sloping velocity features, tending to coincide with theoretical M_2 ray paths (dashed lines). These were computed from the equation

$$\frac{dz}{dx} = \sqrt{\frac{\omega^2 - f^2}{N(z)^2 - \omega^2}}, \tag{3.1}$$

where f is the Coriolis frequency, ω is the wave frequency, and N is the buoyancy frequency computed from the Levitus and Boyer (1994) climatology at 21°N, 201°E. Ray paths for semidiurnal (M_2) and diurnal (K_1) frequencies are plotted emanating from the locations of critical slopes on Kaena Ridge's flanks (ray paths are plotted at the same location in all plots). The steeper rays are associated with M_2.

Most sections show strong flow (relative to the background flow) just above the ridge between 600-900 m. Many also show stronger flow in the expected vicinity of the surface reflection of both the northward (e.g. #3,11) and southward beams (e.g. #3,7). To the north, the observed surface bounce appears to occur about 15-20 km northward of the expected locations given by the ray paths.

In addition to the semidiurnal beams, some features (e.g. #2 south of the ridge or #10 north of the ridge) have a shallower slope, roughly consistent with diurnal frequency ray paths (gray dashed). These features may be K_1 internal tides generated at the ridge, or possibly $\frac{1}{2}M_2$ waves resulting from Parametric Subharmonic Instability (PSI, Carter and Gregg, 2006).

3.4.1 Harmonic Fit and Model Comparison

The individual transects are imperfect views of the semidiurnal tide because i) they contain all frequencies, and ii) they are not synoptic snaphots as each took 12-13 hours to complete. Martin et al. (2006) and Cole et al. (2009) intentionally detuned their observations from the M_2 frequency, such that a simple time average at each location was equivalent to a phase average. Since our sampling was opportunistic and our resulting phase coverage (Figure 3.3a) is therefore variable and not as complete, we isolate semidiurnal motions with harmonic analysis at each along-track location.

More transects were completed on the northern side of the ridge than on the south. However, some of the extra transects are at similar M_2 phases, resulting in similar phase coverage

at all locations. At each along-track location and depth with more than 6 occupations, M_2 amplitude u_o, and phase ϕ are determined via least-squares methods by fitting the data, $u(x, z, t)$ to the model,

$$u(x, z, t) = u_0(x, z) \sin(\omega_{M_2} t + \phi_u(x, z)), \tag{3.2}$$

where ω_{M_2} is the semidiurnal tidal frequency. Sensitivity studies were conducted by also fitting mean flow and a diurnal component to the flow. Neither significantly altered the M_2 solutions.

Example fits are shown in Figure 3.3b and c for a region dominated by the semidiurnal internal tide (b) and one less so (c). Observations (x's and o's) and the resulting fit (black line) are plotted versus M_2 phase. Phase is relative to the beginning of the first cruise (June 29, 2010), and does not correspond to high/low tide. Dashed lines in Figure 3.3a and markers in the upper left panel of Figure 3.2 indicate their locations.

Our observations do not span the water column; thus barotropic and baroclinic motions cannot be separated. Since the barotropic motions do not vary in depth and are laterally large-scale, this choice does not affect the structure of the beams. Martin et al. (2006) found that the barotropic tides contributed <25% of the semidiurnal energy immediately above the ridge, and <10% elsewhere.

The spatial structure of the M_2 beams is shown in Figure 3.4 for observations (top) and the POM model (bottom), for both amplitude (u_o, left panels) and a snapshot at time $t = t_o$ ($u_o \sin(\omega t_o + \phi_u)$, right panels). Qualitative agreement is seen between the model and observations. Energy is seen extending downward from the northward surface bounce, as in the model. The observed amplitude is generally stronger than the model output, likely because the observations do not separate M_2 and S_2, while the model is M_2 only. The observations and the model both show elevated signals at i) the intersection of the two beams above the ridge, and ii) near the first surface reflection.

3.5 Conclusion

Repeated opportunistic shipboard ADCP transects were conducted spanning the Kaena Ridge, a major supercritical generator of internal tide beams. Harmonic fits were used to construct spatial maps of the structure of these beams, and were then compared to theoretical characteristics and numerical model simulations. The depth range of the ADCP was 1000-1500m compared to 600 m for previous studies by Martin et al. (2006) and Cole et al. (2009), revealing substantially more structure. The results from our harmonic fits generally agree with the model simulations and previous observations.

The presence and location of the beams is relatively constant over time, as evidenced by the success of the harmonic fit to limited data spanning 10 months. However, individual transects do suggest some spatial variability between individual transects. Examination of spatial and temporal variations in stratification from both climatological data (Levitus and Boyer, 1994) and Hawaii Ocean Time-Series data (*http://hahana.soest.hawaii.edu/hot/hot-dogs/*) indicate that they would shift the surface-reflection location by only 1-4 km. We hypothesize that spatial variations in the beams are due in large part to refraction by mesoscale currents, highlighting the need to better understand these effects on internal tides.

Additional interesting features were observed in the individual sections that were suggestive of near-diurnal internal tides, but our data were not sufficient to comment on them further. The database of *Kilo Moana* ADCP observations continues to grow with monthly trips to station ALOHA. Future visitation of these additional data, when the time series is long enough to separate all the frequencies, may reveal more.

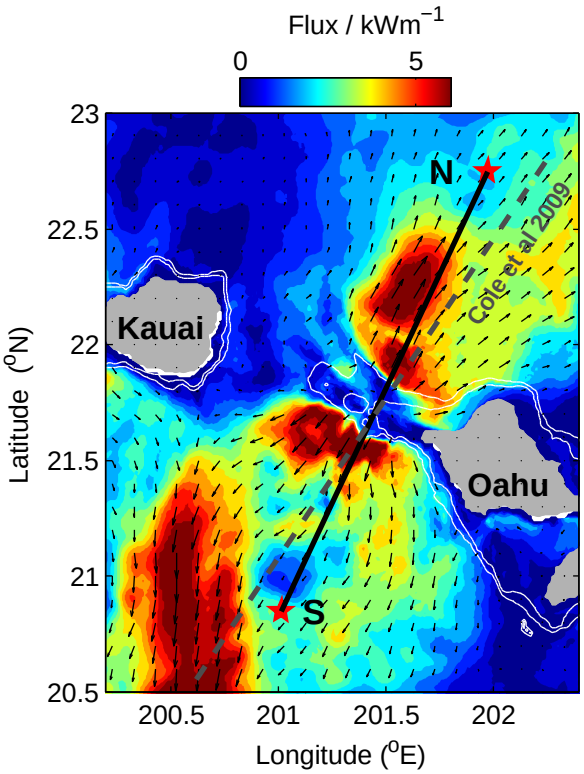

Figure 3.1: Overview map of study area. Eleven shipboard ADCP transects were made along the black line from S to N. Depth-integrated M_2 energy flux magnitude (color) and vectors (black arrows) from numerical model simulations with the Princeton Ocean Model (POM) are plotted. The 1000m and 1500m isobaths are contoured. The gray dashed line shows the approximate location of measurements made by Cole et al. (2009).

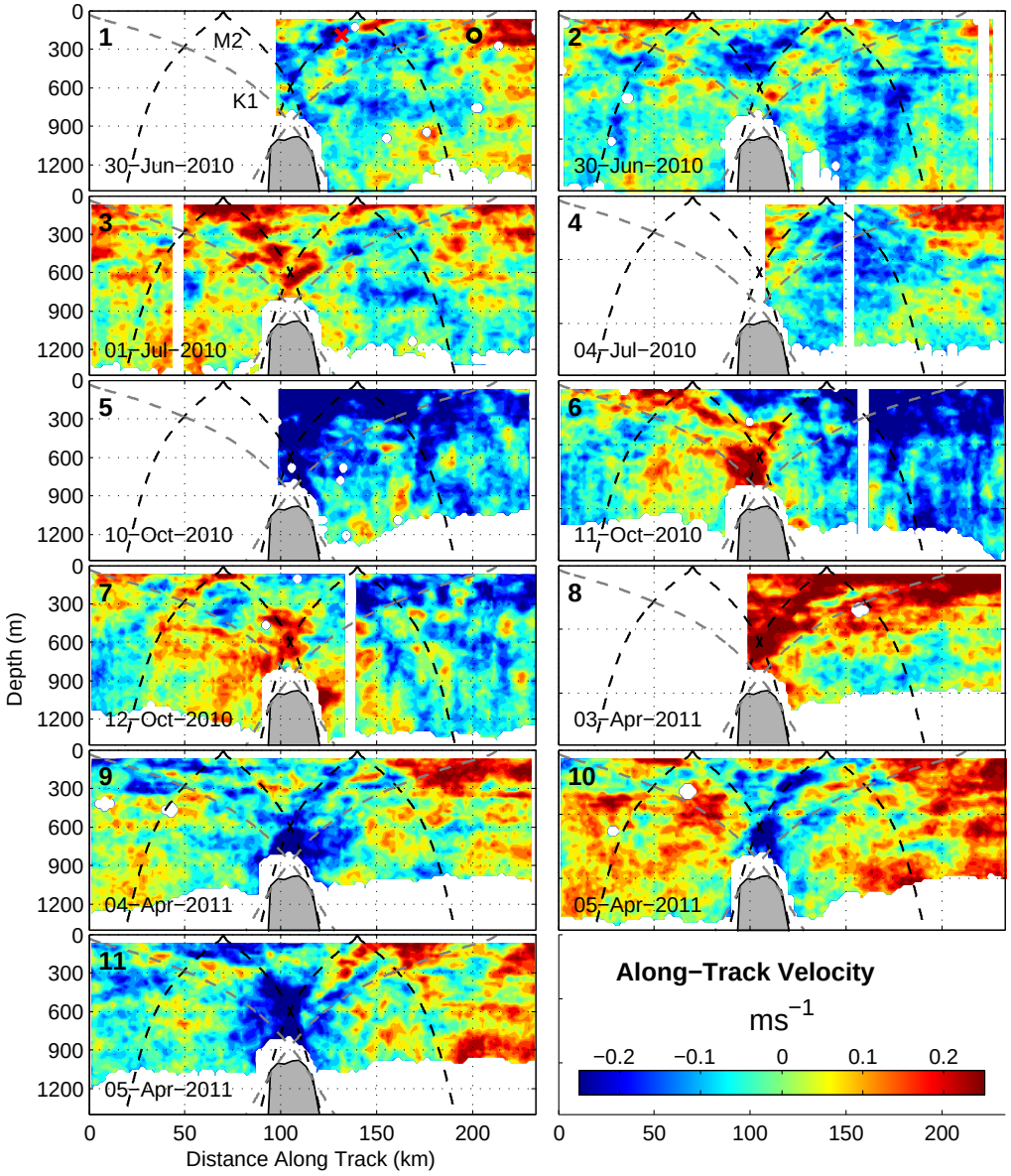

Figure 3.2: Along-track component of raw velocity measured along each transect. Distance is measured from waypoint S to N (Figure 3.1). Kaena Ridge (gray) is visible near the center of each transect. Theoretical M_2 (black dashed) and K_1 (gray dashed) ray paths are plotted emanating from supercritical locations of the ridge flanks. In the upper left panel, the locations of example time-series 1 and 2 (Figure 3.3) are indicated by the red x and black circle, respectively. The date of each transect is indicated in the lower left of each panel.

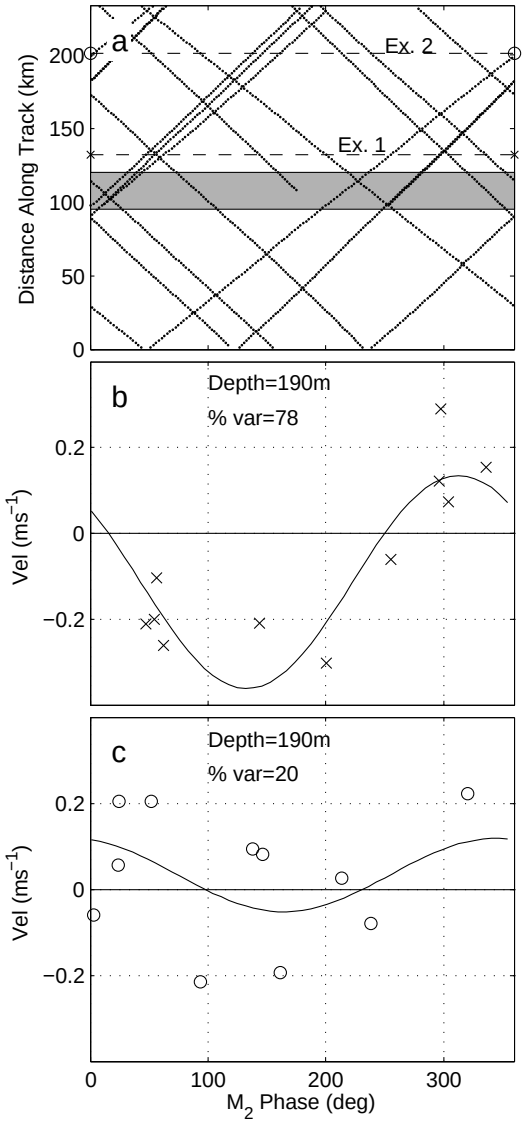

Figure 3.3: M_2 Phase coverage and example time-series. (a) M_2 phase plotted versus distance along the transect. Gray shading indicates the location of Kaena Ridge along the ship-track. Horizontal dashed lines indicate locations of example time series in lower 2 panels. (b) Time-series of measured along-track velocity and harmonic fit (line) for example 1. (c) As in (b), for example 2. The depth and percent of variance explained by the harmonic fit is also indicated.

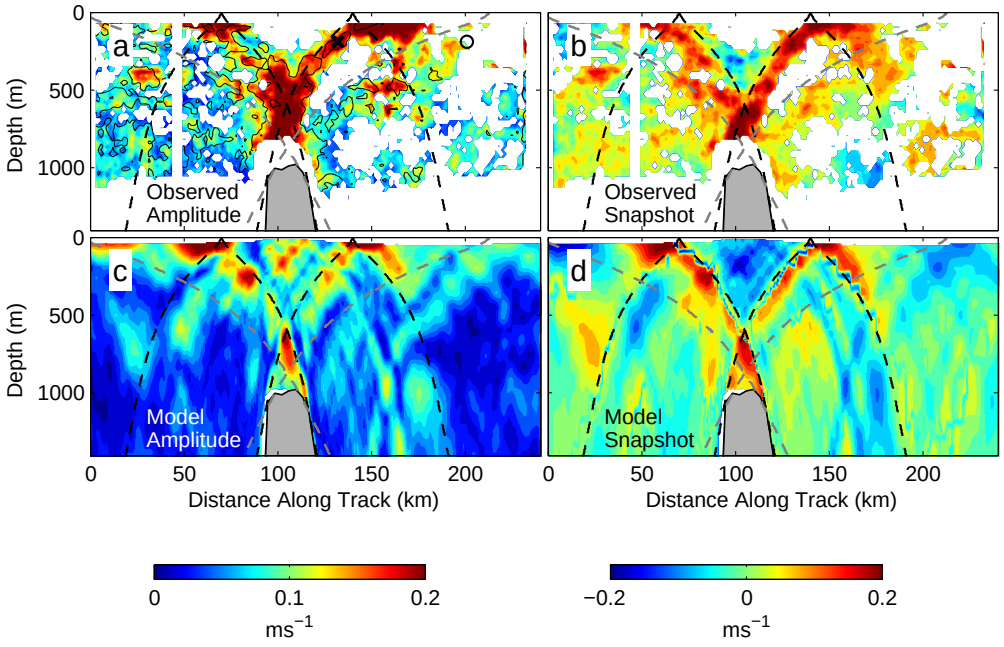

Figure 3.4: Results of harmonic fit to velocity time-series at each grid point: Top row is from observations: (a) M_2 amplitude (m/s) and (b) Snapshot of M_2 velocity on yearday 179.4 , constructed from harmonic fit. Data is contoured only where fit explained more than 20 percent of the variance. Black contours in (a) show regions of 60 percent variance. Bottom row is (c) amplitude and (d) snapshot from POM model along the ship track.

Chapter

STRUCTURE AND VARIABILITY OF INTERNAL TIDES IN LUZON STRAIT

4.1 Note

The contents of this chapter were submitted to the *Journal of Physical Oceanography* for peer review on Dec. 11 2014.

4.2 Introduction

Internal tides, generated where the barotropic tides force stratified water over underwater bathymetry, are thought to provide a significant fraction of the 2 TW of energy required to maintain abyssal stratification and the Meridional Overturning Circulation (Munk and Wunsch, 1998). They contribute to ocean mixing through a cascade of energy to smaller-scale waves or by shoaling on remote continental slopes. A better understanding of the generation, propagation, and dissipation of internal tides near major generation sites is necessary to understand and predict these processes under present and future oceanographic conditions.

One large source of internal tides is Luzon Strait (Simmons, 2004; Jan et al., 2008), where internal tides are generated at two steep submarine ridges separating the South China Sea from the Pacific Ocean (Figure 5.1). In addition to the complex bathymetry, Luzon Strait also features intrusions of the Kuroshio current and high mesoscale variability. The Internal Waves in Straits Experiment (IWISE) was designed to investigate internal wave dynamics in this complex environment. Two major scientific objectives of IWISE are determining how internal tides in Luzon Strait are affected by (1) a double-ridge system with complex topography, and (2) strong, time-variable currents and stratification.

As it propagates west from the ridges, the internal tide often steepens into nonlinear internal waves (NLIWs) (Ramp et al., 2004; Farmer et al., 2009; Li and Farmer, 2011; Lien et al., 2014) that are associated with large vertical displacements, currents, and turbulence that may impact the local ecosystem (Wang et al., 2007; Moore and Lien, 2007). Improving predictive capability for these NLIWs through a better understanding of the variability of internal tide generation at Luzon Strait is another motivation for this work. Park and Farmer (2014) recently showed that accounting for effects of the Kuroshio on wave propagation west of the Strait improves the prediction of NLIW timing, but predicting the amplitude is still a challenge.

The two ridges in Luzon Strait contain multiple internal tide generation sites, and the resultant combination of waves produces interference patterns in depth-integrated energy fluxes (Figure 5.1 b,c). Energy flux vectors form a clockwise gyre in the northern section of the Strait, where both the west and east ridges generate significant internal tides. To the south where the western ridge is deeper and does not generate strong internal tides, energy fluxes emerge primarily from the east ridge, consistent with a single source there. These patterns are predicted in models (Jan et al., 2008; Buijsman et al., 2012) and confirmed in measurements made during the IWISE pilot cruise (Alford et al., 2011).

The main goal of this work is to quantify influences from the mesoscale or Kuroshio using the coherence of internal tides over several spring-neap cycles. The coherent portion of the internal tide maintains a constant phase and amplitude with respect to the barotropic tidal forcing. Quantifying the coherence of the internal tide is important for several reasons. Estimates of internal tide energy flux made from satellite altimetry only capture the coherent portion of the signal (Ray and Zaron, 2011; Zhao, 2014). Knowledge of the coherent-incoherent partitioning is needed to make accurate estimates of internal tide propagation and induced mixing, or to remove the internal tide signal for investigation of other non-tidal processes. Coherence is also closely related to predictability of internal tides and associated

NLIWs. If it were 100% coherent, the internal tide could be predicted given knowledge of the barotropic forcing and the (constant) amplitude and phase of each constituent. Several mechanisms could lead to incoherence of the internal tide in Luzon Strait. Although they are not necessarily independent, we will here divide them into a conceptual framework of "local" and "remote" mechanisms.

"Local" refers to processes occurring in Luzon Strait, encompassing both ridges. First, generation at the ridges may be modified by changes in stratification or shear over those sites. The Kuroshio is the dominant source of variability in stratification and shear in Luzon Strait. Generation at one ridge may also be modified by waves generated at the other ridge. Changes in phase speed between the ridges caused by the Kuroshio could alter the phase of those waves, leading to variability in generation through changes in the bottom perturbation pressure (Kelly and Nash, 2010; Zilberman et al., 2011). Finally, it is possible that the 3D interference pattern in the northern portion of the Strait (Buijsman et al., 2014) could be shifted by the Kuroshio, leading to variability and loss of coherence where large gradients exist.

"Remote" refers to mechanisms involving signals that come from outside of Luzon Strait. A portion of the westward propagating diurnal internal tide from Luzon Strait is expected to reflect back from the continental shelf, while the semidiurnal internal tide is expected to propagate on-shelf (Klymak et al., 2011). Mesoscale variability between the shelf and Luzon Strait could alter the phase of the returning signals, leading to lower coherence. Another remote source is the Mariana Arc, which generates strong semidiurnal internal tides that propagate westward to Luzon Strait. These waves propagate through a region of strong mesoscale variability east of Luzon Strait, so their phase upon arrival could be highly variable (Kerry et al., 2013).

In this paper we characterize the internal tide structure and variability in Luzon Strait over several spring-neap cycles, focusing on two moorings with nearly full-depth coverage

over 50 days. Data, methods, and oceanographic context are presented in section 2. Results are presented in section 3, focusing on detailed measurements from two moorings. In section 4 the coherent and incoherent portions of the internal tide are separated. In section 5 we examine the coherence of the internal tide in the model and estimate the effect of several mechanisms on the internal tide coherence. We end with conclusions.

4.3 Data

Observations were made during the Internal Waves in Straits Experiment (IWISE), a research initiative to study the generation, propagation, and dissipation of internal waves in Luzon Strait. A pilot experiment was conducted during summer 2010, consisting of two short-term moorings and 19 shipboard LADCP/CTD stations (Alford et al., 2011) along a northern and southern line. During the summer of 2011, an 8-element moored array (Figure 5.1) was deployed along the same northern and southern lines. The goal of the array was to occupy the same locations studied during the pilot for a longer period, in order to measure the time-variability of those signals over several spring-neap cycles. As a result of the challenging environment, not all moorings returned full-depth data. In this paper, we focus on two moorings (A1 and S9) where nearly full-depth measurements were obtained, allowing reliable separation of barotropic and baroclinic signals and calculation of internal tide energy and flux.

4.3.1 A1

Mooring A1 was located on the eastern ridge in central Luzon Strait (121^{o}40.5$'$ E, 20^{o}31.4$'$ N) at a water depth of 1446 m. A 'Stablemoor' platform at a depth of 705 m housed upward and downward looking 75kHz RDI Longranger Accoustic Doppler Current Profilers (ADCPs), which measured velocity over depths of ∼120-650 m and ∼725-1200 m with 5 minute time resolution. An upward-looking 300kHz ADCP at 80 m measured near-surface

velocity. Seabird (SBE)-37 Microcats (temperature, salinity, and pressure) and SBE-56's (temperature) were deployed along the mooring with 2 minute sampling rate. Pressure records from the SBE-37 Microcats were used to correct for mooring knockdown.

4.3.2 S9

Mooring S9 was located on the southern portion of the eastern ridge ($121^o1.8'$ E, $19^o18'$ N), at a water depth of 2286 m. Two stacked McLane Moored Profilers (MPs) profiled depth ranges of 330-1260 m and 1300-2220 m, measuring horizontal velocity, temperature, and salinity. The MP profiles at a nominal speed of 0.25 ms^{-1}, resulting in a complete profile approximately every hour. The MP has a vertical resolution of $\sim$10 m for velocity and 2 m for density. A subsurface float at 300 m contained an upward looking 75kHz ADCP that measured velocity from $\sim$30-300 m. Between this float and a smaller float at 70 m, a T-chain consisting of SBE-56 temperature loggers spaced 15 m apart measured temperature. Pressure records from the bottom and top of the T-chain were used to correct the SBE-56 temperature records for mooring knockdown (see Appendix for details). Salinity was estimated for the T-chain using the observed T-S relation from the SBE-37. For the following analysis, all data from both moorings were interpolated onto a uniform grid with 10 m vertical and 1.5 hr temporal spacing.

4.3.3 Models

We also make use of two numerical models in this analysis. The first is the MITgcm model, which uses more detailed bathymetry and provides higher spatial resolution, but does not contain any mesoscale variability. The second is the LZS model, which has coarser resolution, but is run over a longer time period and contains a realistic Kuroshio and mesoscale variability in addition to tidal forcing.

MITgcm Model

The Massachusetts Institute of Technology General Circulation Model (MITgcm) (Marshall et al. 1997) was used in 3D configuration, as described in Buijsman et al. (2014). The model uses realistic topography merged from high resolution gridded multibeam data with a resolution of ∼300m and 30-arc second resolution global topography/bathymetry grid (`SRTM30_PLUS`) data from the Smith and Sandwell database with a resolution of ∼1 km (Smith and Sandwell 1997). The density stratification is derived from temperature and salinity data collected in between the ridges (Alford et al., 2011). The tidal forcing at the east, west, north, and south model boundaries is composed of barotropic velocities extracted from TPXO7.2 (Egbert and Erofeeva, 2002).

LZSNFS Model

The Luzon Strait Ocean Nowcast / Forecast System (LZSNFS, hereafter LZS) is an application of the NRL Ocean Nowcast /Forecast System (Ko et al., 2008), which contains the Kuroshio and mesoscale eddies. The system is an integration of a dynamical ocean model and a statistical data-analysis model. The model derives its ocean bottom topography from the Digital Bathymetry Data Base in 2-minute resolution. Open boundary conditions are derived from a larger scale model for the entire East Asian seas (Ko et al., 2009). The barotropic tidal currents of 8 tidal constituents (K_1, O_1, P_1, Q_1, K_2, M_2, N_2 and S_2) are obtained from TPXO7.2 (Egbert and Erofeeva, 2002). This model includes reflection of the internal tide from the continental shelf to the west, but does not contain remote internal tides from outside the domain, including the Mariana Arc. The LZS model has now been used in several studies of internal waves in Luzon Strait and the South China Sea (Chen et al., 2013; Ma et al., 2013).

4.4 Results

Our primary focus is the internal tide energy and energy flux. However, we first take a moment to present the basic data (Figure 4.2) and velocity spectra (Figure 4.3).

4.4.1 Basic Signals

The nearly full-depth coverage allows us to unambiguously separate the barotropic and baroclinic signals. Barotropic tidal velocity is defined as

$$\mathbf{u}_{BT} = \frac{1}{H}\int_{-H}^{0}[\mathbf{u}(z,t)dz - \bar{\mathbf{u}}(z)]dz \tag{4.1}$$

where $\mathbf{u}(z,t)$ is the instantaneous velocity and $\bar{\mathbf{u}}(z)$ is a slowly-varying sub-tidal component. Baroclinic velocity is defined as

$$\mathbf{u}' = \mathbf{u}(z,t) - \mathbf{u}_{BT} \tag{4.2}$$

The spring-neap cycle of tidal forcing is evident in the barotropic velocity (Figure 4.2, top). The barotropic velocities are very strong, up to 0.48 ms^{-1} at A1, and 0.31 ms^{-1} at S9. Velocities at all depths are also dominated by tidal-frequency motions and a strong spring-neap cycle, but exhibit more complexity than the barotropic signals. Vertical displacements are tidally dominated and increase with depth, as indicated by the variability of density contours.

4.4.2 Spectra

Rotary spectra of baroclinic horizontal velocity at a depth of 250 m from S9 are presented in Figure 4.3 (spectra from A1 are similar in character and are not shown). The spectra are dominated by peaks at tidal frequencies as well as sum and difference frequencies (for example $M_2 + K_1$) and higher harmonics. The spectra are elevated about 10-15 times above the theoretical GM76 internal wave spectrum (Garrett and Munk, 1972; Cairns and Williams,

1976), but follow a similar slope and fall-off with increasing frequency. The extreme elevation above GM levels nearly completely masks the usually-prominent inertial peak, which here is only barely detectable.

4.4.3 Mesoscale Velocity and Kuroshio

We use the large spatial extent of the mooring array and the LZS model to characterize the spatial and temporal structure of the Kuroshio and mesoscale velocity field during the experiment. Figure 4.4 shows low-passed velocity vectors from moored ADCPs (color) at 150 m, with the color indicating the time of each measurement (only every 3 days are shown for clarity). Gray vectors are the time-mean low-passed velocity at 150 m from the LZS model during the experiment, which are generally consistent with observations. A persistent Kuroshio intrusion was present during the experiment, entering Luzon Strait from the southeast and passing over the western half of the Strait near the northern line before exiting to the east of Taiwan. It can be seen in observations at moorings N2 and MPN, where low-frequency velocity was strong and to the North during the experiment. Note that A1 was not in the path of the Kuroshio intrusion, which appears to be deflected around the island and shallow topography to the southeast of the mooring. Velocity measured at moorings along the southern line was also outside of the main Kuroshio intrusion, but exhibited strong, variable low-frequency flows, likely eddies spun off of the Kuroshio intrusion.

Low-frequency velocity and stratification at S9 and A1 are computed by low-pass filtering with a cutoff of 0.25 cpd (Figure 4.5). Both moorings have a stratification maximum near 150m. In general N^2, defined as $\frac{-g}{\rho_o}\frac{\partial \rho}{\partial z}$, is higher at S9 than at A1. Variable N^2 is seen in the upper 200-300 m at both moorings. The low-frequency velocities are surface-intensified at both moorings. The velocity at A1 appears to have a weak spring-neap cycle, likely due to tidal rectification. The low-frequency velocity at S9 is dominated by strong ($0.5 \mathrm{ms}^{-1}$) near-surface (0-300 m) pulses with timescales of a few days.

4.4.4 Internal Tides

Internal tide energy and energy flux are computed using standard methods (Kunze et al., 2002; Nash et al., 2005). The diurnal and semidiurnal frequency bands are separated by applying a bandpass filter (gray in Figure 4.3) to the velocity and displacement data. The shallowest and deepest velocities are extended by linear extrapolation to the surface and bottom, respectively. Gaps in velocity were limited to the upper 20m and lower 100m at A1, and the upper 40m and lower 50m at S9. Stratification N^2 and vertical displacement η are linearly interpolated from the shallowest (deepest) measured value to zero at the surface (bottom). Gaps in displacement were limited to the upper 70m and lower 45m at A1, and the upper 90m and lower 60m at S9. Smaller gaps in velocity and displacement in the middle of the water column are filled by linear interpolation.

Horizontal kinetic energy (HKE) and available potential energy (APE) are computed as

$$HKE = \frac{1}{2}\rho < u'^2 + v'^2 > \tag{4.3}$$

$$APE = \frac{1}{2}\rho N^2 < \eta^2 > \tag{4.4}$$

where η is vertical displacement computed over 3 day windows and brackets indicate averaging over a wave period.

The perturbation pressure p' is computed as

$$p' = p_{surf} + \int_z^0 \rho' g dz \tag{4.5}$$

where the density perturbation is given as

$$\rho' = \frac{\bar{\rho}}{g}\bar{N}^2\eta \tag{4.6}$$

The surface pressure p_{surf} is not measured but can be inferred from the baroclinicity condition that the depth-averaged pressure perturbation must vanish (Althaus et al., 2003):

$$\frac{1}{H}\int_{-H}^0 p'(z,t)dz = 0 \tag{4.7}$$

Determining p_{surf} and p' requires integrating over the full water depth. Thus, vertical gaps in measurements can introduce errors in this quantity (Nash et al., 2005; Rainville and Pinkel, 2006a). Sensitivity studies showed that errors in p_{surf} and p' due to interpolating surface gaps were small (<10%), allowing us to compute accurate profiles of p' over the depth ranges we sampled.

Energy flux is defined as the covariance of velocity and pressure perturbations:

$$\mathbf{F} =< \mathbf{u}'p' > \tag{4.8}$$

Although profiles of p' over the measured depth range are accurate, the depth-integrated energy and flux magnitude may differ from the true value due to the vertical gaps. This difference depends on the depth-profile of energy flux, which is normally surface-intensified. To estimate this error, we resampled MITgcm model data from the mooring locations and computed energy flux in the same manner as the observations. Errors from the true value were 1% and 17% for diurnal and semidiurnal at A1, and 5% and 9% for diurnal and semidiurnal fluxes at S9. Importantly, these errors give rise to largely time-independent biases that do not affect our present focus on the time-variable signals and their coherence.

We also compute barotropic to baroclinic conversion, defined as (Kelly and Nash, 2010)

$$C =< \nabla H \cdot (\mathbf{U_{BT}} p_b') > \tag{4.9}$$

Where ∇H is the bottom slope, p_b' is the perturbation pressure at the bottom, and brackets indicate averaging over a wave period.

4.4.5 Depth-time Structure of Internal Tides

We first examine and contrast the depth-time structure of the diurnal internal tide at S9 and A1. Semidiurnal quantities are omitted for brevity; see supporting online material for figures. The diurnal signals are noticeably more coherent at S9, which we will further quantify in a future section. The diurnal internal tide at S9 (Figure 4.6) exhibits a relatively clean

spring-neap cycle due to the beating of the K_1 and O_1 components. The vertical structure of pressure, energy and flux appears to be low-mode and is similar during each spring tide. Energy and flux are largest in the upper 500 m, with a smaller peak in the lower water column.

At A1, the diurnal velocity at A1 (Figure 4.7b) also shows a strong spring-neap cycle. Energy (dominated here by HKE) has a similar vertical structure during all 4 spring tides. However, pressure (c) is more variable in both time and depth, and does not have such an obvious spring-neap cycle. As a result, the depth and time structure of flux is more variable, notably during the last spring tide (yearday>205). It will be shown in a later section that this lowers the coherence of the diurnal internal tide at A1.

4.4.6 Modal Decomposition

The modal structure of the internal tide was also examined by fitting velocity and displacement profiles to mode shapes determined numerically from the IW vertical structure equation:

$$\frac{d^2}{dz^2}\phi(z) + \frac{N^2(z)}{c_n^2}\phi(z) = 0 \tag{4.10}$$

where ϕ is the vertical mode shape and c_n is the eigen-speed. The modal distributions of time-averaged, depth-integrated APE, HKE, and energy flux at S9 and A1 are shown in Figure 4.8. The modal distributions are red, with most of the variance contained in the first 3 modes. Energy flux is dominated by mode 1 with the exception of the diurnal internal tide at A1, where most of the flux is contained in the first 3 modes. The dominance of low mode flux is typical of internal tides, since the pressure tends to act as a lowpass filter (Nash et al., 2005). HKE at both moorings has more variance at higher modes than energy flux, but still tends to be have a red spectrum, with about 75% most of the total HKE contained in the first 2 modes. At S9 the mode-1 APE contains about 75% of the total in the diurnal band, and less than 50% in the semidiurnal band. At A1, semidiurnal APE is dominated by

mode-1 but diurnal APE is distributed more evenly among modes (note though that diurnal energy at A1 is dominated by HKE).

4.4.7 Depth-Integrated Internal Tide Energy and Flux

Next we examine timeseries of depth-integrated internal tide energy, energy flux, and conversion (Figure 4.9). Time-mean quantities are summarized in Table 4.1. At S9, the diurnal barotropic forcing exceeds the semidiurnal forcing by about a factor of 2. This is reflected in the greater diurnal magnitude of energy (b), flux (c), and conversion (d) at S9.

At A1 (red), diurnal and semidiurnal barotropic forcing have comparable magnitudes. Depth-integrated energy is large in both bands, with semidiurnal exceeding diurnal most of the time. Note that the diurnal energy at A1 is dominated by HKE. While the diurnal and semidiurnal barotropic forcing and energy magnitudes are comparable, the energy flux (c) and conversion (d) are dominated by the semidiurnal band. The diurnal energy flux is small compared to the semidiurnal flux, but still very large compared to typical open-ocean values. Semidiurnal flux appears to be well correlated with the barotropic forcing. Diurnal flux appears less correlated with barotropic forcing, even though the diurnal energy is large and well-correlated.

A map view of the depth-integrated diurnal (left) and semidiurnal (right) energy fluxes at A1 (top) and S9 (bottom) is shown in Figure 4.10. As also seen in Figure 5.1, the observed and modeled fluxes generally show the same patterns, with an interference pattern to the north (a,b) and a single source to the south (c,d). The observed diurnal fluxes at A1 (a) show the greatest directional variability, with some of the fluxes towards the SW in agreement with the model, but also directed west and east at times. The semidiurnal band at S9 also shows more directional variability, but less than the diurnal band at A1.

4.5 Coherent/Incoherent Separation

We next decompose the internal tide signals into coherent and incoherent components using a method similar to Nash et al. (2012). A harmonic fit to the major diurnal (K_1,O_1,Q_1) or semidiurnal (M_2,S_2,N_2) tidal constituents is performed on the bandpass-filtered timeseries of diurnal or semidiurnal velocity and pressure at each depth. Note that the bandwidth of the filter will affect the partitioning of coherent and incoherent signals (since an infinitely thin passband contains just 1 frequency and is 100% coherent by definition). The passbands we used (shown in gray in Figure 4.3) are 0.85-1.15 cpd for the diurnal band and 1.7-2.3 cpd for the semidiurnal band, which include the 3 diurnal or semidiurnal constituents used for the harmonic fits. We do not include P_1 or K_2 in the fits because the record length is not long enough to resolve them from K_1 or S_2, respectively. The coherent part $(u,p)_c$ is defined as the reconstructed fit, and the remainder is defined as the incoherent part:

$$u_i = u - u_c \tag{4.11}$$

$$v_i = v - v_c \tag{4.12}$$

$$p_i = p - p_c \tag{4.13}$$

Velocities are separated into barotropic and baroclinic components

$$u_c' = u_c - u_c^{BT} \tag{4.14}$$

$$u_i' = u_i - u_i^{BT} \tag{4.15}$$

$$\tag{4.16}$$

where $u_{c,i}^{BT}$ is the depth-mean of $u_{c,i}$. Then baroclinic energy, energy flux, and conversion are computed separately for each component. In addition to the coherent and incoherent terms, there is a third component resulting from the cross-terms. APE is given by:

$$APE = APE_c + APE_i + APE_{cr} \tag{4.17}$$

$$APE_c = \frac{1}{2}\frac{g^2}{\rho N^2}\rho_c'^2 \tag{4.18}$$

$$APE_i = \frac{1}{2}\frac{g^2}{\rho N^2}\rho_i'^2 \tag{4.19}$$

$$APE_{cr} = \frac{g^2}{\rho N^2}\rho_c'\rho_i' \tag{4.20}$$

$$\tag{4.21}$$

HKE is given by:

$$HKE = HKE_c + HKE_i + HKE_{cr} \tag{4.22}$$

$$HKE_c = \frac{1}{2}\rho < u_c'^2 + v_c'^2 > \tag{4.23}$$

$$HKE_i = \frac{1}{2}\rho < u_i'^2 + v_i'^2 > \tag{4.24}$$

$$HKE_{cr} = \rho < u_c'u_i' + v_c'v_i' > \tag{4.25}$$

Energy flux is given by

$$F_u = F_c + F_i + F_{cr} \tag{4.26}$$

$$F_c =< u_c'p_c' > \tag{4.27}$$

$$F_i =< u_i'p_i' > \tag{4.28}$$

$$F_{cr} =< u_i'p_c' + u_c'p_i' > \tag{4.29}$$

with similar expressions for the meridional component F_v. Baroclinic to barotropic conversion is given by:

$$C = C_c + C_i + C_{cr} \tag{4.30}$$

$$C_c = U_c^{BT} \cdot \nabla H p_c' \tag{4.31}$$

$$C_i = U_i^{BT} \cdot \nabla H p_i' \tag{4.32}$$

$$C_{cr} = U_c^{BT} \cdot \nabla H p_i' + U_i^{BT} \cdot \nabla H p_c' \tag{4.33}$$

Results

As expected due to their proximity to strong internal tide generation sites, the coherent term (Figures 4.11-4.14, orange) is generally the largest of the 3 components. Although not strictly tied to the barotropic forcing, we loosely interpret the coherent component as the locally-generated internal tide, in the absence of changes in mesoscale stratification or velocity. The magnitude and direction of the coherent flux vary according to the spring-neap cycle, and spring tides are not identical because of the Q_1 and N_2 components.

The remaining incoherent and cross-terms are deviations from this regular cycle. They tend to also be largest during spring tides, but their phase and/or amplitude vary on timescales shorter than the ∼50 day record, and as a result they are not captured in the harmonic fits. Fits over individual spring tides (not shown) are more coherent, suggesting that changes in the internal tide's amplitude or phase occur on timescales between 14 and 50 days.

To compare the coherence at different locations, we compute the percent variance of each quantity that is explained by the coherent portion of the signal:

$$\%var_X = [1 - \frac{var(X - X_c)}{var(X)}] \times 100 \tag{4.34}$$

which is indicated in the upper left of each panel in Figures 4.11- 4.14 and Table 4.2.

The coherence of the diurnal energy flux at A1 is less than 30%, significantly less than the diurnal internal tide at S9 and the semidiurnal internal tide at both locations. The diurnal A1 energy flux (Figure 4.13 d,e) is dominated by the cross-term fluxes, which are of comparable magnitude as the coherent fluxes and change the sign of both components of energy flux, resulting in highly variable energy flux vectors (as seen in Figure 4.10). Further decomposing the cross-term fluxes into their two components (Eq. 4.29) reveals that they are dominated by the term involving incoherent pressure $< u'_c p'_i >$. This is consistent with the qualitative incoherent nature of perturbation pressure and energy flux seen in Figure

4.7c. Conversion (f), which depends on the magnitude and phase of bottom perturbation pressure, is also less coherent at A1 (63%).

Cross-term fluxes in the semidiurnal band at A1 and both bands at S9 are of similar magnitude, but smaller relative to coherent fluxes. At S9, the diurnal zonal F_{cr} (Figure 4.11d) is negative during the first two springs, and positive during the last two springs. Meridional F_{cr} is mostly positive during the first two springs, and negative during the last two springs. The zonal F_{cr} appears to be somewhat correlated with the mean low-frequency velocity over the upper 1000 m (Figure 4.5e), suggesting that the internal tide energy flux may be modified by the low-frequency eddy/mesocale velocities.

The levels of coherence are summarized in Figure 4.15, in which it can be seen that the diurnal band at S9 and the semidiurnal band at A1 are largely coherent ($> 70\%$ for all quantities). Semidiurnal motions at S9 are slightly less coherent ($> 60\%$). Diurnal motions at A1 stand out as significantly less coherent ($< 30\%$ except for HKE) than the other three, consistent with the visual appearance of pressure (Figure 4.7c), and the obvious veering of the flux direction (Figure 4.10a). We discuss reasons for this next.

4.6 Discussion

Which of the several possible physical mechanisms are responsible for the observed levels of internal tide incoherence in Luzon Strait? We first use a simple 2D toy model to estimate the effect variable stratification and velocity due to the Kuroshio have on internal tides propagating between the ridges at 20.5^{o}N. The model consists of a coherent mode-1 internal tide generated at both ridges, with the total observed internal tide at A1 then consisting of the superposition of the locally generated wave (the observed coherent internal tide) and the wave arriving from the western ridge after traveling through variable phase speed between the ridges. The phase speed is calculated from the Taylor-Goldstein equation using low-passed velocity and stratification from the LZS model. The resulting coherence of flux and

conversion in both bands (Eq. 4.34) is 99%, showing that this mechanism has a negligible effect.

Next we use a similar model to consider the impact of the diurnal internal tide reflected from the continental shelf to the west. In this scenario, a local (coherent) internal tide is generated at A1 and propagates west to the slope at 117.5^oE, where 1/3 of the energy reflects back, consistent with Klymak et al. (2011). The resulting diurnal coherence in this 2-D model is 86% for flux and 99% for conversion. This mechanism could explain some of the lower diurnal coherence in flux at A1, but the observed coherence is significantly lower. However, it is enough to explain the 88% coherence of the diurnal flux at S9. Klymak et al. (2011) note that the amount of diurnal energy reflected is sensitive to the phase between mode 1 and 2 waves. Using the LZS model data, we calculated the mode-1 and 2 phase speeds, and the phase difference between them after propagating to the shelf (assuming they start in phase). The phase difference has a range of about 80^o, suggesting that the fraction of energy reflected from the shelf could be quite variable in time, helping to explain the modest incoherence observed in the S9 diurnal internal tide.

Finally we consider the effect of remote (semidiurnal) waves from the Mariana Arc. In recent modeling studies, Kerry et al. (2014) found that including remote waves from the Mariana Arc increased the variability of M_2 conversion at Luzon Strait. We estimate the westward energy flux from Mariana as 1.3kWm^{-1} from Kerry et al. (2013), assuming a line source and no dissipation or spreading. This is $\sim 4\%$ of the mean semidiurnal coherent flux at A1, and is likely an upper bound. In the absence of detailed stratification or velocity information along the entire transect, we assume that the phase speed and travel time vary similarly to a LZS model point east of the ridges. The phase of the arriving wave has a range of more than 360^o, and the coherence of the semidiurnal flux in this 2-D model is 69%. This is lower than the observed semidiurnal coherence at both A1 (93%) and S9 (73%), so this mechanism could account for those values. The coherence of semidiurnal conversion at A1

in this model is 86%, close to the observed value of 88%.

Though these simple 2-D calculations neglect possible feedbacks that could change conversion, and do not include any scattering or dissipation, they provide a rough estimate of the possible magnitude of incoherence that these mechanisms could produce. The results suggest that the arrival of remote semidiurnal internal tides from the Mariana Arc could account for the observed semidiurnal incoherence at both A1 and S9, and that reflection of the diurnal internal tide from the continental shelf could account for the observed level of diurnal incoherence at S9. However, the observed $\sim 30\%$ coherence of the diurnal internal tide at A1 cannot be explained by these simple 2-D models.

To investigate further, we use the 3D LZS model and compute coherence in the same way as for the observations (Figure 4.16). Coherence in both frequencies is lower along the eastern ridge, especially south of 20^oN. The diurnal band (c) also has a region of low coherence extending to the northwest from the eastern ridge near 20.5^0N. Both diurnal and semidiurnal internal tides are largely coherent in the area of S9. A1 is located in a region of low diurnal coherence and higher semidiurnal coherence. A zonal transect (a) through A1 at 20.5N shows excellent agreement between model and observations. A transect through S9 (b) shows good agreement in the diurnal band, and slightly higher than observed coherence in the semidiurnal band. Since the model reproduces the observed patterns, we can use it to explore mechanisms for lowering coherence. Notably, since the model does not include remote waves from the Mariana Arc, more local effects appear responsible.

A clue to the diurnal incoherence at A1 is given in Buijsman et al. (2014), who identified a large gradient in the phase of mode-1 diurnal pressure at that location. We hypothesize that incoherence arises as the variable Kuroshio and mesoscale shifts this pattern back and forth, which Buijsman et al. (2014) were not able to examine since the MITgcm model did not contain mesoscale forcing. Here we compute the phase of mode-1 perturbation pressure from the LZS model using a sliding harmonic fit to the diurnal and semidiurnal frequencies

in overlapping 3 day windows. The diurnal phase (Figure 4.17 b,e) has a large gradient that runs from NW to SE, passing near A1 before continuing south along the eastern ridge. This pattern and strong north-south gradient between the ridges is similar to that seen in Buijsman et al. (2014), but appears to be less zonal near 20.5^{o}N, possibly due to the addition of the Kuroshio in the LZS model. The gradient of semidiurnal phase (Figure 4.17 c,f) is smaller at A1, in agreement with the higher coherence of that component. Near the location of S9, the gradient of diurnal phase is small and the semidiurnal phase gradient is larger, consistent with the relative levels of coherence observed there.

To test our hypothesis that shifting of this gradient is responsible for the lower coherence, we also examined the standard deviation of the baroclinic phase (not shown). It was generally largest where the largest gradients exist, consistent with this spatial pattern being advected or shifted laterally.

The shifting of the internal tide phase pattern must be caused by changes in stratification or velocity shear, which in Luzon Strait are dominated by the intrusion of the Kuroshio. Figure 4.17 shows the low-frequency velocity at 100 m at two different times (a,d). In the first period (top row), there is a weaker, more diffuse Kuroshio, and the white diurnal phase contour passes through A1 (b). In the second time period (bottom row), the Kuroshio is stronger and more jet-like and the diurnal phase pattern around A1 (e) appears to be shifted to the north. This suggests that the shifting of the diurnal pressure phase pattern is related to the low-frequency velocity or Kuroshio. However, the specifics of the interaction between the 3D internal tide response and the background flows are complicated, and beyond the scope of this paper.

4.7 Conclusions

The coherence and variability of internal tides in Luzon Strait were studied using measurements from two moorings deployed for 50 days during the IWISE experiment. The

observations reveal an extremely energetic internal wave field, with depth-integrated diurnal and semidiurnal energy fluxes up to 54(63) kWm^{-1}, respectively. Velocity spectra measured at the moorings were elevated up to 15 times above the theoretical GM spectrum (Figure 4.3), likely due to energy input from strong internal tides and implying elevated turbulent mixing rates. The modal distribution of internal tide energy flux was red, with most of the flux contained in the first 2 modes.

The temporal variability of the internal tide is quantified by computing the coherent component, described by a sum of tidal frequencies with constant amplitude and phase over the 50 day mooring deployment. The semidiurnal internal tide at A1 and both frequencies of internal tide at S9 were largely coherent (Table 4.2), with more than 70% percent of the energy flux variance explained by the coherent component. In contrast, the diurnal internal tide at A1 is significantly less coherent, with the coherent energy flux only 30% of the total. The phase and amplitude of diurnal perturbation pressure at A1 varies significantly over the mooring deployment, resulting in the low coherence.

Simple 2-D calculations suggest that reflection of the diurnal internal tide from the continental shelf and remote semidiurnal internal tides arriving from the Mariana Arc could account for the observed levels of coherence, with the exception of the diurnal internal tide at A1. Instead, the much lower coherence of the diurnal internal tide at A1 is a result of the mooring's location near a large gradient in the 3D pattern of baroclinic pressure phase. The LZS model, which contains a realistic Kuroshio and mesoscale variability, shows that changes in the Kuroshio intrusion into Luzon Strait occur at the same time as shifts of the internal tide phase pattern in Luzon Strait. However, the multiple sources and 3-D nature of the interference pattern makes it difficult to isolate the details of this mechanism. Continued progress will require a combination of data from many different observation platforms, combined with models such as the LZS that include the Kuroshio and mesoscale variability.

4.8 Acknowledgments

Collaborators on this work include Jonathan Nash, Dong-Shan Ko, Maarten Buijsman, and Byungho Lim. IWISE was funded by the Office of Naval Research (ONR). We thank the Captain and crew of the *RV Revelle* and *RV OR 1* for their skill and hard work to acquire these measurements. We would also like to thank John Mickett, Eric Boget, Zoë Parsons, Paul Aguilar, Tom Peacock, Amy Waterhouse, Ruth Musgrave, Hayley Dosser, Keshien Fu, and Chungwei Lu for their work in deploying the moorings and making shipboard measurements. This work was supported by ONR grants N00014-09-1-0219 (Dr. Alford and Rainville), N00014-11-1-0184 (Pickering), N00014-05WX-2-0647 (Dr. Ko), ONRDC32025354 (Dr. Buijsman), and N00014-09-1-0281 (Dr. Nash). IWISE would not have been possible without the hard work, talent and generosity of our Taiwanese colleagues, especially T.Y. Tang, Y. J. Yang, Yu-Huai Wang and Joe Wang. We particularly acknowledge Dr. Tang, who is no longer with us but will always be fondly remembered.

4.9 Appendix: Estimating Internal Wave Displacement from Temperature-chain Measurements with Mooring Knockdown

Extremely strong upper-ocean currents in Luzon Strait inhibited moored profilers from climbing at times during the pilot experiment. To prevent this issue during the main experiment, mooring S9 was redesigned with an upward looking ADCP and a temperature chain to measure the upper 300 m. The T-chain consisted of SBE-56 temperature loggers spaced about 15 m apart, with an upward looking ADCP at the bottom of the T-chain and a SBE-37 Microcat at the top of the T-chain. Here we discuss the correction of mooring knockdown in these measurements.

Mooring knockdown, determined from pressure measured at the top (SBE-37) and bottom (ADCP) of the T-chain, was up to $\sim$75 m during strong flows at spring tide. The instantaneous depth of each SBE-56 temperature sensor was calculated from the pressure recorded

Table 4.1: Time-mean, depth-integrated energy and energy flux for diurnal and semidiurnal internal tide at moorings S9 and A1. Direction is in degrees true (CW from N).

	diurnal			semidiurnal		
	$\bar{E}$	$\lvert\bar{F}\rvert$	$\bar{\theta}$	$\bar{E}$	$\lvert\bar{F}\rvert$	$\bar{\theta}$
	$\mathrm{kJm^{-2}}$	$\mathrm{kWm^{-1}}$	${}^{o}T$	$\mathrm{kJm^{-2}}$	$\mathrm{kWm^{-1}}$	${}^{o}T$
S9	24	25	339	15	14	313
A1	21	5	236	27	27	169

at the top and bottom of the T-chain, assuming that the T-chain remained a straight line between the top and bottom. This assumption can be tested by comparing the difference in depth between the top and bottom (δz) to the known length of the wire $L = 237$ m. The maximum value of $(L - \delta z)$ was about 10m, or about 4% of L, indicating that this is a good assumption. The cable could be slightly curved instead of in a straight line.

Figure 4.9 shows temperature plotted at the nominal depth of the T-chain instruments (a) and after interpolating to the actual depth (b). Without correction, large mooring blowdowns during spring tides (i.e. day 183) would be interpreted as extremely large vertical displacements. These vertical displacements have a large effect on the internal tide energy flux.

Table 4.2: Percent variance of observed mode-1 energy, flux, and conversion explained by coherent portion at moorings A1 and S9.

	APE	HKE	Fu	Fv	F	C
A1 - D1	16	80	38	30	24	31
A1 - D2	83	79	53	85	84	88
S9 - D1	90	72	85	84	88	94
S9 - D2	65	60	57	61	74	67

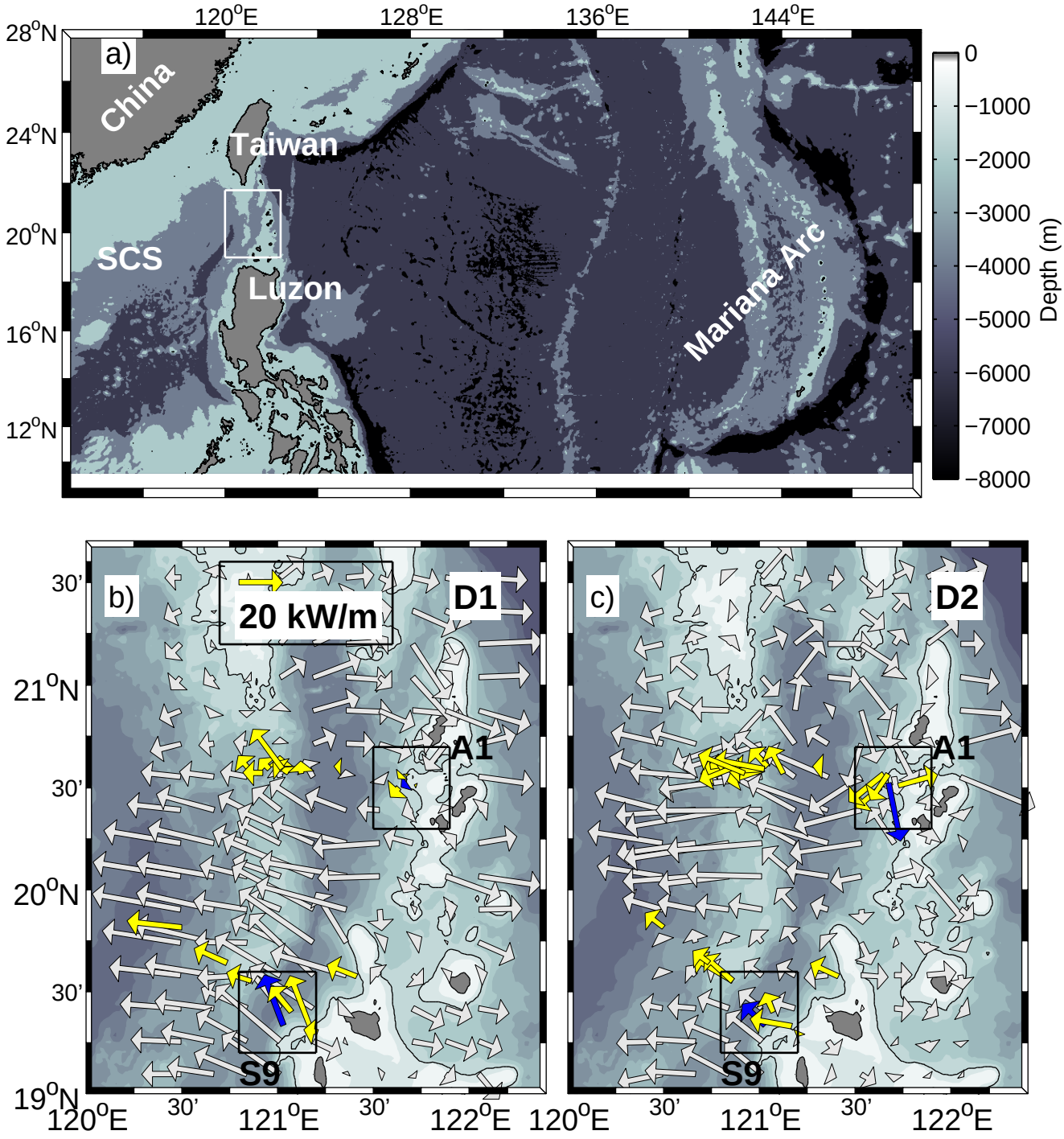

Figure 4.1: (a) Map of larger region, including Mariana Arc and South China Sea (SCS). (b,c) Map of Luzon Strait with mooring locations and depth-integrated diurnal (b) and semidiurnal (c) energy fluxes. Modeled MITgcm energy fluxes are shown in white. Fluxes measured from LADCP/CTD stations are shown in yellow. Time-mean fluxes from moorings A1 and S9 are shown in blue. Boxes around these moorings indicate regions shown in figure 4.10. The 1000m isobath is contoured.

.

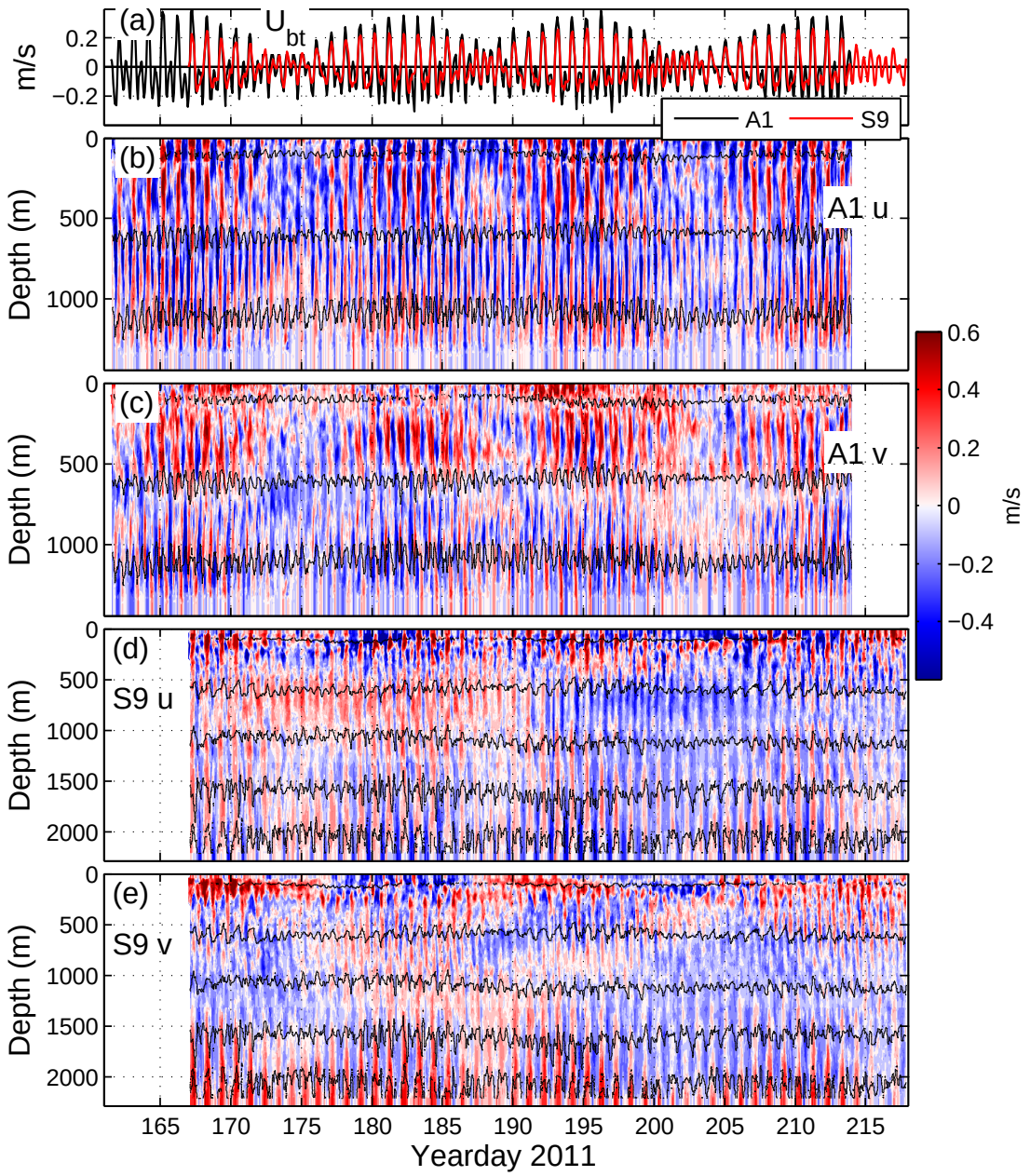

Figure 4.2: Raw data from moorings A1 and S9. (a) Zonal component of barotropic (depth-mean) velocity. (b) A1 zonal velocity (c) A1 meridional velocity (d) S9 zonal velocity (e) S9 meridional velocity. Black lines are isopycnal contours at 500m intervals.

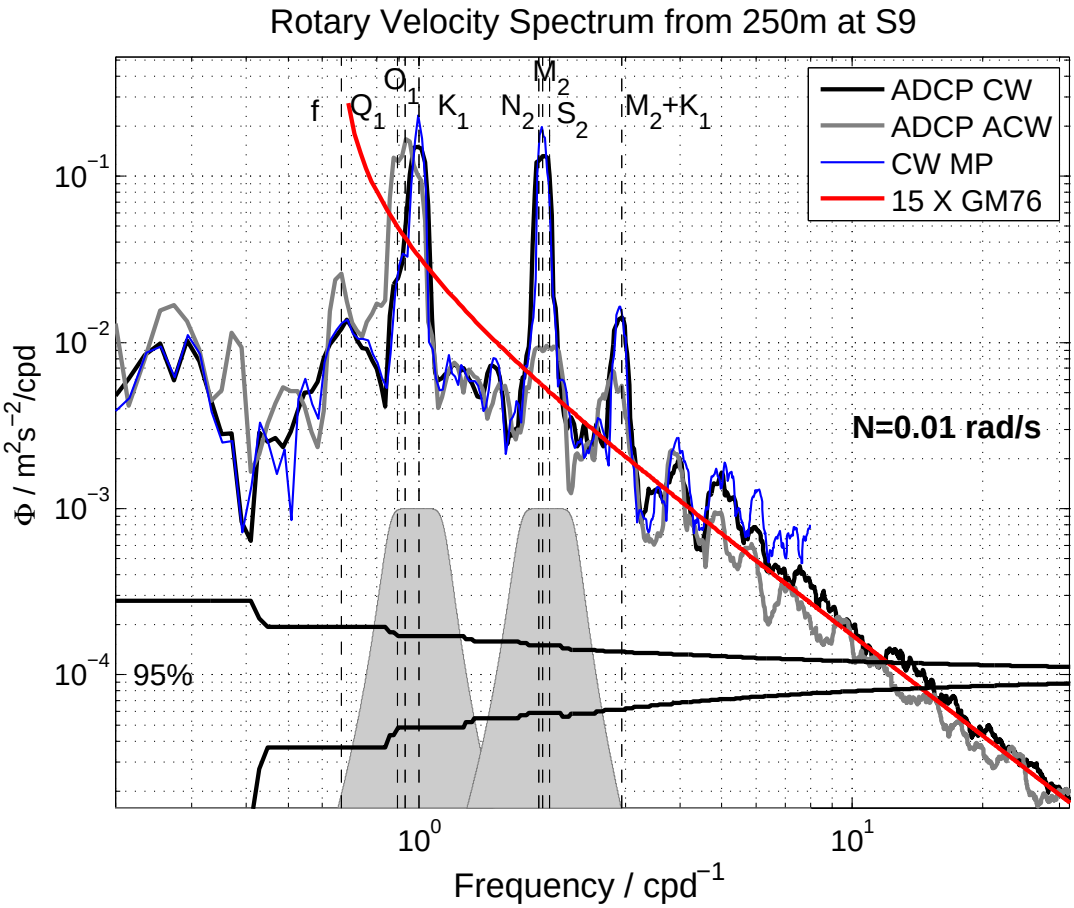

Figure 4.3: Rotary spectrum of baroclinic velocity at 250m at mooring S9. Spectra of the raw velocity measured by an upward looking 75kHz ADCP are shown in black (clockwise) and gray (counter-clockwise). The clockwise spectrum of the gridded MP velocity is plotted in blue. Gray shading shows the (scaled) frequency response of the bandpass filter used to isolate diurnal and semidiurnal frequencies. Dashed red line is 15× the theoretical GM76 spectrum for the mean N at that depth.

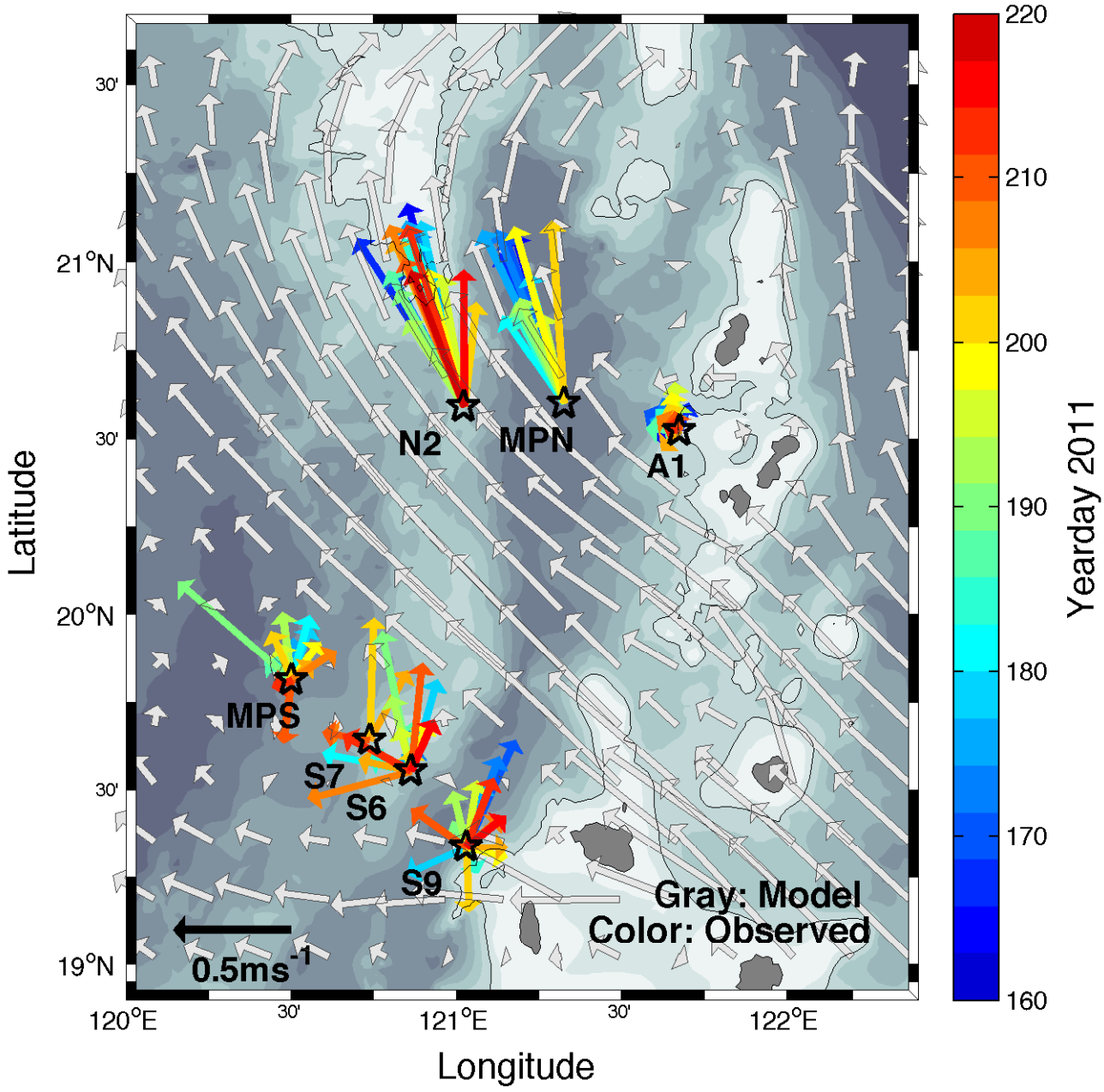

Figure 4.4: Low-frequency velocity across Luzon Strait during the experiment. Colored vectors show low-pass filtered velocity at 150m from mooring array. Gray vectors are time-mean velocity vectors at 150m from the LZS model during the experiment.

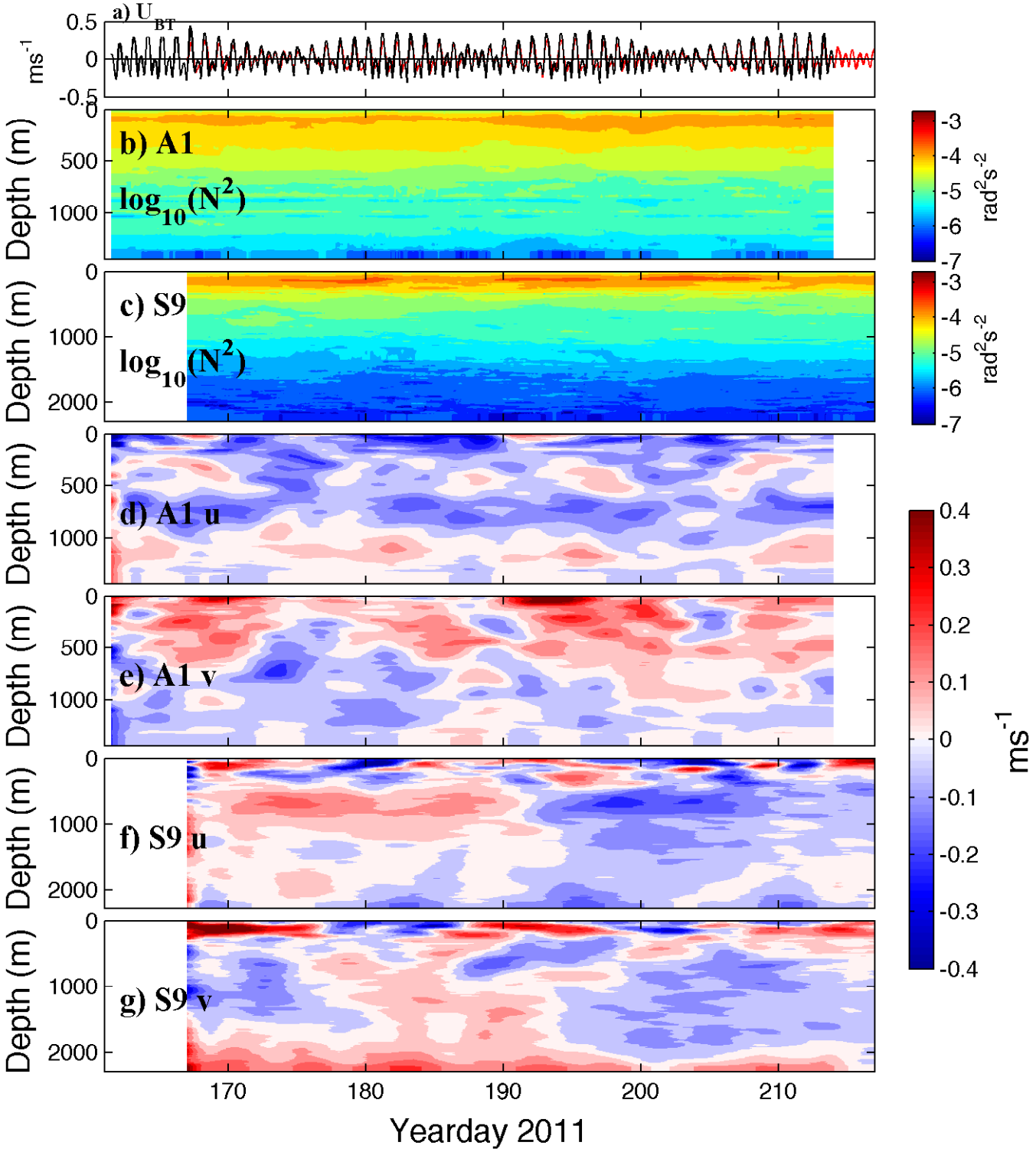

Figure 4.5: Low-pass filtered stratification and velocity (4 day cutoff) at S9 and A1. (a) Zonal barotropic velocity at S9 (red) and A1 (black). (b) Stratification at A1. (c) Stratification at S9. (d) Zonal velocity at A1. (e) Zonal velocity at S9. (f) Meridional velocity at A1. (g) Meridional velocity at S9.

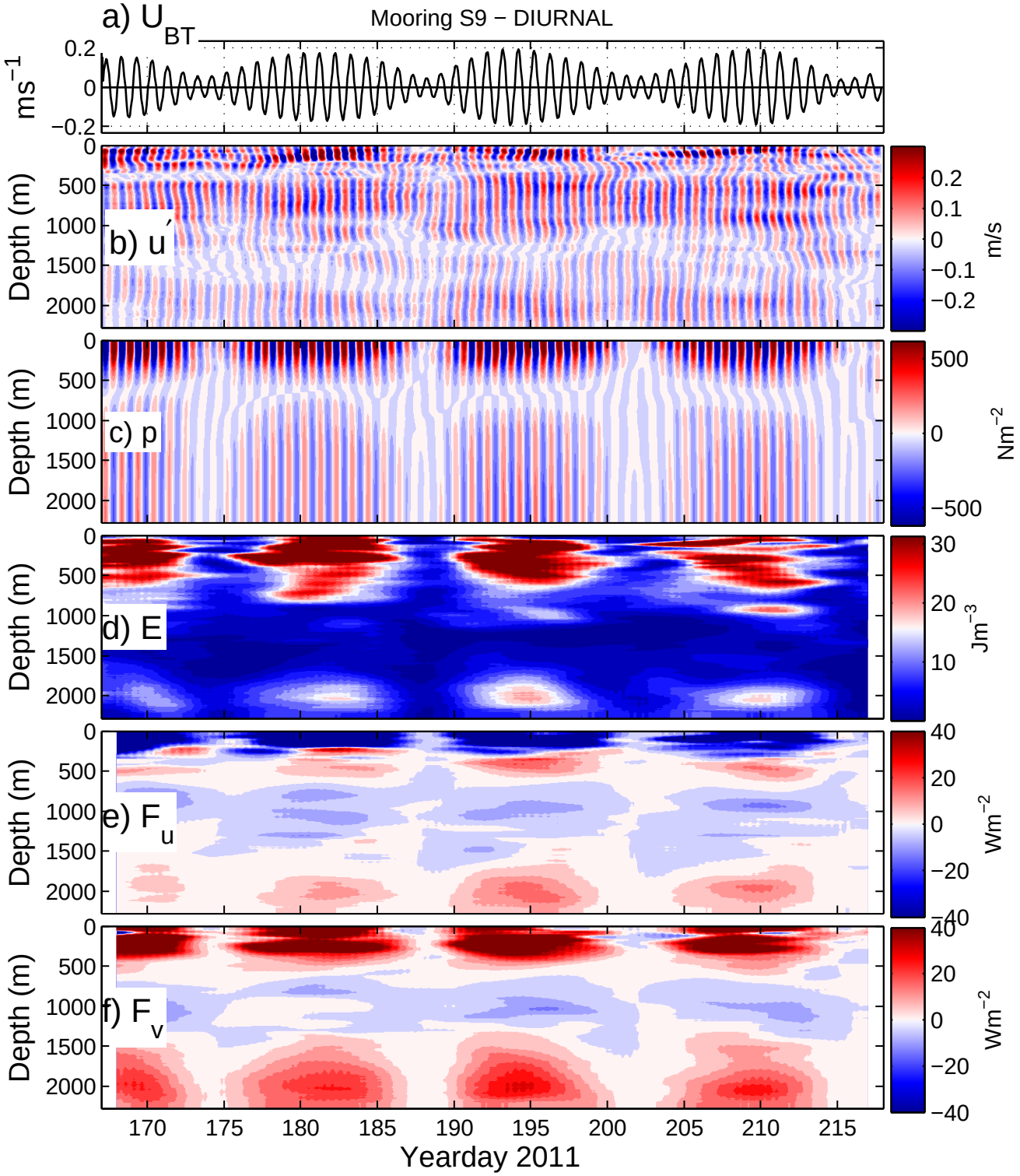

Figure 4.6: Diurnal internal tide quantities at S9: (a) Barotropic velocity u_{BT}, (b) baroclinic zonal velocity (c) perturbation pressure (d) energy (HKE+APE) (e) zonal energy flux (f) meridional energy flux.

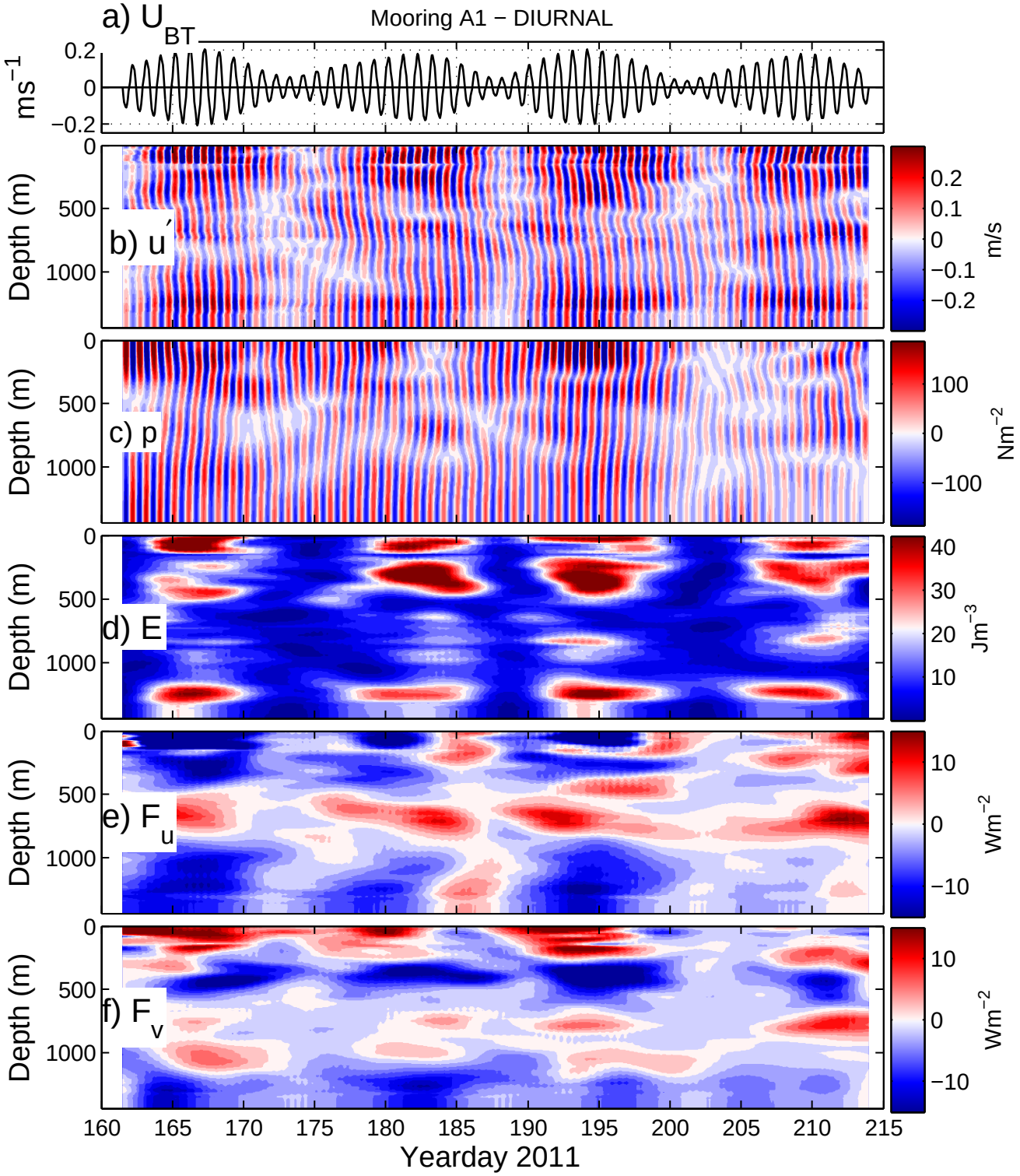

Figure 4.7: Diurnal internal tide quantities at A1: (a) Barotropic velocity u_{BT}, (b) baroclinic zonal velocity (c) perturbation pressure (d) energy (HKE+APE) (e) zonal energy flux (f) meridional energy flux.

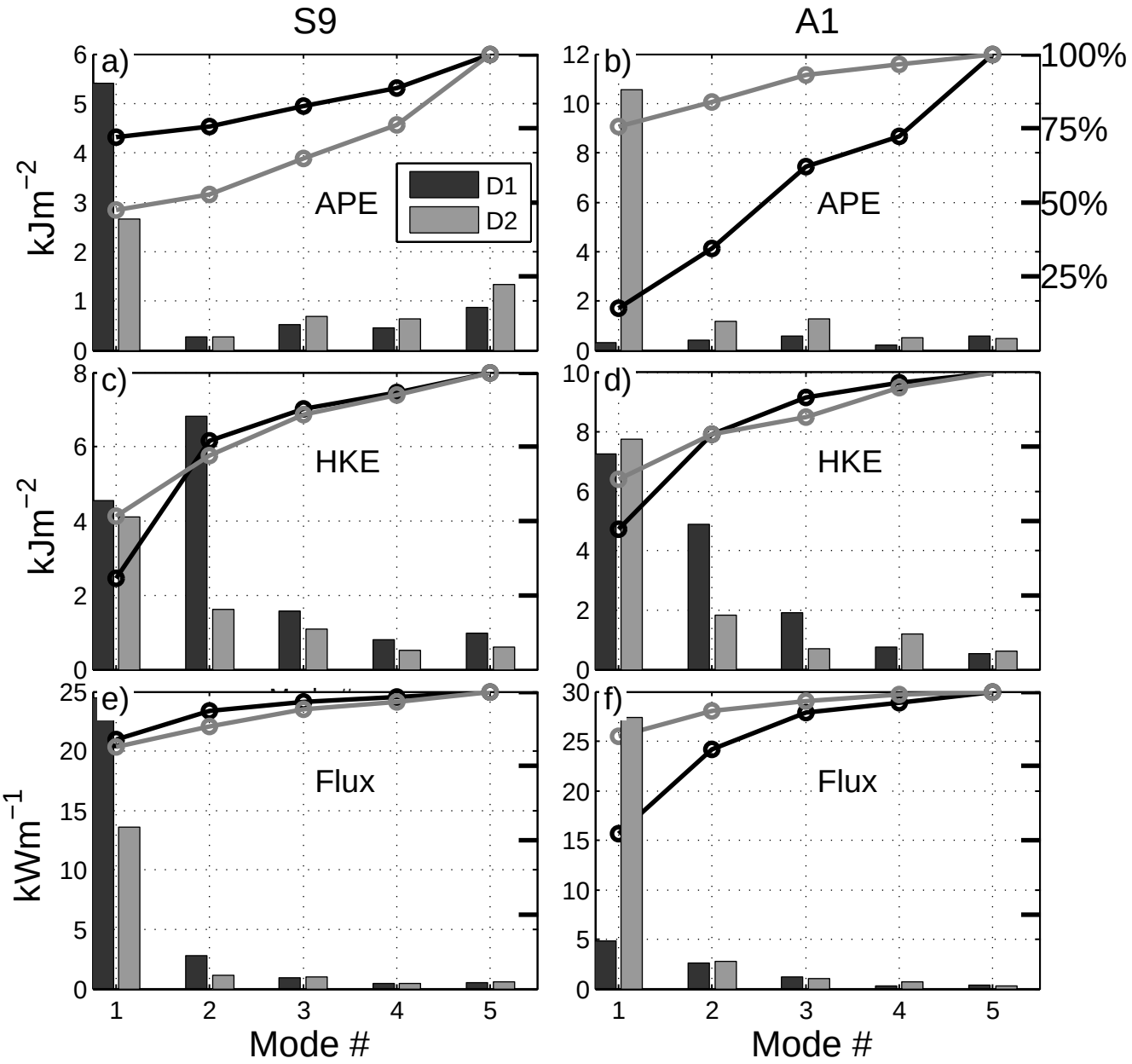

Figure 4.8: Modal distribution of APE (top), HKE (middle), and energy flux (bottom) at S9 (left) and A1 (right). Lines with circles show the cumulative percent total, with scale at upper right.

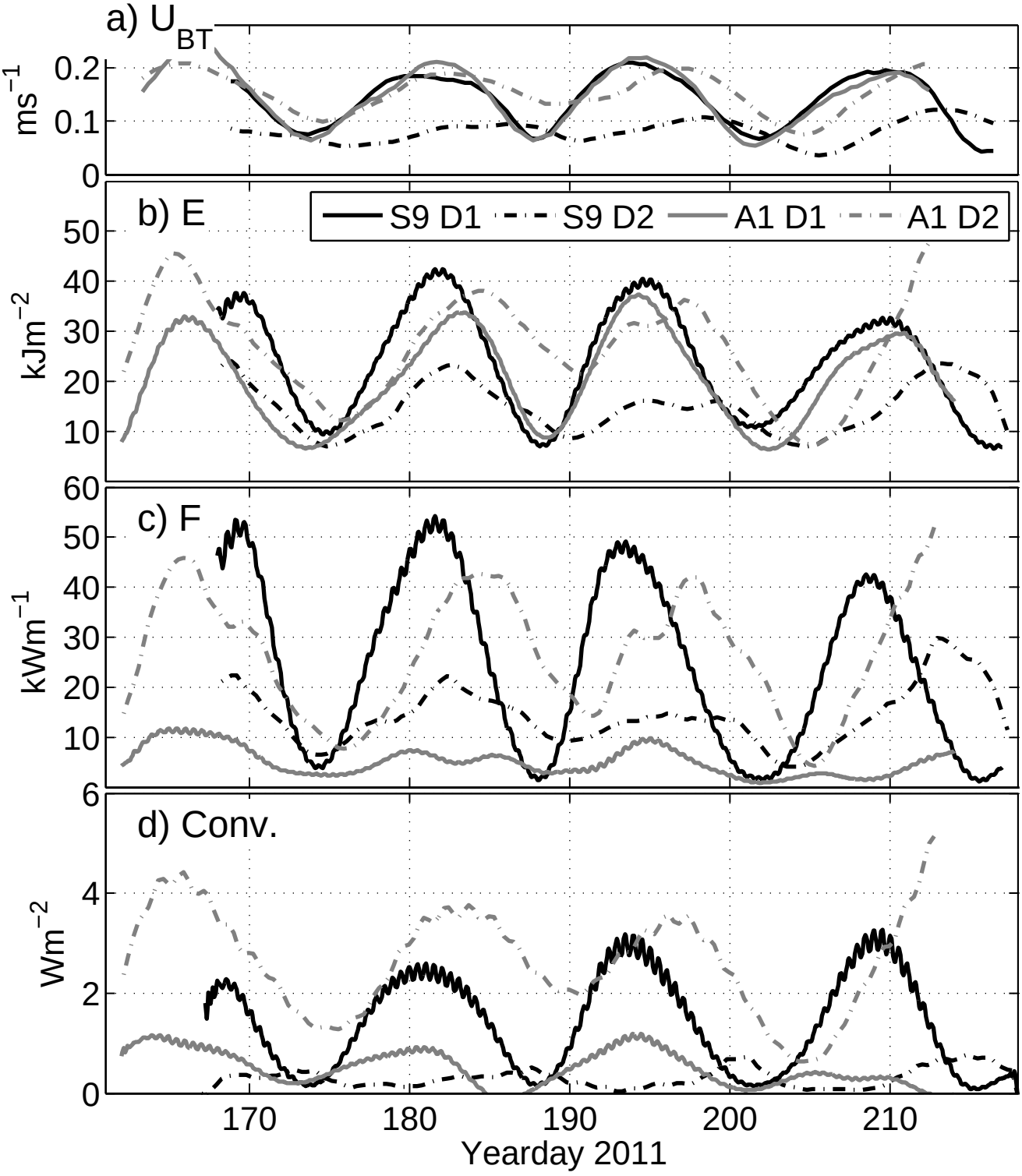

Figure 4.9: Time-series of depth-integrated internal tide quantities at moorings S9 (black) and A1 (gray). Diurnal quantities are shown with solid lines, and semidiurnal are shown with dashed lines. (a) Barotropic velocity amplitude. (b) Depth-integrated energy (HKE + APE). (c) Depth-integrated energy flux magnitude. (d) Barotropic to baroclinic conversion.

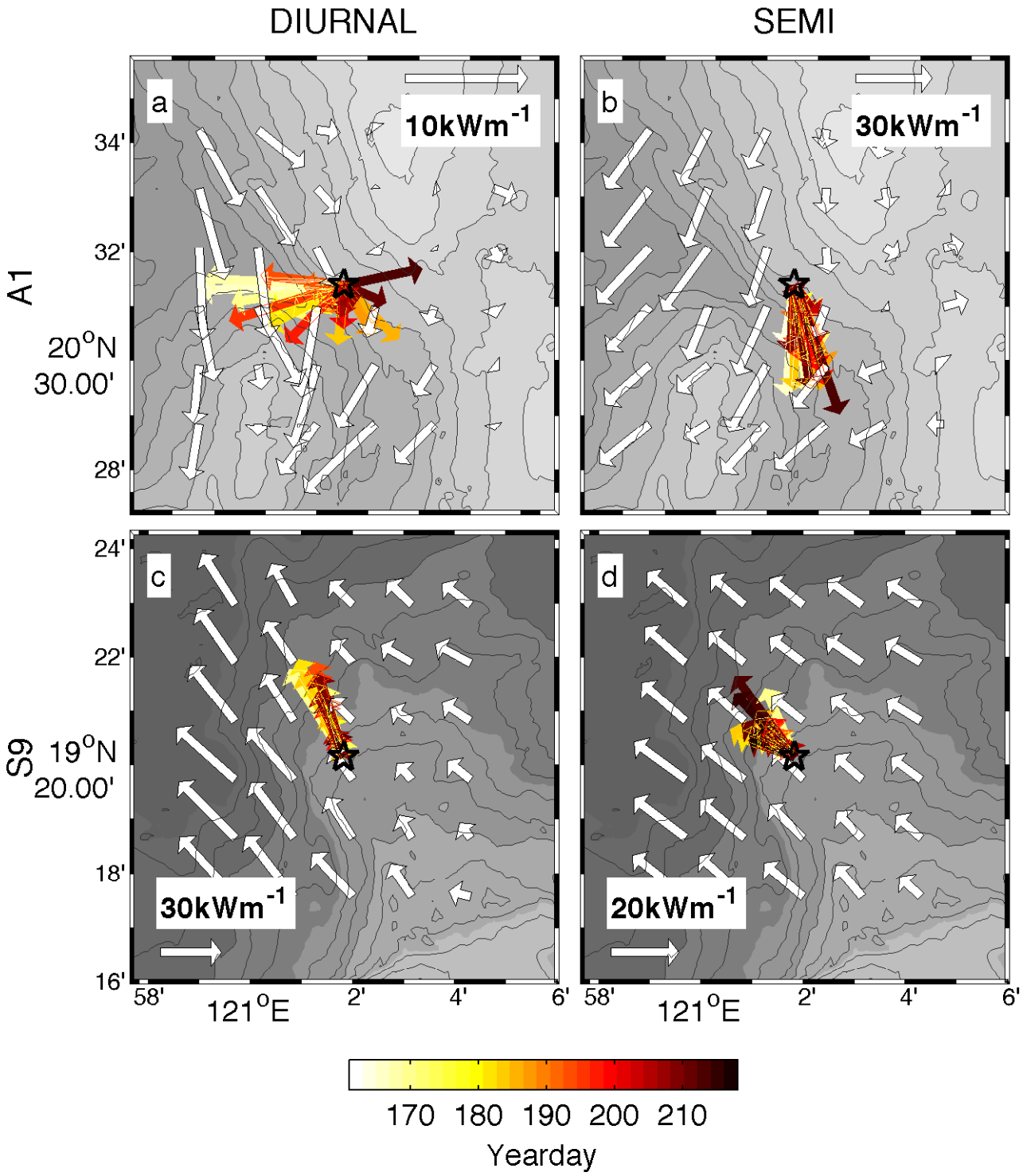

Figure 4.10: Diurnal (left) and semi-diurnal (right) depth-integrated energy fluxes at moorings A1 (top) and S9 (bottom). White vectors are time-mean modeled (MITgcm) fluxes. Observed fluxes are colored by time.

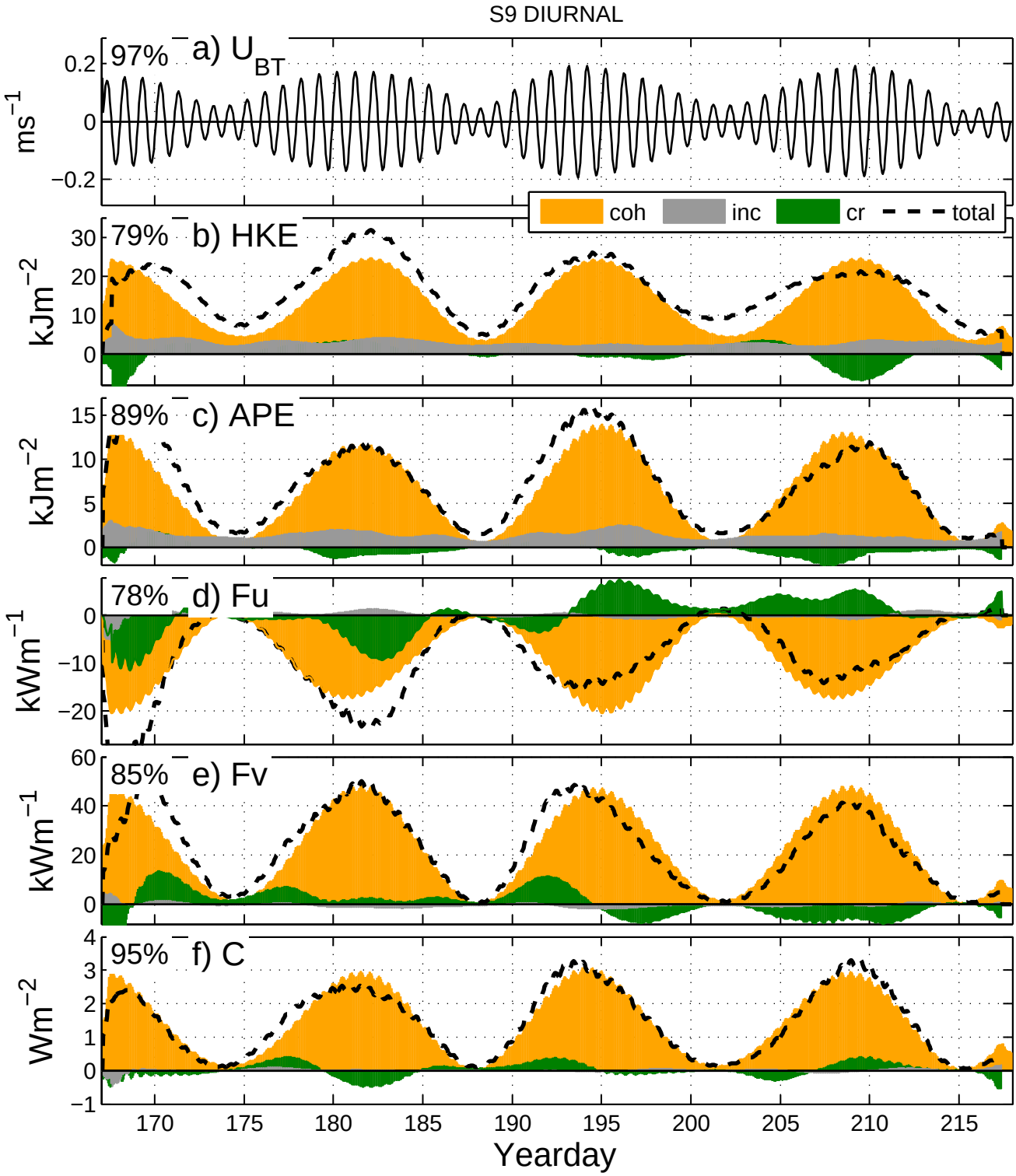

Figure 4.11: Results of coherent/incoherent separation for diurnal band at S9. a) Zonal barotropic velocity. b) HKE. c) APE . d) Zonal energy flux. e) Meridional energy flux. f) Conversion. Coherent, incoherent, and cross-term components are shown in color. Dashed black line shows the total of each quantity. Number in upper left of each panel indicates the

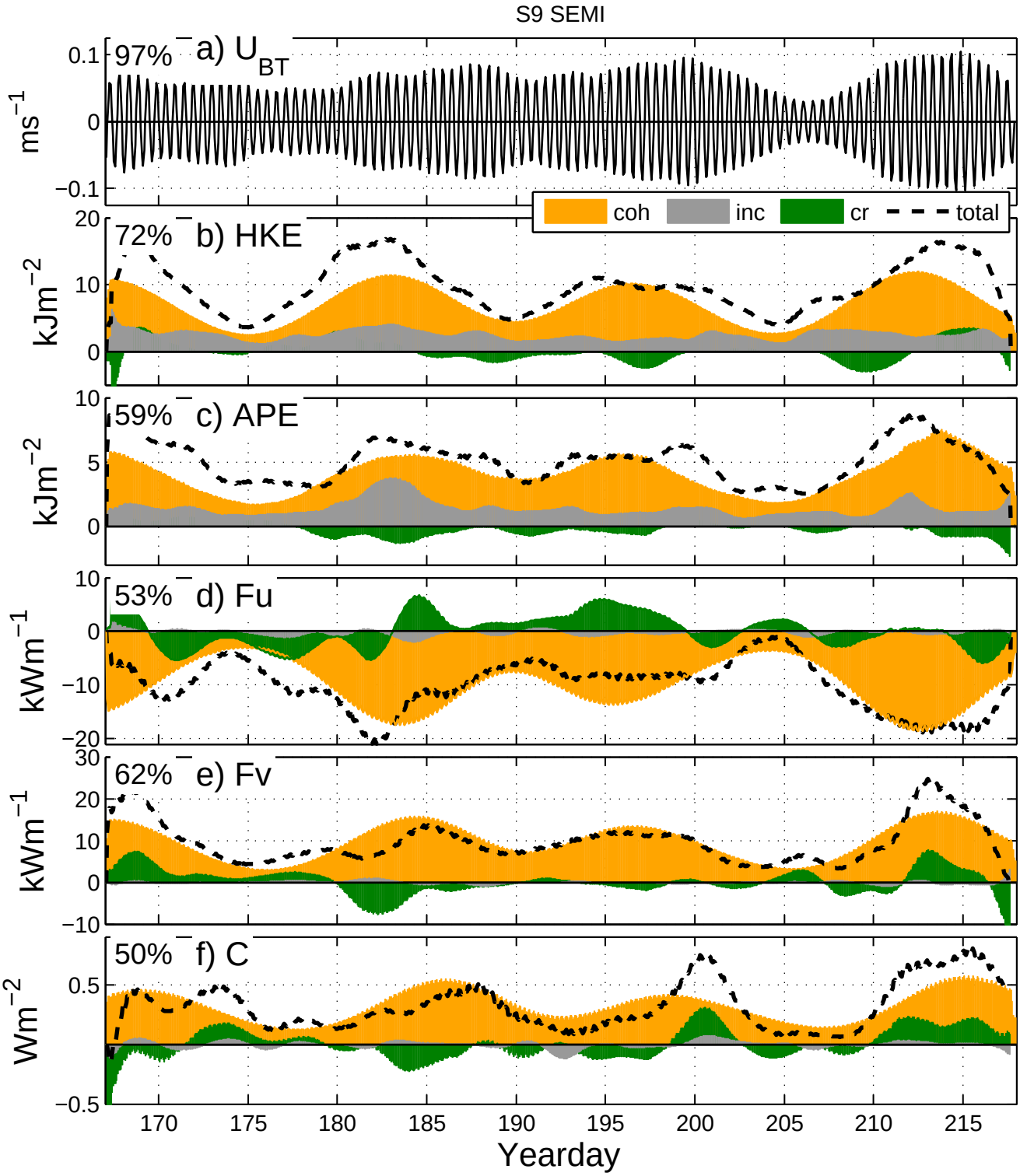

Figure 4.12: Results of coherent/incoherent separation for semidiurnal band at S9. a) Zonal barotropic velocity. b) HKE. c) APE . d) Zonal energy flux. e) Meridional energy flux. f) Conversion. Coherent, incoherent, and cross-term components are shown in color. Dashed black line shows the total of each quantity. Number in upper left of each panel indicates the

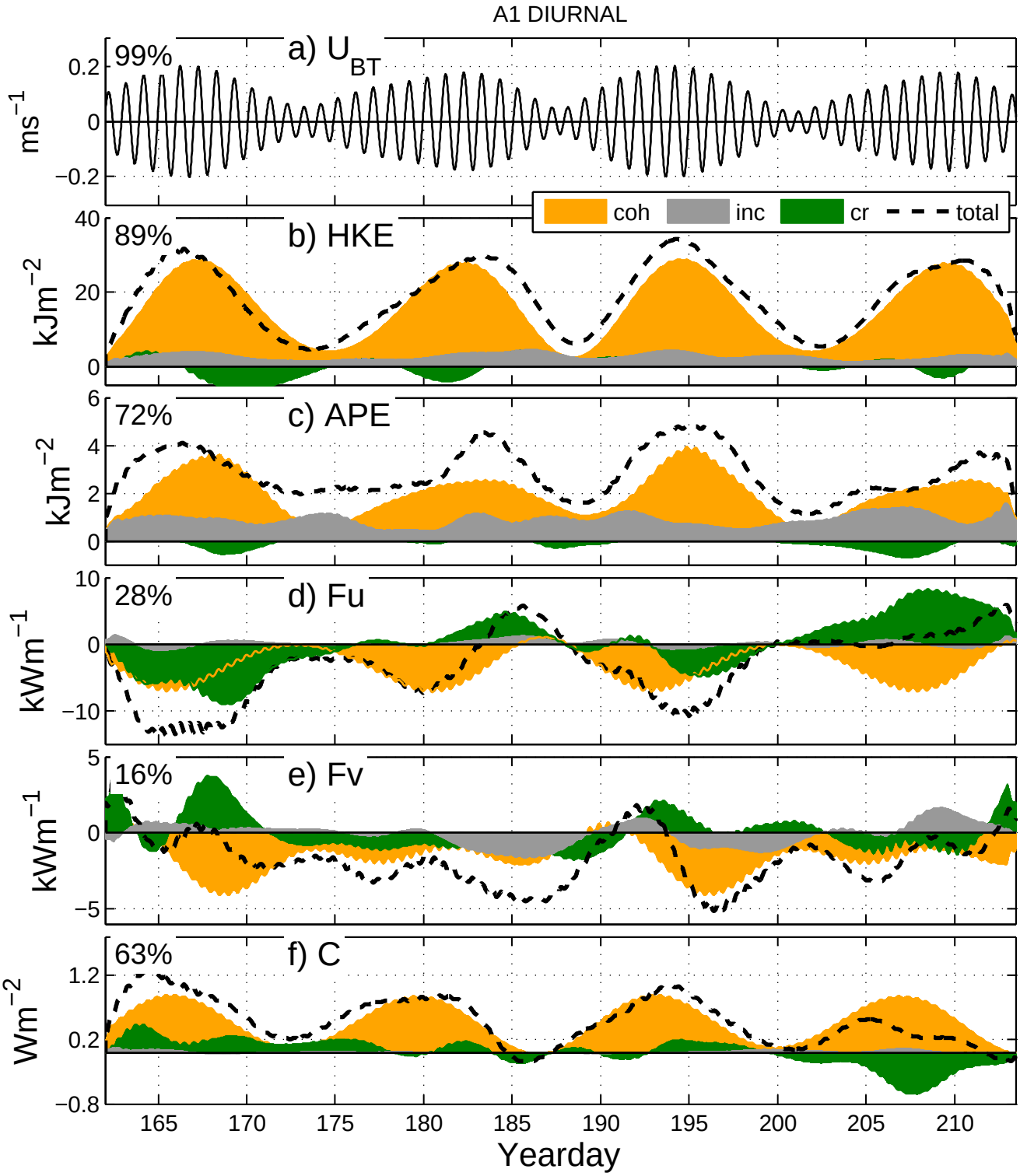

Figure 4.13: Results of coherent/incoherent separation for diurnal band at A1. a) Zonal barotropic velocity. b) HKE. c) APE . d) Zonal energy flux. e) Meridional energy flux. f) Conversion. Coherent, incoherent, and cross-term components are shown in color. Dashed black line shows the total of each quantity. Number in upper left of each panel indicates the

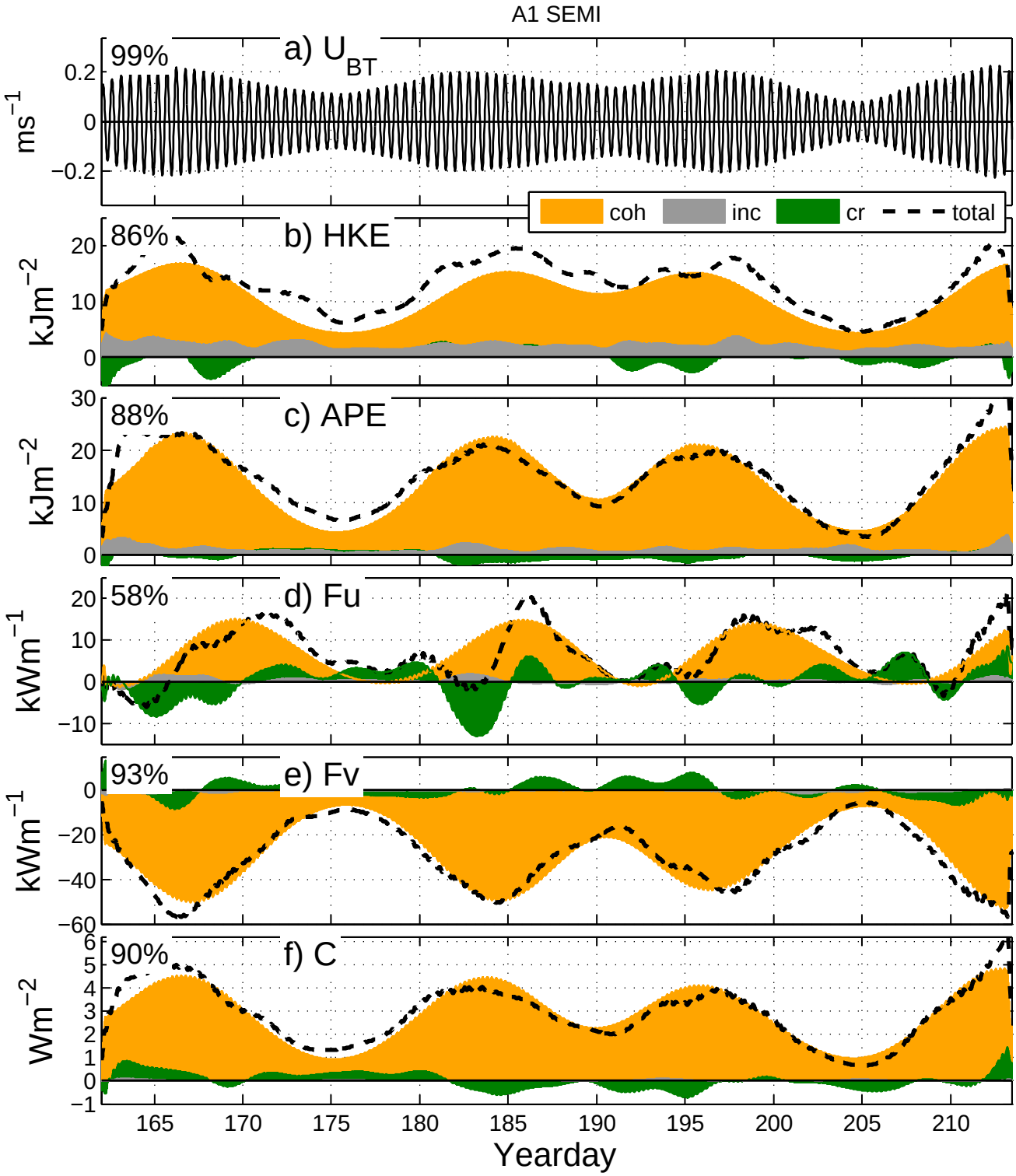

Figure 4.14: Results of coherent/incoherent separation for semidiurnal band at A1. a) Zonal barotropic velocity. b) HKE. c) APE . d) Zonal energy flux. e) Meridional energy flux. f) Conversion. Coherent, incoherent, and cross-term components are shown in color. Dashed black line shows the total of each quantity. Number in upper left of each panel indicates the

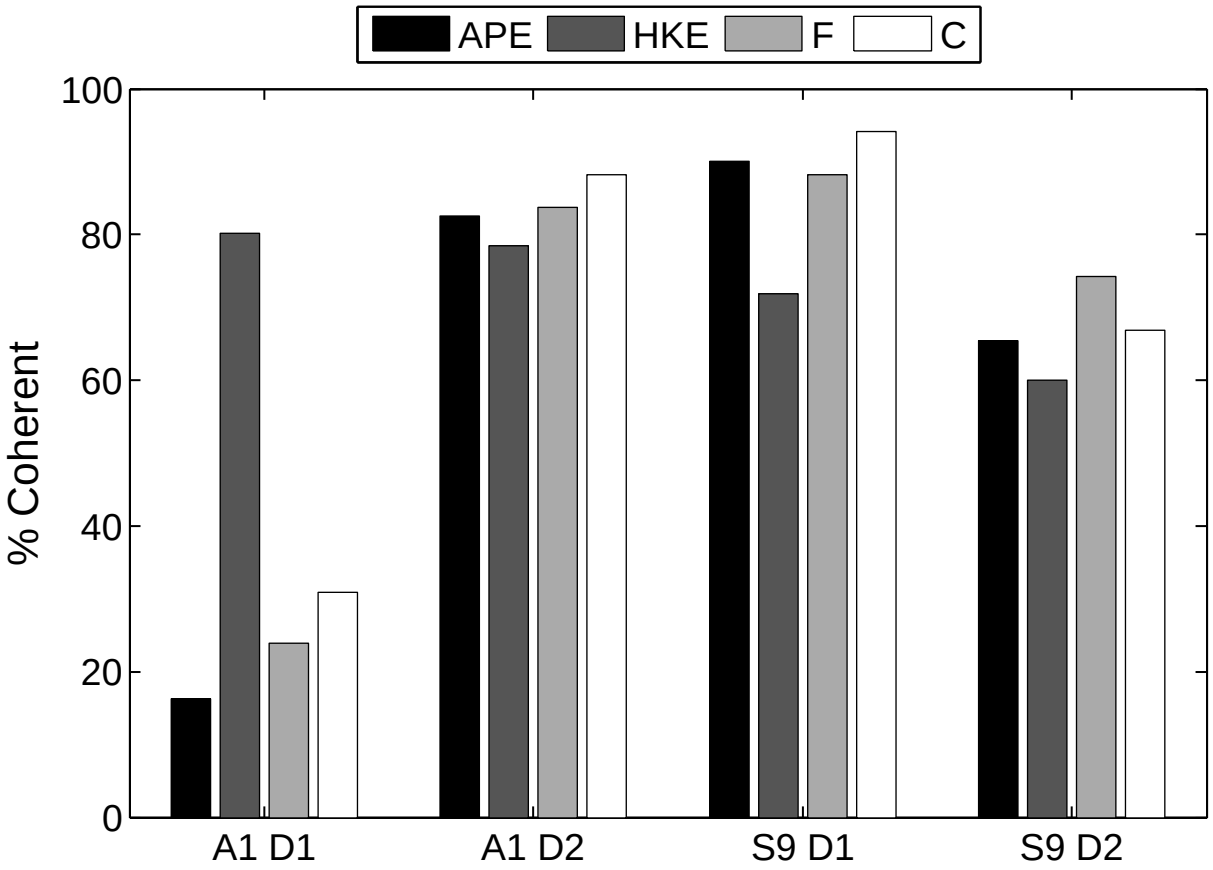

Figure 4.15: Percent coherence of internal tides at A1 and S9 in both frequency bands, computed via Eq 4.34.

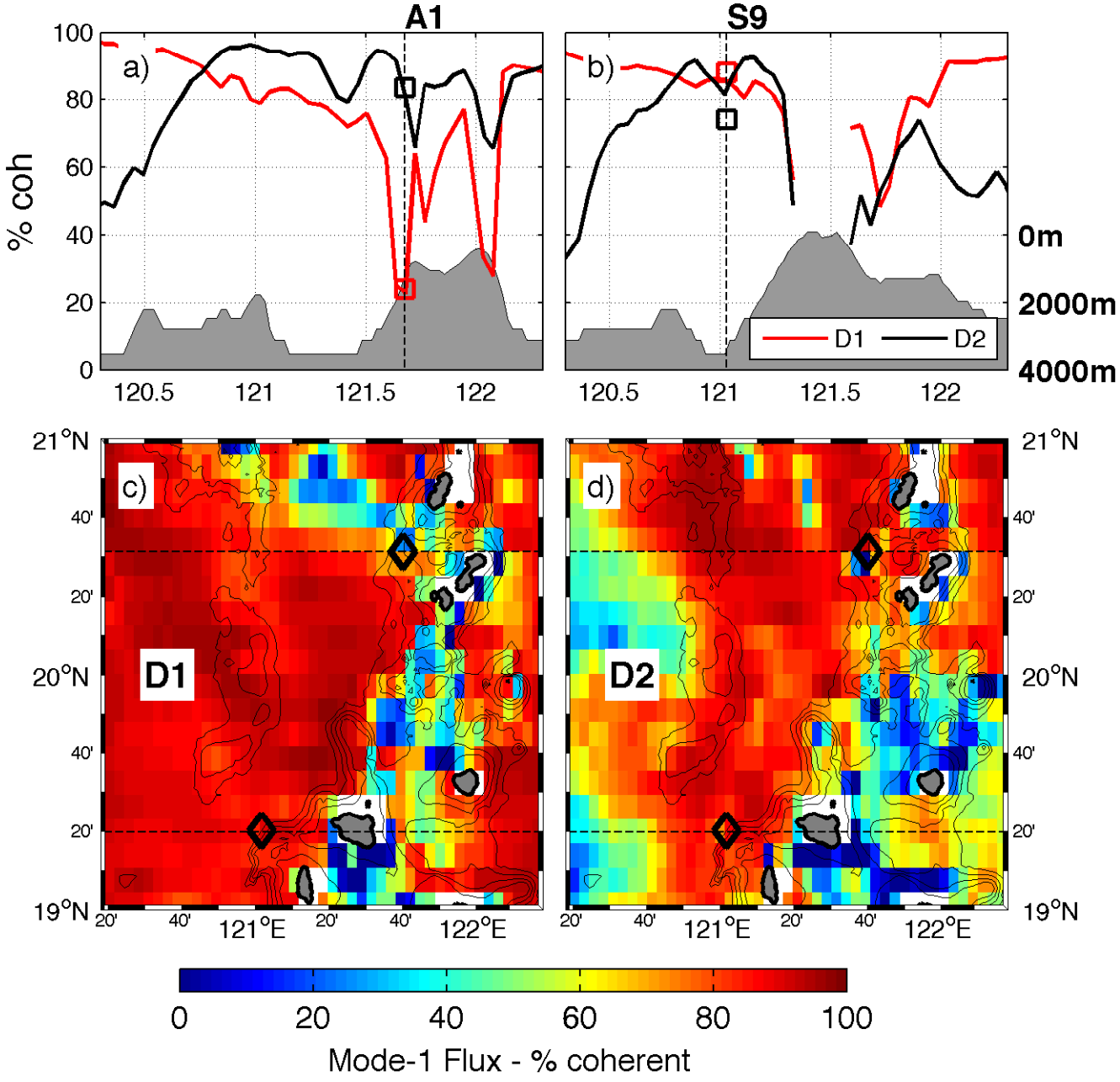

Figure 4.16: Percent variance of mode-1 energy flux explained by coherent component in LZS model. (a) Cross-section along 20.52 N (through A1) (b) Cross-section along 19.3 N (through S9). Observed values from moorings are plotted as squares. Bathymetry along cross sections is shown in gray, with a scale at lower right of panel (b). (c) Diurnal band. (d) Semidiurnal band. Dashed lines in (c) and (d) indicate location of cross-sections.

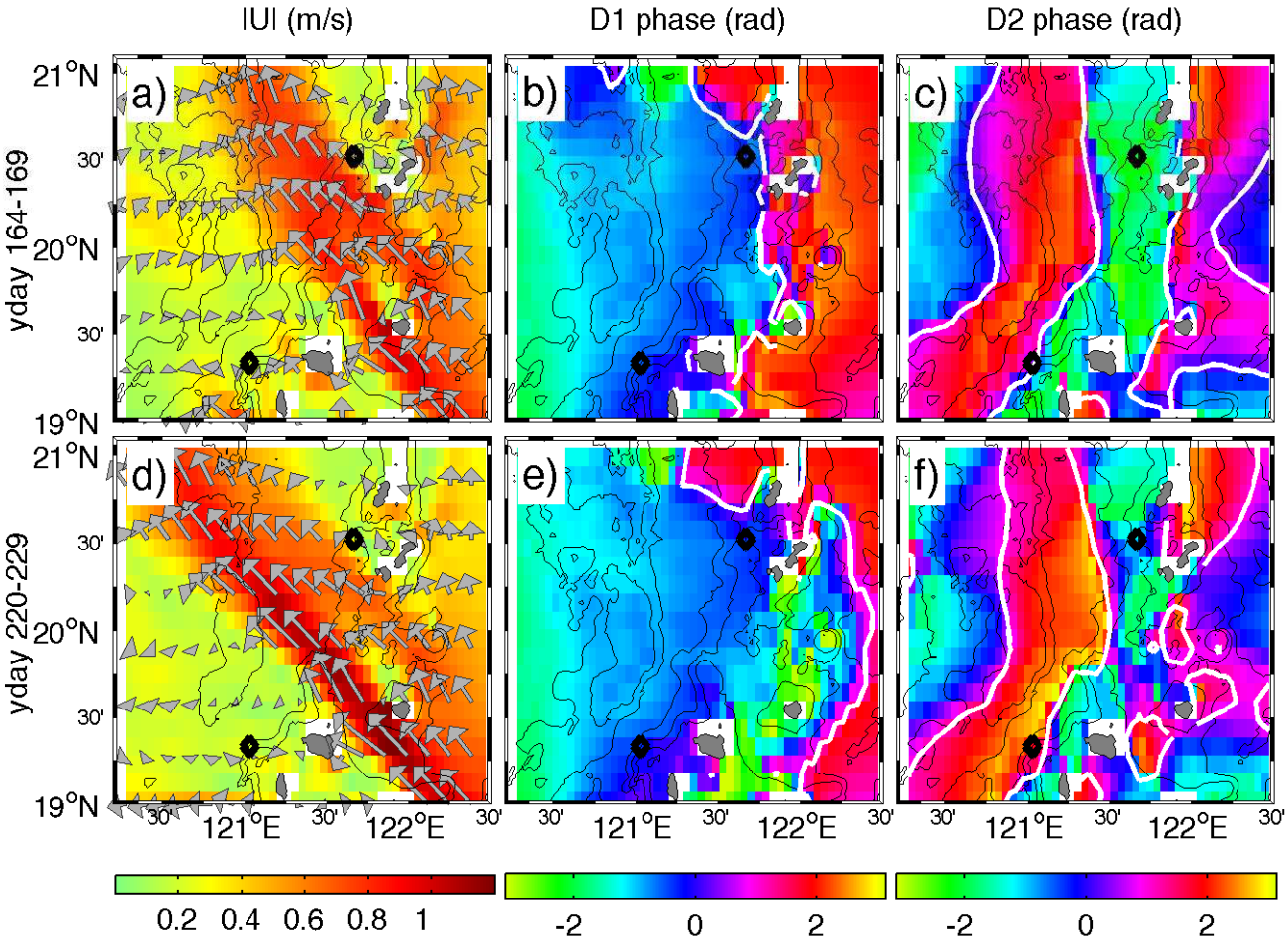

Figure 4.17: Figure showing the low-frequency velocity at 100m (left) and phase of diurnal (middle) and semidiurnal (right) mode-1 pressure for two time periods (top and bottom) of the LZS model. The same phase value is contoured in white to show the shifting of the phase pattern. A constant offset is added to phases in 2nd time period to account for different barotropic phases.

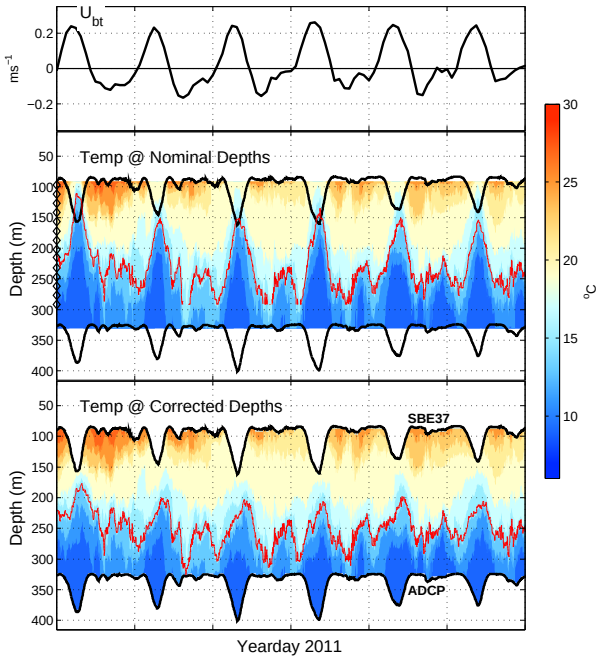

A1Figure illustrating removal of mooring blowdown from T-chain measurements at S9, and effect on calculated vertical displacement. (a) Zonal barotropic velocity. (b)Thermistor-string temperature plotted versus nominal depth of instruments. Black lines indicate depth of SBE-37 and ADCP at top and bottom of T-chain, respectively. (c) Temperature corrected for mooring blowdown using pressure measured at top and bottom of T-chain. The 15^{o}C isotherm is contoured in red in (b) and (c) to illustrate the effect of blowdowns on inferred vertical displacement.

Chapter

TIDALLY FORCED TURBULENT DISSIPATION ON A SLOPE IN LUZON STRAIT

5.1 Abstract

We present observations of flow and turbulent mixing on a supercritical slope in southeastern Luzon Strait from a mooring deployed in the summer of 2011 as part of the Internal Waves In Straits Experiment (IWISE). Two stacked moored profilers, an Acoustic Doppler Current Profiler (ADCP) and a thermistor string measured horizontal velocity, density, and salinity over nearly the entire water column for 50 days. Large velocities and vertical displacements are observed near the bottom and vary strongly with the tidal forcing. Turbulent dissipation rate is computed from Thorpe scales and exhibits a strong spring-neap cycle, varying by an order of magnitude between spring and neap. High-resolution MITgcm model runs are compared to the observations and used to interpret the spatial structure and evolution of the flow and turbulence observed at the mooring. The model cross-section confirms the formation of lee-waves formed by tidal flow over the ridge, which break and lead to turbulent mixing. The 3D nature of the topography results in spatially variable flow and mixing over the slope. Depth-integrated dissipation largely scales with barotropic forcing but varies over different spring tides, suggesting that mesoscale velocity variability modulates the turbulent mixing.

5.2 Introduction

Quantifying and understanding turbulence, and the processes that create it, is an important but challenging goal of oceanographic research. On a global scale, turbulent mixing helps

maintain the oceans overturning circulation by mixing cold, dense abyssal water with lighter water above it (Munk and Wunsch, 1998). Turbulent mixing creates lateral density gradients that drive circulations, and redistributes nutrients important for biological productivity. It is also a sink for energy from the ocean circulation and tides, and thus important to quantify in order to construct accurate energy budgets. The location and magnitude of mixing has been shown to significantly affect the circulation in global climate models (Jayne, 2009; Melet et al., 2013b). Although mixing can have important affects on the larger-scale circulation, it occurs on much smaller scales than most models resolve and needs to be parameterized. Quantifying and understanding the processes leading to turbulence is essential in order to develop accurate parameterizations.

Breaking internal lee waves are one important source of mixing. They have previously been observed in coastal and fjord environments, but not in the open ocean until recently. Deep turbulent events phase locked to the tidal forcing were observed during the Hawaii Ocean Mixing Experiment (HOME) (Levine and Boyd, 2006; Aucan et al., 2006; Klymak et al., 2008). Subsequent modeling showed that these events were due to breaking lee waves that are generated by tidal flow over the ridge and swept over the ridge when the flow reverses (Legg and Klymak, 2008; Klymak et al., 2010). Alford et al. (2014) observed the time-evolution of these internal lee waves at Kaena ridge, confirming the model predictions.

At Luzon Strait, strong barotropic tidal flow over two ridges generates some of the world's largest internal tides. The internal wave field in Luzon Strait is complicated by the 3D bathymetry, frequent intrusions of the Kuroshio current, and strong mesoscale variability. While a large fraction of the energy lost from the barotropic tide at Luzon Strait radiates away as low-mode internal tides, a significant amount of dissipation occurs locally in the form of breaking lee waves (Alford et al., 2011; Buijsman et al., 2012, 2014). Observations made in Luzon Strait in 2010 as part of the Internal Waves In Straits Experiment (IWISE) revealed extremely large density overturns and turbulence levels on the ridge slopes (Alford

et al., 2011). Buijsman et al. (2012) used a 2D model to confirm the formation and breaking of lee waves on the western ridge at 20.6^{o}N, also showing that dissipation at this location was increased during semidiurnal forcing due to a resonance between the two ridges.

In the summer of 2011, a mooring array was deployed in Luzon Strait as part of the IWISE experiment, with the goal of observing these processes over multiple spring-neap tidal cycles and different mesoscale states. Here we present observations from one mooring (S9) deployed in southeast Luzon Strait (Figure 5.1). The topography at this location is more complex and barotropic flow is not as perpendicular to the slope, in contrast to the northern portion of the Strait where lee wave formation and dissipation may be well approximated by parameterizations based on flow over 2-dimensional ridges.

The goals of this analysis are to: (1) Document observations of flow and turbulence on a supercritical ridge. (2) Compare these to model predictions and assess how well they agree with the observations. (3) Use the model to better understand the spatial structure of the observations. (4) Investigate how dissipation varies with tidal forcing over several spring-neap cycles.

5.3 Data and Methods

5.3.1 Mooring

Mooring S9 (121 E,19.3 N) was located on a slope on the eastern ridge in southern Luzon Strait (Figure 5.1) at a depth of 2286m. The mooring consisted of two stacked McLane Moored Profilers (MP), sampling depths of 330-1260m and 1300-2230m, respectively. The MP profiles at 25 cm/s, resulting in a profile approximately every 1.5 hrs. Velocity and density are estimated with a vertical resolution of 10 m and 2m, respectively. Near-surface velocity was measured by an upward looking long-ranger deployed at 300m. Two SBE39 temperature sensors were deployed below the MP at depths of 2216m and 2222m, sampling at 25 sec intervals. Near-surface temperature was measured with SBE56 temperature sensors. In this analysis we focus mainly on the lower MP and SBE39's, below 1400m.

5.3.2 Model

The Massachusetts Institute of Technology General Circulation Model (MITgcm) (Marshall et al. 1997) was used in a 3D configuration, as described in Buijsman et al. (2014). The model uses realistic topography merged from high resolution gridded multibeam data with a resolution of ∼300m and 30-arc second resolution global topography/bathymetry grid (`SRTM30_PLUS`) data from the Smith and Sandwell database with a resolution of ∼1 km (Smith and Sandwell 1997). It has 150 vertical levels, with 250m horizontal resolution (telescoped to boundaries). A horizontally uniform, depth-varying stratification is used,

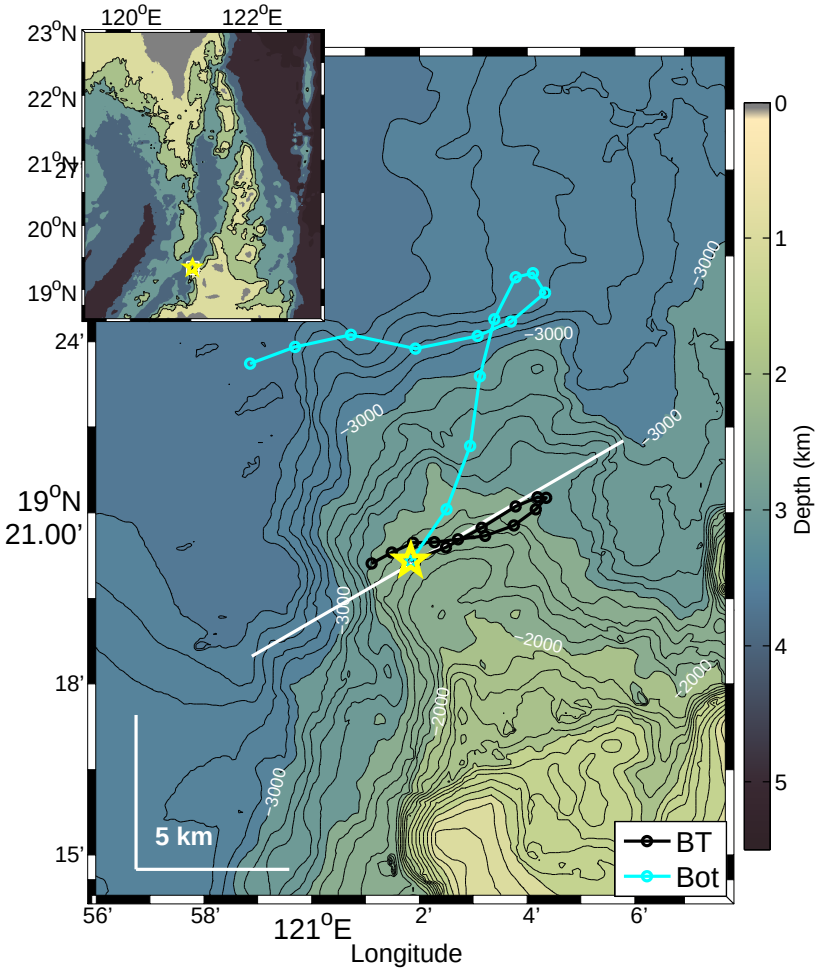

Figure 5.1: Upper Left Inset: Map showing entire Luzon Strait region and bathymetry (contoured at 100m intervals). Yellow star indicates position of mooring S9. Main panel: Detailed map of mooring location (yellow star) and bathymetry contours. White line shows the position of the model transect discussed in text. Black circles and line show depth-mean velocity integrated over 1day. Cyan shows the mean velocity in the lower 500m integrated over 1 day.

derived from temperature and salinity data collected in between the ridges (Alford et al., 2011). The tidal forcing at the east, west, north, and south model boundaries is composed of barotropic velocities extracted from TPXO7.2 (Egbert and Erofeeva, 2002). Dissipation is computed in the model from Thorpe sorting using the scheme of Klymak and Legg (2010). The model was run for yeardays 207-214 of 2011, overlapping with a portion of the mooring measurements.

5.3.3 Dissipation

Turbulent dissipation rate ϵ was estimated from Thorpe scales L_T (Thorpe, 1977; Dillon, 1982), the vertical distance a water parcel is displaced to form a stable, sorted density profile. The Thorpe scale is then related to the Ozmidov scale, and dissipation is computed as $\epsilon = 0.64 L_T^2 N^3$. Overturns were computed from potential temperature. Turbulent diffusivity is estimated as $\kappa_\rho = 0.2\epsilon/\bar{N}$ (Osborn, 1980), where 0.2 is the assumed mixing efficiency. Spurious overturns were rejected using criteria from Galbraith and Kelley (1996). The sampling pattern of the MP results in a possibily biased estimate of dissipation. The bias is evaluated by resampling a well-resolved data set at another IWISE mooring (see appendix for details); this suggests the dissipation estimated from the MP is biased high, up to 3 times the actual value.

5.4 Results

5.4.1 Oceanographic Setting and Context

The mooring was located on a peninsular-like slope increasing in depth towards the northwest (Figure 5.1). Barotropic tides in this area are mixed but dominated by the diurnal component, which was nearly rectilinear and oriented towards 60^oT, largely perpendicular to the local slope. The semidiurnal component was smaller but may be important, as it modulates the tidal velocities. Note that the tidal forcing (Figure 5.2a) is asymmetric, with a stronger

north/east flow (ebb) and a weaker south/west flow (flood). Maximum barotropic velocities measured at the mooring were about 25cms^{-1} (Figure 5.2a), giving lateral displacements of approximately 5 km. The bathymetry is mostly supercritical with respect to the diurnal frequency.

5.4.2 Mooring Timeseries

Velocity (Figure 5.2 c) exhibits a strong tidal cycle dominated by beating of the K_1 and O_1 frequencies, as well as low-frequency modulation. Isopycnals also displays a tidal cycle and vertical displacements are largest near 1800m, sometimes exceeding 300m during spring tides. Turbulent dissipation (d) is strongest deeper in the water column and extends to about 700 m off of the bottom, with a large spring-neap cycle. The depth-integrated (below 1400m) dissipation (b) varies by an order of magnitude between spring and neap.

5.4.3 Detailed 2 Day Period

Next we examine a more detailed 2 day section representative of many of the observed events (Figure 5.3). During ebb tide (positive velocity), flow is upslope and isopycnals are lifted. After the flow switches from ebb to flood, flow is downslope and isopycnals drop sharply (209.4) before rebounding (209.5). High levels of dissipation are seen below 1600m during this period. This is followed by a smaller semidiurnal fluctuation of BT velocity (which remains negative), during which higher levels of ϵ are seen closer to the bottom (below 1800m). Note that although the ebb (NE) barotropic velocity is stronger, observed dissipation at the mooring is larger during the flood (SW) tidal flow. In a later section we will show that this is a consequence of the mooring's specific location on the slope.

Qualitatively, the model reproduces the timing of velocity, displacements, and dissipation reasonably well. A more quantitative comparison is made by plotting observed versus model dissipation, depth-integrated from the bottom to 1400m (Figure 5.4). Model data are interpolated onto the same time vector as the observations. Instantaneous values show no clear relationship, indicating that the model is not useful (at least at the resolution used here) for predicting individual profiles of dissipation. When data are averaged with a moving window, the skill of the model increases. It does a reasonable job of predicting 12 hr or 1 day averaged dissipation, likely because the dissipation at this location and depth range is

largely tidally forced. The model dissipation tends to be slightly larger than the observed values.

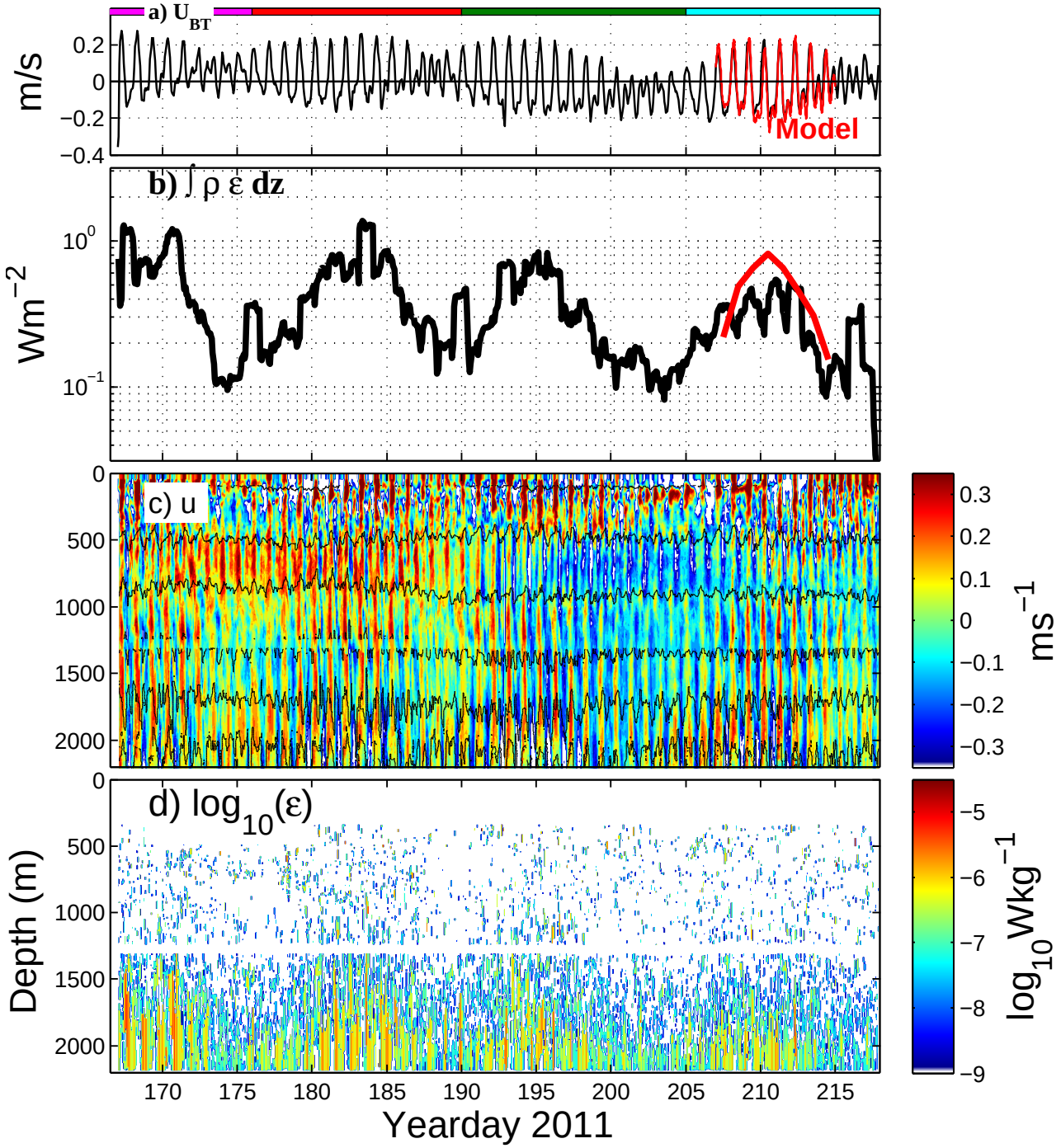

Figure 5.2: Timeseries of data from mooring S9. (a) Barotropic velocity (b) Depth-integrated ϵ. Model data is plotted in red for overlapping time period. (c) Zonal velocity at S9, with isopycnals contoured every 400m. (d) log_{10} of turbulent dissipation rate ϵ.

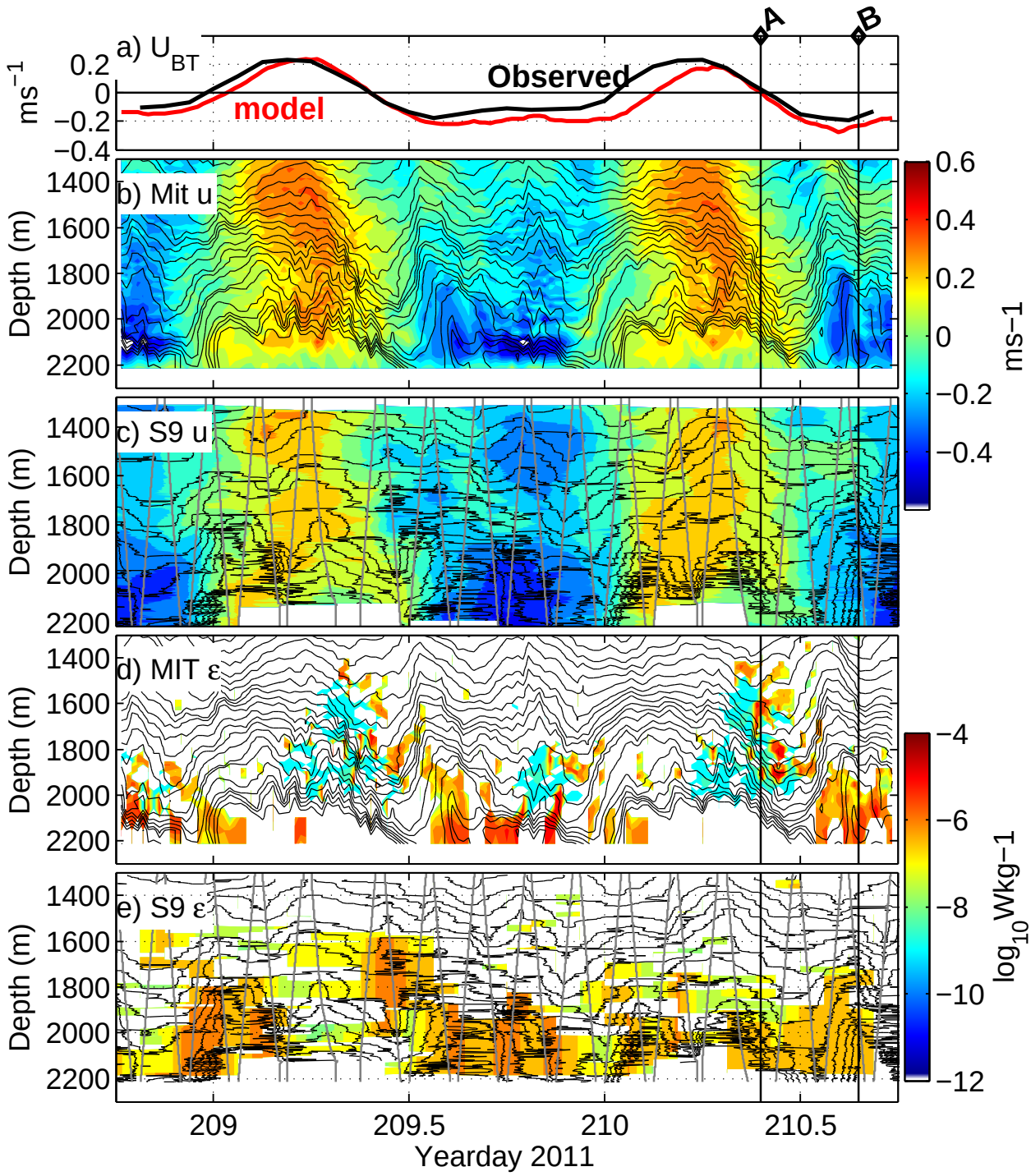

Figure 5.3: Observed and model data from mooring location for a 2 day period. (top) Depth-mean zonal velocity. (b) Model zonal velocity (c) observed zonal velocity (d) model ϵ and (e) observed ϵ. 'A' and 'B' indicate times of spatial transects shown in figures 5.7 and 5.8. Gray lines in panels c and e show the sampling pattern of the profiler. Black lines in b-e are isopycnals.

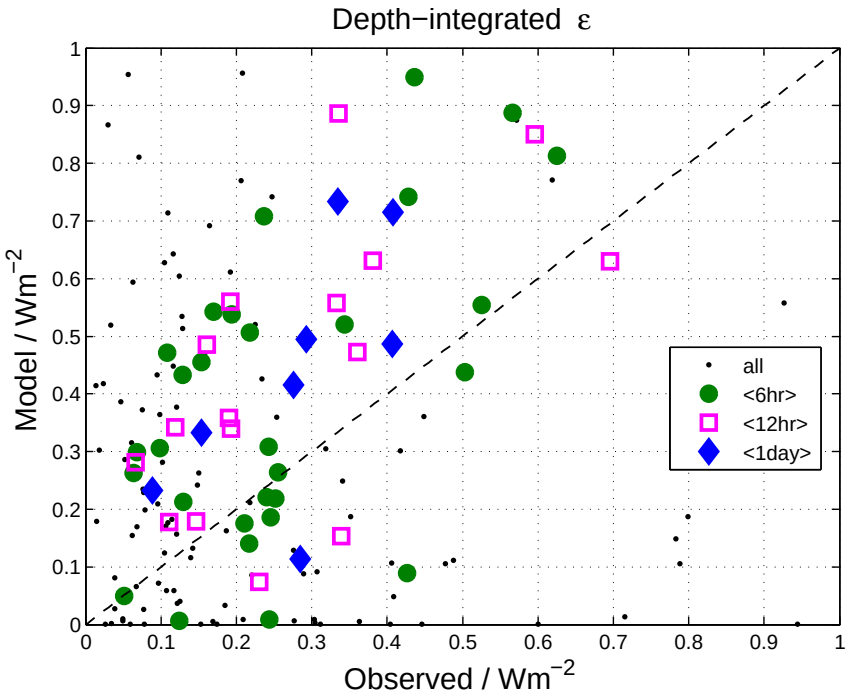

Figure 5.4: Scatter-plot of ϵ depth-integrated between the bottom and 1400m from S9 and model. Colors indicate different averaging periods. Agreement between observations and model improves as averaging time is increased.

5.4.4 Near-Bottom Turbulence Inferred from Temperature

Below the lower range of the MP (2214 m, ∼19 m above bottom), the signature of turbulent events was also observed by two SBE-39 thermistors located 11 and 17 m above the bottom. Although the magnitude of turbulence cannot be quantified from these time series, their faster sampling provides valuable information on the the timing of turbulent events. Temperature fluctuates with the tidal cycle (Figure 5.5), consistent with tidally forced upslope (cooler) and downslope (warmer) flow. During downslope flow, when higher levels of turbulence are observed by the MP, thermistor temperatures show increased fluctuations at higher

frequencies, on top of the smoother tidal displacements. The high-frequency fluctuations are at frequencies above N, consistent with them being turbulence and not high-frequency internal waves. Temperature difference between the two thermistors (not shown) also changes sign during these periods, indicating overturns.

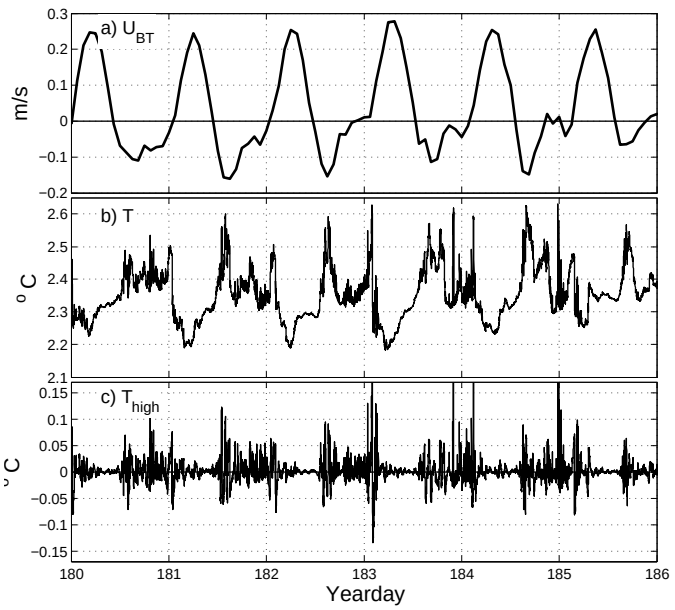

Figure 5.5: (a) Zonal barotropic velocity at S9. (b) Temperature from SBE39 at bottom of mooring S9. (c) Highpass filtered SBE39 temperature, with cutoff at N.

5.4.5 Depth Structure

Time-averaged dissipation increases towards the bottom, reaching a maximum of approximately 10^{-6}Wkg^{-1} in the bottom 200m (Figure 5.6). Model dissipation is slightly larger than observed below 1600m. Average turbulent diffusivity K_ρ is up to $\approx 0.2\text{ms}^{-2}$. This profile is similar to those observed at the Hawaiian Ridge (Klymak et al., 2006) and Luzon Strait (Alford et al., 2011), with dissipation increasing from mid-depth to the bottom. There is also significant temporal variability in the depth structure, as seen in the profiles for the four individual spring tides. Dissipation and diffusivity are larger during the first two spring tides, and smaller during the last two periods.

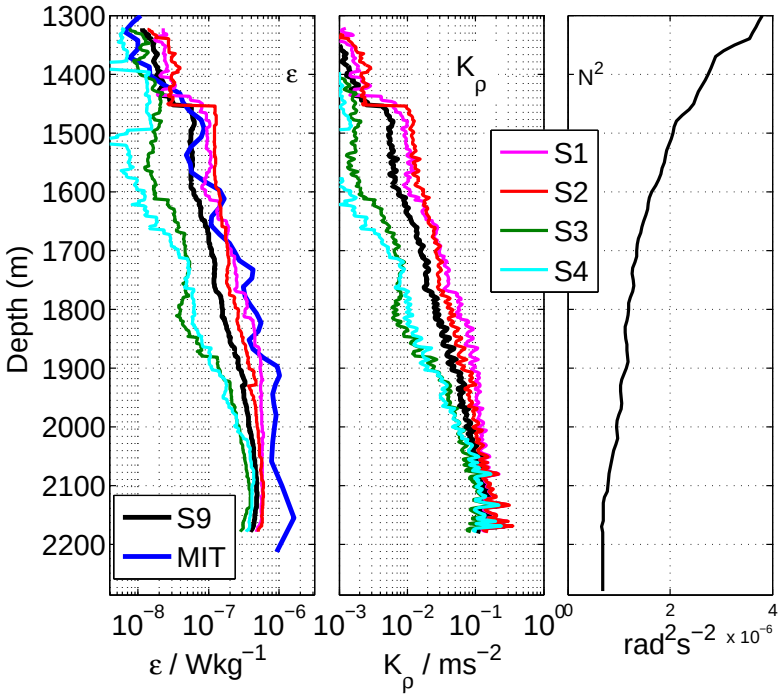

Figure 5.6: Depth profiles of time-averaged (left) ϵ and (middle) turbulent diffusivity κ_ρ. S9 profile for entire record is shown in black. Blue is MITgcm profile. Other colors are profiles for individual spring tides. Mean N^2 profile over the deployment is shown in right panel.

5.4.6 Model Cross Sections

In order to put the moored time series in context and understand the spatial structure of the flow and turbulence, we examine cross-sections of the MITgcm model aligned in the direction of dominant barotropic flow (240^{o}T) and passing through the mooring location. We examine cross-sections at the end of ebb tide ('A') and during maximum flood tide ('B'), at the times indicated in Figure 5.3.

At the end of the ebb period (Figure 5.7), velocity is towards the northeast and a strong, bottom-intensified velocity jet ($> 0.5\text{ms}^{-1}$) forms over the ridge crest. A lee wave is seen forming with isopycnals pushed downwards east of the mooring, forming a trough near $x = 9$km before rebounding sharply at $x = 10$km. During this time period, turbulence is largest just above this jet, near 2000m depth and between $x = 6$ and $x = 10$km where shear is large.

During flood tide (Figure 5.8), barotropic velocity is towards the southwest. Velocities during flood are not as strong as during ebb, with maximum velocity about 0.4ms^{-1} at the top of the slope near S9. A weaker lee wave is seen forming on the west side of the ridge now, with a trough near $x = 4$km, just west of the mooring site. Isopycnals at and around S9 are now stretched vertically (high strain), and turbulence is now strongest below 2000m and between $x = 4$ and $x = 8$. It appears that some turbulence generated during ebb is advected westward by the flood tide. Although the flood tide is weaker than ebb, turbulence at the mooring site is stronger during flood, as also seen in the time series.

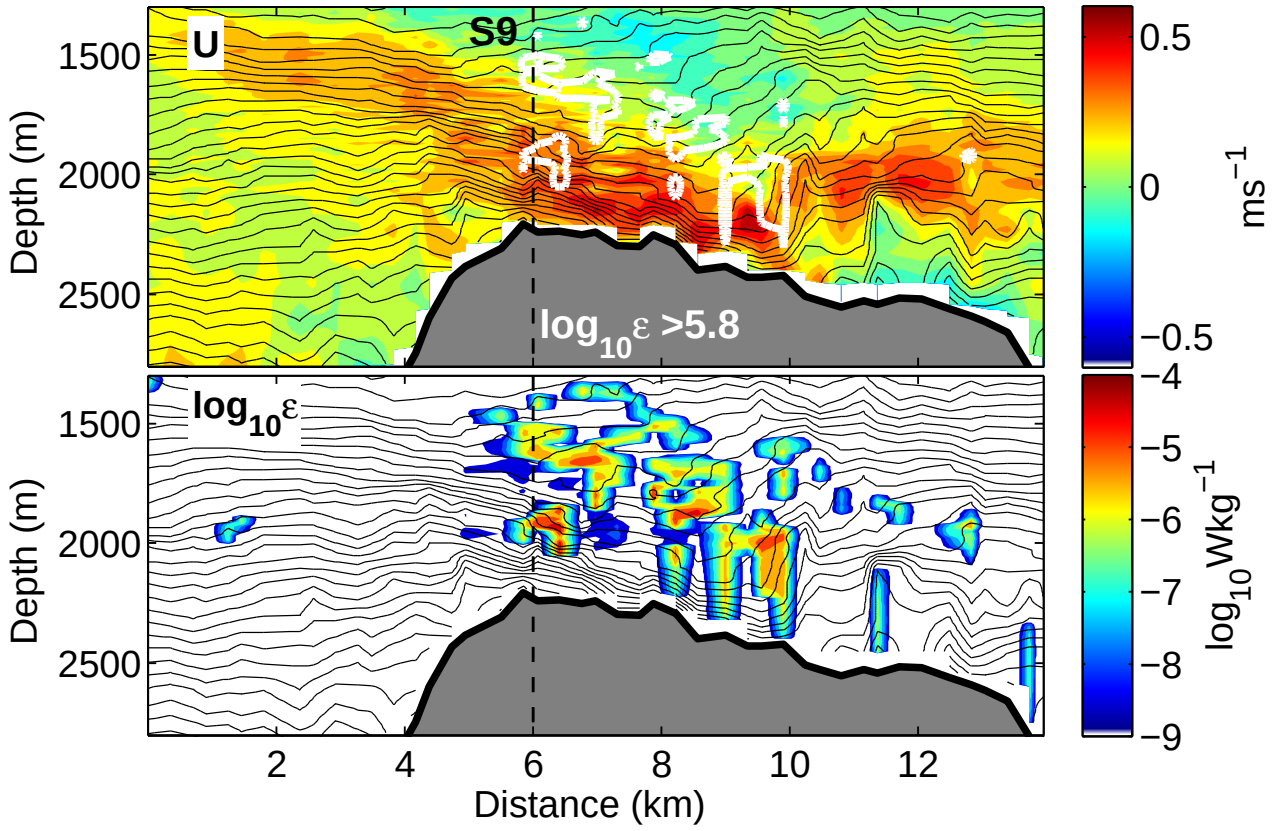

Figure 5.7: Spatial section of along-transect velocity (top panel, towards 240^{o}T), and ϵ (bottom) from MITgcm model transects during period 'A'. In top panel, contours of $log_{10}\epsilon >$ 5.8 are shown in white. Isotherms are contoured in black in both panels. Dashed line indicates location of S9.

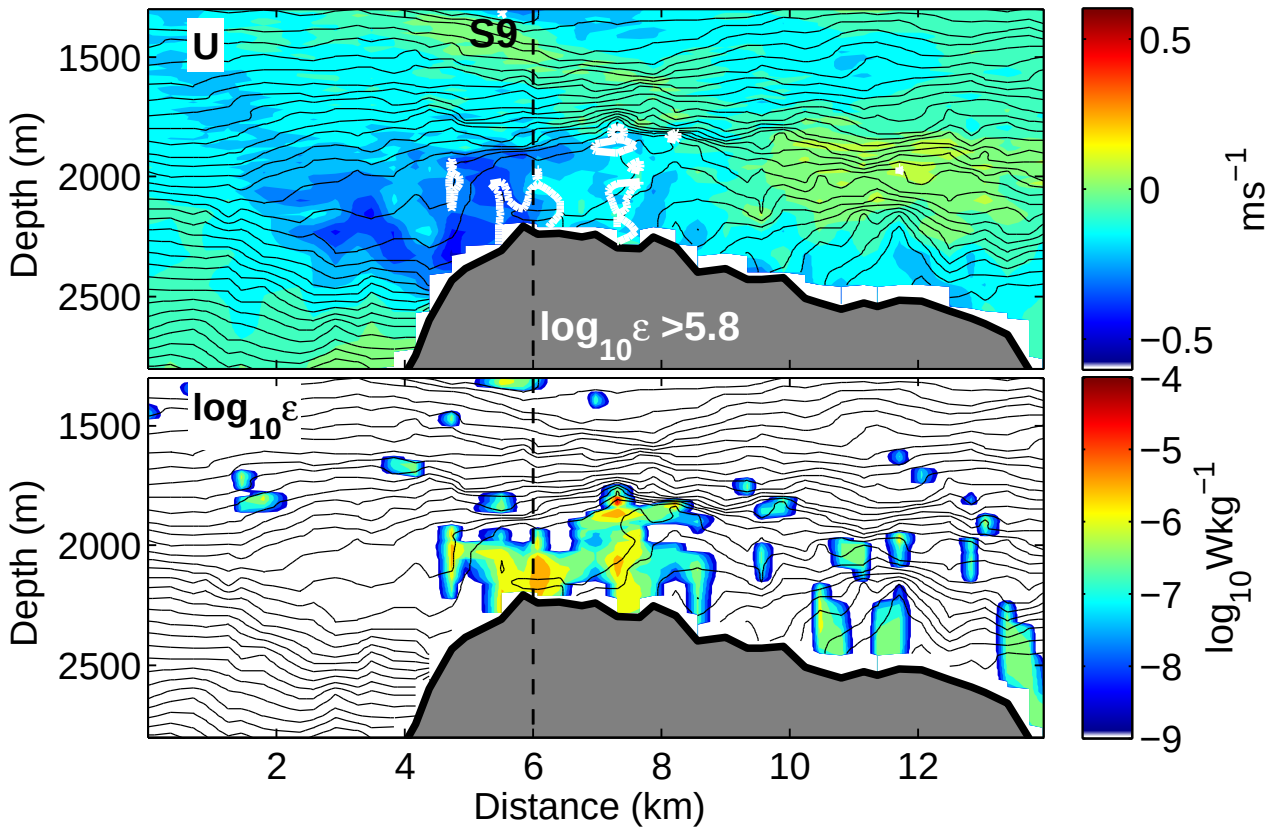

Figure 5.8: Spatial section of along-transect velocity (top panel, towards 240^{o}T), and ϵ (bottom) from MITgcm model transects during period 'B'. In top panel, contours of $log_{10}\epsilon >$ 5.8 are shown in white. Isotherms are contoured in black in both panels.

5.4.7 Spatial Structure of Flow and Dissipation Over the Slope

The model also provides insight into the 3-dimensional nature of flow over the slope. During ebb tide, barotropic velocity is towards the northeast. However, the near-bottom velocity, averaged over the bottom 300m, is steered by the topography (Figure 5.9). Some of the flow encountering steep slopes to the south and west of S9 is deflected north. To the north of S9,

the near-bottom flow is more northward than the barotropic velocity, tending to flow down the topographic gradient. The largest dissipation during this period is east of S9, as was also seen in the model cross section. During flood tide, near-bottom velocity is strong and westward over the shallower areas of the slope. Dissipation is largest over the steep slopes running south of S9. The model predictions agree well with near-bottom velocity measured at S9 during these two periods.

5.4.8 Comparison of Lee Wave Structure to Scaling

Klymak et al. (2010) proposed a scaling for lee waves that applies to flow over supercritical ridges with large topographic inverse Froude number

$$Fr_t^{-1} = \frac{N_o h_{wkb}}{U_o} \tag{5.1}$$

where N_o is the WKB-stretched stratification, U_o is the deep-water tidal velocity, and h_{wkb} is the WKB-stretched ridge height. Using values of $N_o = 0.005$, $h_{wkb} = 2000$m, and $U_o = 0.15\text{ms}^{-1}$ gives an estimated $Fr_t^{-1} \approx 66$, so we expect the scaling to apply here.

According to this scaling, lee waves should have a vertical scale of $\lambda_z \approx 2\pi U_c/N$ (Klymak et al., 2010), where U_c is the speed of tidal flow at the ridge crest and N is the local stratification. Using appropriate values for S9 of $U_c = 0.3(0.4)$m and $N = 0.005\text{s}^{-1}$ gives a vertical scale of $\lambda_z \approx 376(500)$m, which is close to the observed values during flood (ebb) tidal flow. Based on the modal phase speeds at S9, for $U = 0.3$ we would expect modes 12 and higher to be arrested.

5.4.9 Scaling with Barotropic Velocity

Next we examine the relationship of depth-integrated dissipation to the barotropic forcing, which is expected to scale with U_{BT}^3. Turbulent dissipation is vertically integrated between 1400-2300 m depths and averaged over 1 day, then plotted versus the 1-day average magnitude of barotropic velocity (Figure **??**). A least-squares fit with a first-order polynomial of the form

$$log_{10}(\epsilon) = Alog_{10}(U_{BT}) + B \tag{5.2}$$

is performed to determine the power law A that best fits the data. Observed ϵ generally increases with velocity but shows considerable variability. The fit to the entire time series (Figure 5.10) gives a power law of $U^{2.5}$ with an R^2 of 0.49. Model dissipation also increases with velocity, but has much less variability, likely since it is forced with tides only. The fit to

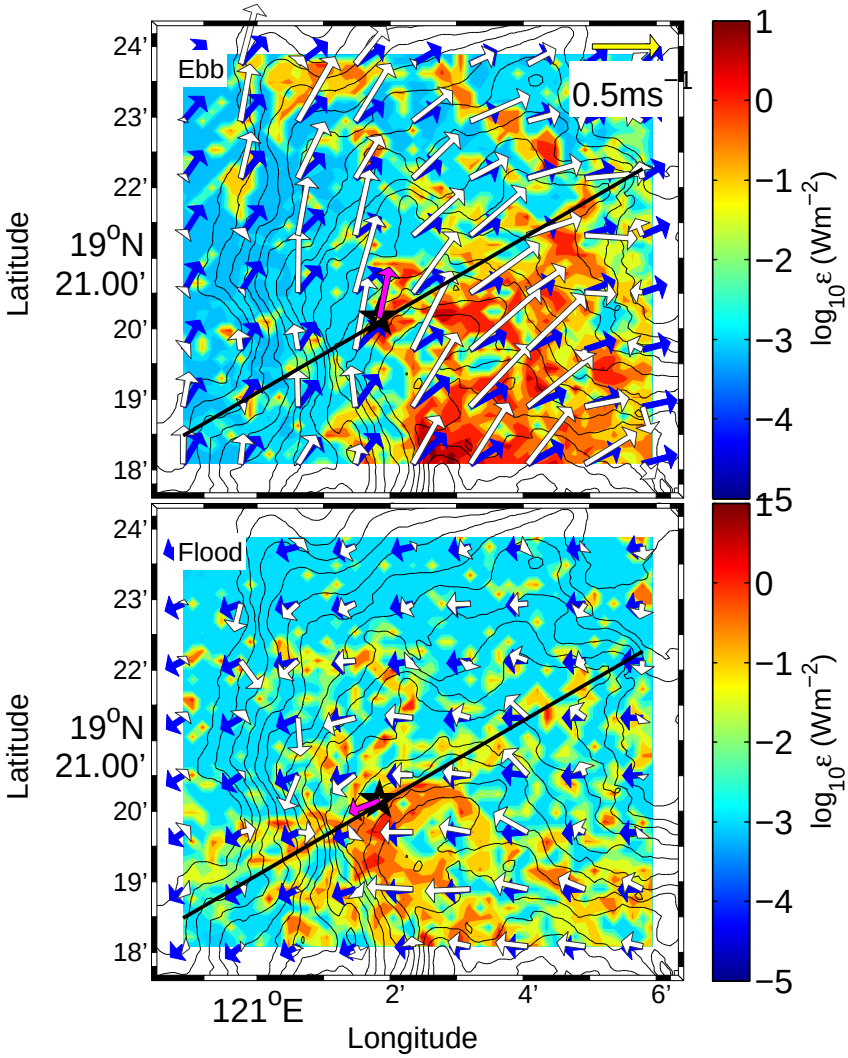

Figure 5.9: Modeled depth-integrated dissipation (colors) , BT velocity (blue), and velocity averaged over the bottom 300m (white) at two times corresponding to model cross sections during flood (top) and ebb (bottom) tide phases. Magenta arrows show near-bottom velocity measured at S9.

model data gives a power law of $U^{3.5}$ and $R^2 = 0.96$. Fits to individual spring tide periods (Figure 5.11), show that there is more variability during the first two springs and less during the last two springs. We discuss this more in the next section.

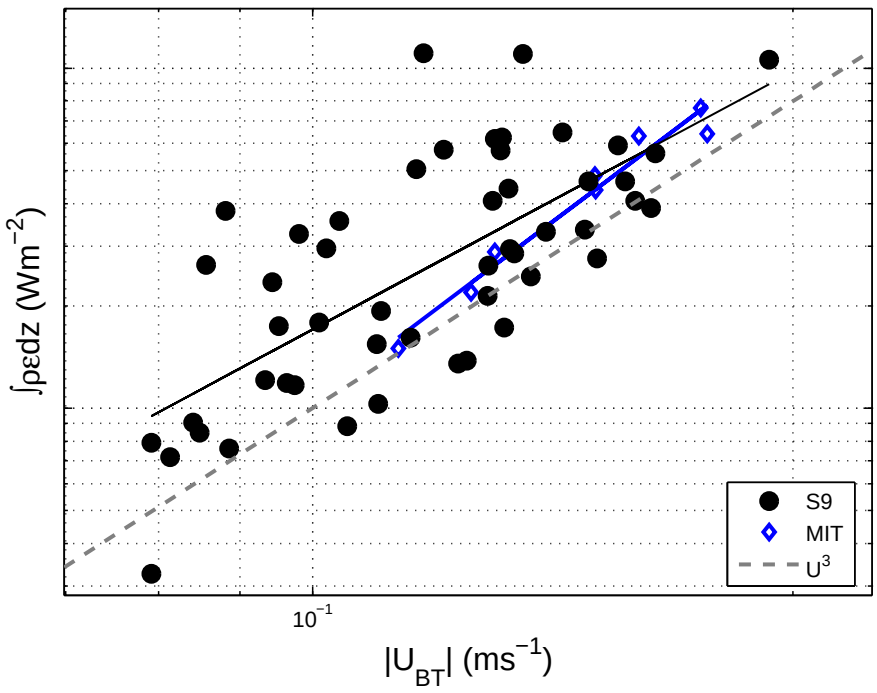

Figure 5.10: Scatter-plot of depth-integrated turbulent dissipation rate ϵ versus barotropic velocity magnitude from S9 (black) and MITgcm model (blue), both averaged with a moving 1 day window. Solid lines show fits with Equation 5.2. Dashed line shows U^3_{BT}.

5.5 Discussion

A novel aspect of this data set is the long time series covering several spring-neap tidal cycles and different mesoscale states, allowing investigation of how tidally forced processes can be influenced on sub-tidal timescales. During the last two spring tides, dissipation scales largely with barotropic velocity and shows little scatter (Figure 5.11). Dissipation during the first two spring tides also scales with U_{bt} but exhibits much more variability/scatter. Profiles of time-mean dissipation during each spring (Figure 5.6) also show that dissipation is larger during the 1st two springs below 1500m. Profiles of stratification are similar during all 4 spring tides (Figure 5.12a), so the changes in dissipation must be due to changes in velocity. To investigate this we examine lowpass filtered velocity during these 4 periods (Figure 5.12 b-d). Meridional velocity in the lower 600m is significantly larger during the 1st two springs, approaching 0.2ms^{-1} near the bottom. Also note that meridional velocity is similar during springs 1 and 2, as well as during springs 3 and 4, the same pattern seen in dissipation profiles. Zonal low-frequency velocity is larger during the 1st spring but smaller in magnitude than the meridional component. Due to the 3D nature of the flow over the slope, it is difficult to predict exactly how low-frequency flows would affect dissipation. In general we would expect dissipation to increase with velocity magnitude. Scaling dissipation with the total velocity (tidal plus mesoscale) over the lower few hundred meters slightly improves R^2 for the first spring tide period (not shown), but it still remains significantly lower. Since the flow and dissipation here is spatially variable, dissipation observed at the mooring may be dependent on flow at different locations. Running more model simulations with varying mesoscale velocity fields could provide more insight.

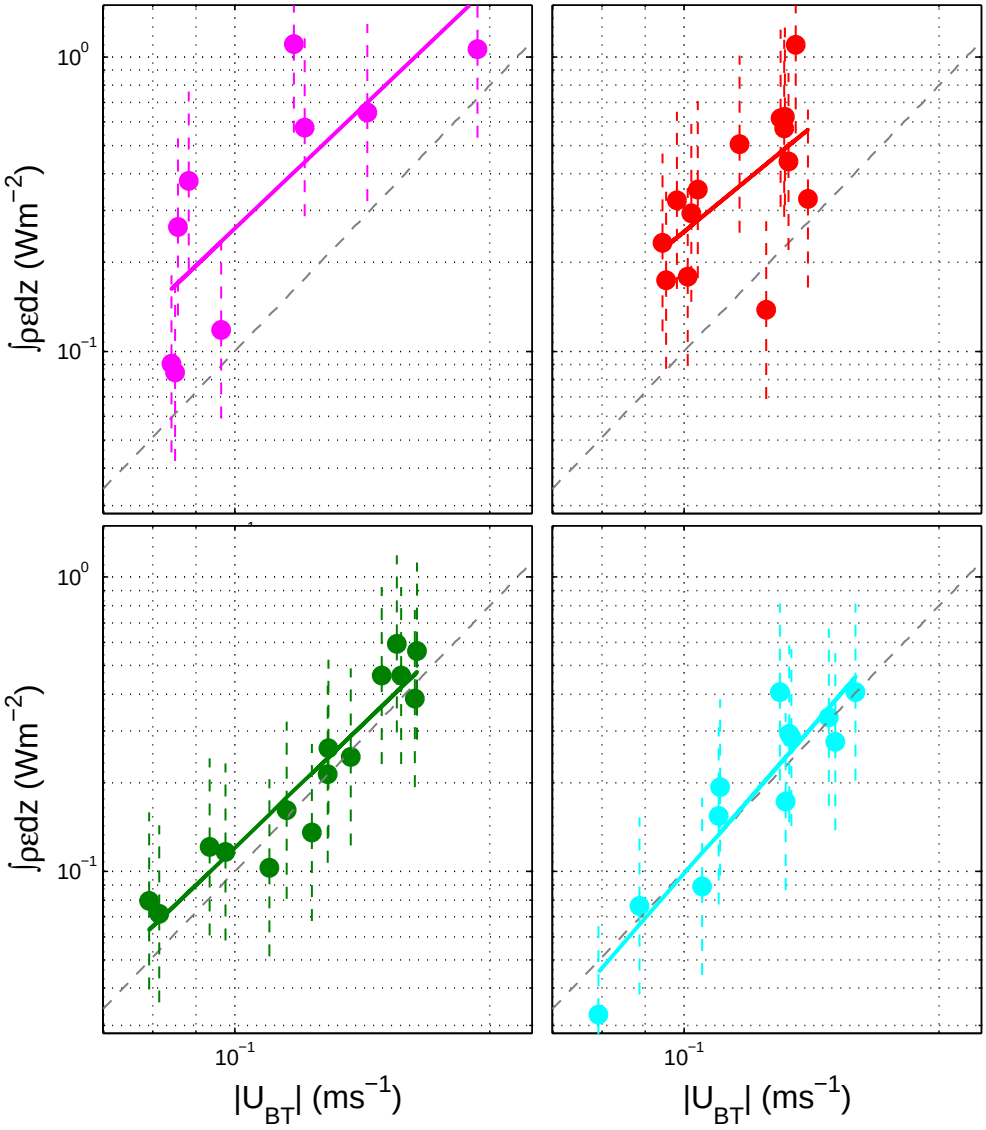

Figure 5.11: Scatter-plot of depth-integrated turbulent dissipation rate ϵ versus barotropic velocity magnitude, both averaged with a moving 1 day window. Each panel/ color of shows data from individual spring tide time periods as indicated in Figure 5.2. Solid lines show fits (Equation 5.2) to each group of data. Vertical dashed lines show estimated errors from T-chain resampling (details in appendix). Dashed line in each panel shows U_{BT}^3. Axis limits are the same for each panel.

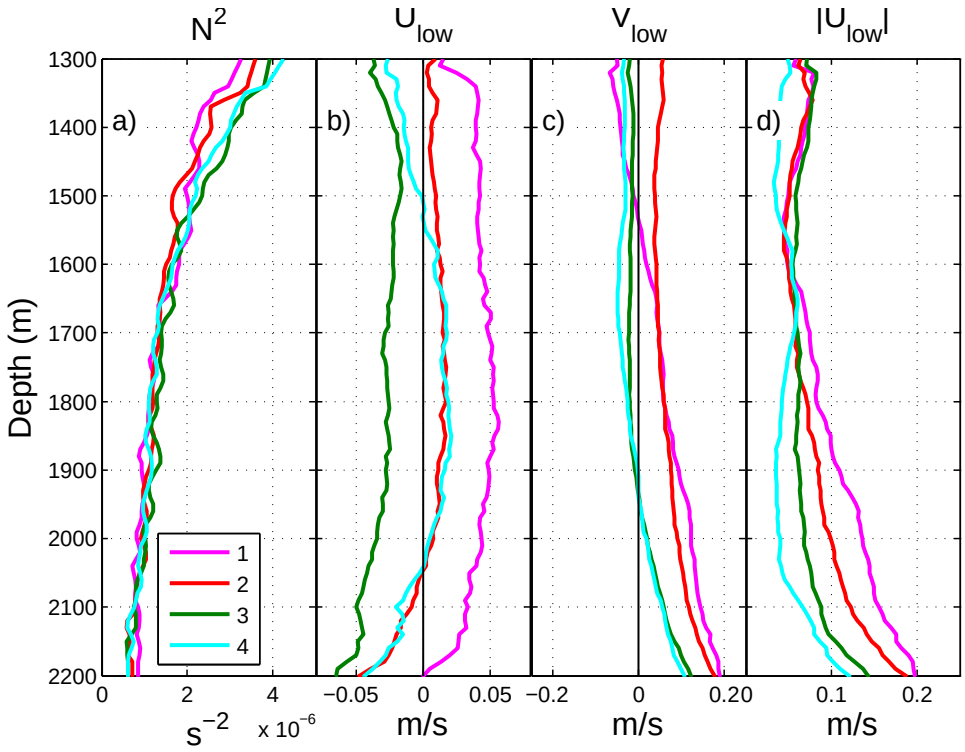

Figure 5.12: Average depth-profiles of a)N^2, b) Low-passed zonal velocity, (c) Low-pass filtered meridional velocity, and (d) low-pass filtered velocity magnitude during four spring tide periods at S9. Color of observed data refers to individual spring tides as indicated in Figure 5.2.

5.6 Conclusions

We have presented temperature, salinity, and velocity measurements from a mooring deployed on a supercritical slope in Luzon Strait for 50 days. Turbulent dissipation is very large and exhibits a spring-neap cycle, varying by an order of magnitude between spring and neap. Dissipation also varies for similar barotropic forcing during different spring tides, suggesting mesoscale effects on mixing. Modeled velocity, displacement, and dissipation from a high resolution 3D MITgcm model simulation agree well with the observations, and are used

to place the mooring observations in context. Model transects confirm that turbulence in the bottom 1000m is largely due to breaking lee waves formed during tidal flow over the slope. The 3D topography influences the tidal flow over the slope, resulting in spatially variable patterns of flow and dissipation that would not be captured in 2D models or parameterizations. Low-frequency velocity varies during the deployment, and is likely responsible for the observed temporal variability in depth-integrated dissipation.

5.7 Acknowledgment

Collaborators on this analysis include Jonathan Nash and Maarten Buijsman, who also provided model data. This work was funded by ONR. We thank the captain crew of the *RV Revelle* and *RV OR1* for their skill and hard work to acquire these measurements. We would also like to thank John Mickett, Eric Boget, Zoe Parsons, Paul Aguilar, Tom Peacock, Hayley Dosser, Ke-shien Fu, and Chung-wei Lu for their work in deploying the moorings.

5.8 Appendix: Effect of MP sampling on overturns

Errors in estimates of dissipation from MPs can arise in several ways. First, the profiler is under sampling the real density field. Second, the profiles that are measured take a finite time, during which isopycnals and overturns may be vertically advected. This will alter the measured overturns size and the corresponding dissipation. To estimate these effects we resampled data from temperature-chain moorings that were highly resolved in time, assuming that overturns computed from the full T-chain data are the true value. This analysis (at another location in Luzon Strait) suggests that dissipation computed from the MP sampling may be biased high by a factor of 2-3 (Figure 5.13). The results are similar for different time periods sampled. We assume it is similar at S9; at both locations turbulence is largely due to tidally-forced lee waves on a supercritical slope.

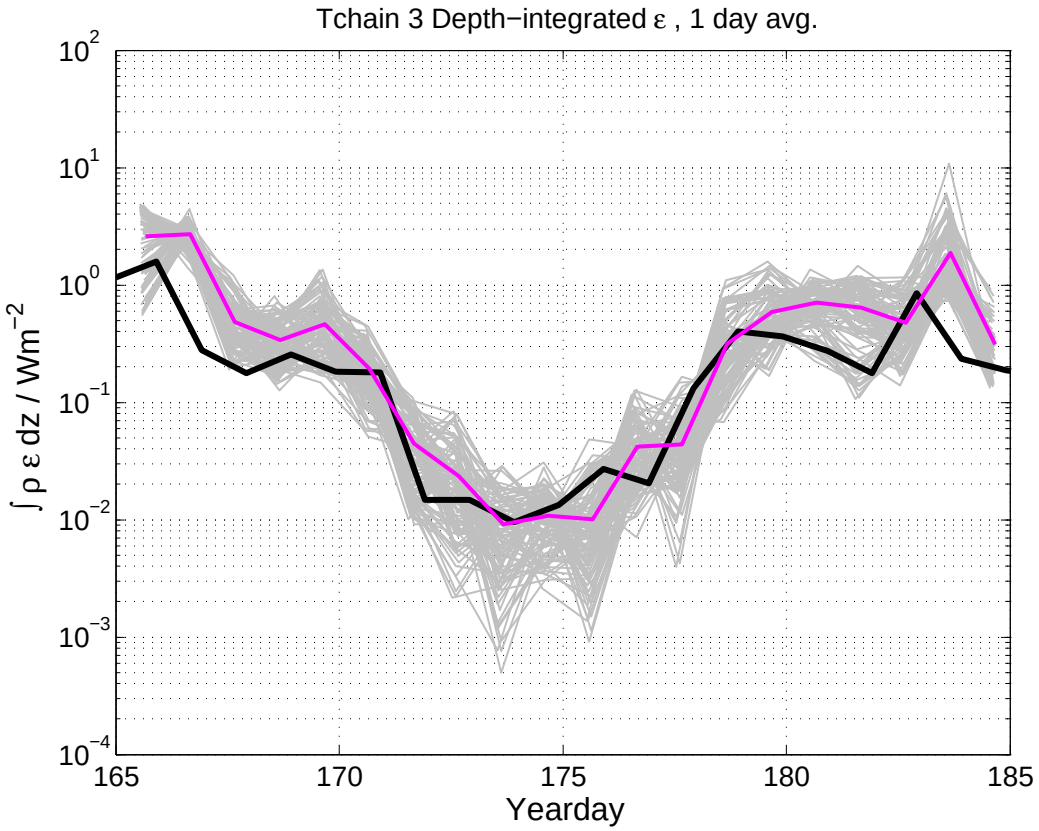

Figure 5.13: Depth-integrated dissipation, averaged over 1 day windows, from T-chain mooring deployed during IWISE. Thick black line is true value from all data. Gray lines are computed using resampled data designed to represent MP sampling. Magenta is the mean of resampled values.

BIBLIOGRAPHY

Alford, M. H., 2001a: Fine structure contamination: Observations and a model of a simple two-wave case. *J. Phys. Oceanogr.*, **9**, 2645–2649.

Alford, M. H., 2001b: Internal swell generation: The spatial distribution of energy flux from the wind to mixed-layer near-inertial motions. *J. Phys. Oceanogr.*, **31 (8)**, 2359–2368.

Alford, M. H., 2003a: Energy available for ocean mixing redistributed through long-range propagation of internal waves. *Nature*, **423**, 159–163.

Alford, M. H., 2003b: Improved global maps and 54-year history of wind-work on ocean inertial motions. *Geophys. Res. Lett.*, **30 (8)**, 1424–1427.

Alford, M. H., 2010: Sustained, full-water-column observations of internal waves and mixing near Mendocino Escarpment. *J. Phys. Oceanogr.*, **40 (12)**, 2643–2660, doi: 10.1175/2010JPO4502.1.

Alford, M. H. and M. C. Gregg, 2001: Near-inertial mixing: Modulation of shear, strain and microstructure at low latitude. *J. Geophys. Res.*, **106 (C8)**, 16 947–16 968.

Alford, M. H., J. M. Klymak, and G. S. Carter, 2014: Breaking internal lee waves at Kaena Ridge, Hawaii. *Geophys. Res. Lett.*, **41**, 906–912.

Alford, M. H., J. A. MacKinnon, Z. Zhao, R. Pinkel, J. Klymak, and T. Peacock, 2007: Internal waves across the Pacific. *Geophys. Res. Lett.*, **34 (L24601)**, doi:10.1029/2007GL031 566.

Alford, M. H., A. Y. Shcherbina, and M. C. Gregg, 2013: Observations of near-inertial internal gravity waves radiating from a frontal jet. *J. Phys. Oceanogr.*, **43 (6)**, 1225–1239.

Alford, M. H. and M. Whitmont, 2007: Seasonal and spatial variability of near-inertial kinetic energy from historical moored velocity records. *J. Phys. Oceanogr.*, **37 (8)**, 2022–2037.

Alford, M. H., et al., 2011: Energy flux and dissipation in Luzon Strait: Two tales of two ridges. *J. Phys. Oceanogr.*, **41 (11)**, 2211–2222.

Althaus, A., E. Kunze, and T. Sanford, 2003: Internal tide radiation from Mendocino Escarpment. *J. Phys. Oceanogr.*, **33 (7)**, 1510–1527.

Arbic, B., et al., 2009: Estimates of bottom flows and bottom boundary layer dissipation of the oceanic general circulation from global high-resolution models. *Journal of Geophysical Research*, **114 (C2)**, C02 024.

Aucan, J., M. A. Merrifield, D. S. Luther, and P. Flament, 2006: Tidal mixing events on the deep flanks of Kaena ridge, Hawaii. *J. Phys. Oceanogr.*, **36 (6)**, 1202–1219.

Buijsman, M., et al., 2014: Three-Dimensional Double-Ridge Internal Tide Resonance in Luzon Strait. *J. Phys. Oceanogr.*, **44 (3)**, 850–869.

Buijsman, M. C., J. M. Klymak, and S. Legg, 2012: Double Ridge Internal Tide Interference and its Effect on Dissipation in Luzon Strait. *J. Phys. Oceanogr.*, **42 (8)**, 1337–1356.

Cairns, J. L. and G. O. Williams, 1976: Internal wave observations from a midwater float, 2. *J. Geophys. Res.*, **81**, 1943–1950.

Carter, G. S. and M. C. Gregg, 2006: Persistent near-diurnal internal waves observed above a site of M2 barotropic-to-baroclinic conversion. *J. Phys. Oceanogr.*, **36 (6)**, 1136–1147.

Chen, Y.-J., D. Shan Ko, and P.-T. Shaw, 2013: The generation and propagation of internal solitary waves in the south china sea. *Journal of Geophysical Research: Oceans*, **118 (12)**, 6578–6589.

Cole, S. T., D. L. Rudnick, B. A. Hodges, and J. P. Martin, 2009: Observations of tidal internal wave beams at Kauai Channel, Hawaii. *J. Phys. Oceanogr.*, **39**, 421–436.

D'Asaro, E., 1985: The energy flux from the wind to near-inertial motions in the mixed layer. *J. Phys. Oceanogr.*, **15**, 943–959.

D'Asaro, E. and H. Perkins, 1984: A near-inertial internal wave spectrum for the Sargasso Sea in late summer. *J. Phys. Oceanogr.*, **14 (3)**, 489–505.

D'Asaro, E. A., 1989: The decay of wind-forced mixed layer inertial oscillations due to the β effect. *J. Geophys. Res.*, **94 (C2)**, 2045–2056.

D'Asaro, E. A., C. E. Eriksen, M. D. Levine, P. Niiler, C. A. Paulson, and P. V. Meurs, 1995: Upper-ocean inertial currents forced by a strong storm, part I, Data and comparisons with linear theory. *J. Phys. Oceanogr.*, **25**, 2909–2936.

Dillon, T. M., 1982: Vertical overturns: A comparison of Thorpe and Ozmidov length scales. *J. Geophys. Res.*, **87**, 9601–9613.

Doherty, K., D. Frye, S. Liberatore, and J. Toole, 1999: A moored profiling instrument. *J. Atmos. Ocean. Tech.*, **16**, 1816–1829.

Egbert, G. and S. Erofeeva, 2002: Efficient inverse modeling of barotropic ocean tides. *J. Atmos. Ocean. Tech.*, **19**, 183–204.

Egbert, G. D. and R. D. Ray, 2003: Semi-diurnal and diurnal tidal dissipation from TOPEX/Poseidon altimetry. *Geophys. Res. Lett.*, **30**, 1907, doi:10.1029/2003GL017676, URL `http://dx.doi.org/10.1029/2003GL017676`.

Farmer, D., Q. Li, and Jae-Hun Park, 2009: Internal wave observations in the South China Sea: the role of rotation and nonlinearity. *Atmos.-Ocean.*, **47**, 267–280.

Furuichi, N., T. Hibiya, and Y. Niwa, 2008: Model predicted distribution of wind-induced internal wave energy in the world's oceans. *J. Geophys. Res.*, **113 (C09034)**, doi:10.1029/2008JC004768.

Galbraith, P. S. and D. E. Kelley, 1996: Identifying overturns in CTD profiles. *J. Atmos. Ocean. Tech.*, **13**, 688–702.

Garrett, C. and E. Kunze, 2006: Internal tide generation in the deep ocean. *Ann. Rev. Fluid Mech.*, **1**, 1056–8700/97/0610–00.

Garrett, C. and W. Munk, 1972: Space-time scales of internal waves. *Geophys. Fluid Dyn.*, **3**, 225–264.

Garrett, C. J. R. and W. H. Munk, 1975: Space-time scales of internal waves: A progress report. *J. Geophys. Res.*, **80 (3)**, 291–297.

Hebert, H. and J. Moum, 1994: Decay of a near-inertial wave. *J. Phys. Oceanogr.*, **24 (11)**, 2334–2351.

Jan, S., R. Lien, and C. Ting, 2008: Numerical study of baroclinic tides in Luzon Strait. *Journal of Oceanography*, **64 (5)**, 789–802.

Jayne, S. R., 2009: The impact of abyssal mixing parameterizations in an ocean general circulation model. *J. Phys. Oceanogr.*, **39**, 1756—1775.

Jiang, J., Y. Lu, and W. Perrie, 2005: Estimating the energy flux from the wind to ocean inertial motions: The sensitivity to surface wind fields. *Geophys. Res. Lett.*, **32 (L15610)**, doi:10.1029/2005GL023 289.

Kalnay, E. M., et al., 1996: The NCEP/NCAR 40-year reanalysis project. *Bulletin of the American Meteorological Society*, **77**, 437–471.

Kelly, S. and J. D. Nash, 2010: Internal-tide generation and destruction by shoaling internal tides. *Geophys. Res. Lett.*, **37 (L23611)**, doi:doi:10.1029/2010GL045598.

Kerry, C. G., B. S. Powell, and G. S. Carter, 2013: Effects of Remote Generation Sites on Model Estimates of M2 Internal Tides in the Philippine Sea. *Journal of Physical Oceanography*, **43**, 187–204.

Kerry, C. G., B. S. Powell, and G. S. Carter, 2014: The impact of sub-tidal circulation on internal tide generation and propagation in the philippine sea. *Journal of Physical Oceanography*, **(2014)**.

King, B. A., E. Firing, and T. M. Joyce, 2001: Shipboard observations during WOCE. *International Geophysics*, **77**, 99–122.

Klymak, J. M., M. H. Alford, R. Pinkel, R. C. Lien, and Y. J. Yang, 2011: The breaking and scattering of the internal tide on a continental slope. *J. Phys. Oceanogr.*, **41 (5)**, 926–945, doi:10.1175/2010JPO4500.1.

Klymak, J. M., S. Legg, and R. Pinkel, 2010: A simple parameterization of turbulent tidal mixing near supercritical topography. *J. Phys. Oceanogr.*, **40 (9)**, 2059–2074, doi:10.1175/2010JPO4396.1, `http://journals.ametsoc.org/doi/pdf/10.1175/2010JPO4396.1`.

Klymak, J. M. and S. M. Legg, 2010: A simple mixing scheme for models that resolve breaking internal waves. *Ocean Modell.*, **33 (3-4)**, 224 – 234, doi:10.1016/j.ocemod.2010.02.005.

Klymak, J. M., R. Pinkel, and L. Rainville, 2008: Direct breaking of the internal tide near topography: Kaena Ridge, Hawaii. *J. Phys. Oceanogr.*, **38**, 380–399.

Klymak, J. M., et al., 2006: An estimate of tidal energy lost to turbulence at the Hawaiian Ridge. *J. Phys. Oceanogr.*, **36 (6)**, 1148–1164.

Ko, D. S., S.-Y. Chao, P. Huang, and S. F. Lin, 2009: Anomalous Upwelling in Nan Wan: July 2008. *Terrestrial, Atmospheric & Oceanic Sciences*, **20 (6)**.

Ko, D. S., P. J. Martin, C. D. Rowley, and R. H. Preller, 2008: A real-time coastal ocean prediction experiment for mrea04. *Journal of Marine Systems*, **69 (1)**, 17–28.

Kunze, E., L. Rosenfield, G. Carter, and M. C. Gregg, 2002: Internal waves in Monterey Submarine Canyon. *J. Phys. Oceanogr.*, **32**, 1890–1913.

Leaman, K. D. and T. B. Sanford, 1975: Vertical energy propagation of inertial waves: A vector spectral analysis of velocity profiles. *J. Geophys. Res.*, **80 (15)**, 1975–1978.

Lee, C. M., E. Kunze, T. B. Sanford, J. D. Nash, M. A. Merrifield, and P. E. Holloway, 2006: Internal tides and turbulence along the 3000-m isobath of the Hawaiian Ridge with model comparisons. *J. Phys. Oceanogr.*, **36 (6)**, 1165–1183.

Legg, S. and J. M. Klymak, 2008: Internal hydraulic jumps and overturning generated by tidal flow over a tall steep ridge. *J. Phys. Oceanogr.*, **38 (9)**, 1949–1964.

Levine, M. D. and T. J. Boyd, 2006: Tidally forced internal waves and overturns observed on a slope: Results from HOME. *J. Phys. Oceanogr.*, **36 (6)**, 1184–1201.

Levitus, S. and T. Boyer, 1994: *World Ocean Atlas 1994*. NOAA Atlas NESDIS 4, U.S. Department of Commerce, Washington, D.C.

Levitus, S. and T. Boyer, 2001: *World Ocean Atlas 2001*. NOAA Atlas NESDIS 4, U.S. Department of Commerce, Washington, D.C.

Li, Q. and D. Farmer, 2011: The generation and evolution of nonlinear internal waves in the deep basin of the South China Sea. *Journal of Physical Oceanography*, **41**, 1345–1363.

Lien, R.-C., F. Henyey, B. Ma, and Y.-J. Yang, 2014: Large-amplitude internal solitary waves observed in the northern South China Sea: Properties and energetics. *J. Phys. Oceanogr.*, **44 (4)**, 1095–1115.

Ma, B. B., R.-C. Lien, and D. S. Ko, 2013: The variability of internal tides in the Northern South China Sea. *Journal of oceanography*, **69 (5)**, 619–630.

MacKinnon, J. A., M. H. Alford, O. Sun, R. Pinkel, Z. Zhao, and J. Klymak, 2013: Parametric Subharmonic Instability of the internal tide at 29N. *J. Phys. Oceanogr.*, **43 (1)**, 17–28.

MacKinnon, J. A. and K. B. Winters, 2005: Subtropical catastrophe: significant loss of low-mode tidal energy at 28.9^o. *Geophys. Res. Lett.*, **32 (L15605)**, doi:10.1029/2005GL023 376.

Martin, J. P. and D. L. Rudnick, 2007: Inferences and observations of turbulent dissipation and mixing in the upper ocean at the Hawaiian Ridge. *J. Phys. Oceanogr.*, **37 (3)**, 476–494.

Martin, J. P., D. L. Rudnick, and R. Pinkel, 2006: Spatially broad observations of internal waves in the upper ocean at the hawaiian ridge. *J. Phys. Oceanogr.*, **36 (6)**, 1085–1103.

Melet, A., R. Hallberg, S. Legg, and M. Nikurashin, 2013a: Sensitivity of the ocean state to lee wave–driven mixing. *Journal of Physical Oceanography*, **44 (3)**, 900–921, doi:10.1175/JPO-D-13-072.1.

Melet, A., R. Hallberg, S. Legg, and K. L. Polzin, 2013b: Sensitivity of the ocean state to the vertical distribution of internal-tide-driven mixing. *J. Phys. Oceanogr.*, **43 (3)**, 602–615, doi:http://dx.doi.org/10.1175/JPO-D-12-055.1.

Merrifield, M. and P. Holloway, 2002: Model estimates of M2 internal tide energetics at the Hawaiian Ridge. *J. Geophys. Res.*, **107**, 10.1029/2001JC000 996.

Moore, S. and R.-C. Lien, 2007: Pilot whales follow internal solitary waves in the South China Sea. *Marine Mammal Science*, **23 (1)**, 193–196.

Müller, P., G. Holloway, F. Henyey, and N. Pomphrey, 1986: Nonlinear interactions among internal gravity waves. *Rev. Geophys*, **24 (3)**, 493–536.

Munk, W. and C. Wunsch, 1998: Abyssal recipes II: energetics of tidal and wind mixing. *Deep-Sea Res. Part I*, **45**, 1977–2010.

Nash, J. D., M. H. Alford, and E. Kunze, 2005: Estimating internal-wave energy fluxes in the ocean. *J. Atmos. Ocean. Tech.*, **22 (10)**, 1551–1570.

Nash, J. D., S. M. Kelly, E. L. Shroyer, J. N. Moum, and T. F. Duda, 2012: The unpredictable nature of internal tides and nonlinear waves on the continental shelf. *J. Phys. Oceanogr.*, **42 (11)**, 1981–2000.

New, A. and R. Pingree, 1992: Local generation of internal soliton packets in the central bay of biscay. *Deep Sea Research Part A. Oceanographic Research Papers*, **39 (9)**, 1521–1534.

Nikurashin, M. and R. Ferrari, 2010: Radiation and dissipation of internal waves generated by geostrophic motions impinging on small-scale topography: Theory. *J. Phys. Oceanogr.*, **40 (5)**, 1055–1074, doi:10.1175/2009JPO4199.1, URL `http://journals.ametsoc.org/doi/abs/10.1175/2009JPO4199.1`, `http://journals.ametsoc.org/doi/pdf/10.1175/2009JPO4199.1`.

Osborn, T. R., 1980: Estimates of the local rate of vertical diffusion from dissipation measurements. *J. Phys. Oceanogr.*, **10**, 83–89.

Park, J.-H. and D. M. Farmer, 2014: Effects of Kuroshio intrusions on nonlinear internal waves in the South China Sea during winter. *J. Geophys. Res.*, **in press**.

Pickering, A. I. and M. H. Alford, 2012: Velocity structure of internal tide beams emanating from Kaena Ridge, Hawaii. *J. Phys. Oceanogr.*, **42 (6)**, 1039–1044.

Pinkel, R., 1985: A wavenumber-frequency spectrum of upper ocean shear. *J. Phys. Oceanogr.*, **15**, 1453–1569.

Pollard, R. T. and R. C. Millard, 1970: Comparison between observed and simulated wind-generated inertial oscillations. *Deep-Sea Res.*, **17**, 153–175.

Rainville, L., T. M. S. Johnston, G. S. Carter, M. A. Merrifield, R. Pinkel, B. D. Dushaw, and P. Worcester, 2010: Interference pattern and propagation of the M_2 internal tide south of the Hawaiian Ridge. *J. Phys. Oceanogr.*, **40 (2)**, 311–325.

Rainville, L. and R. Pinkel, 2006a: Baroclinic energy flux at the Hawaiian ridge: Observations from the R/P FLIP. *J. Phys. Oceanogr.*, **36 (6)**, 1104–1122.

Rainville, L. and R. Pinkel, 2006b: Propagation of low-mode internal waves through the ocean. *J. Phys. Oceanogr.*, **36**, 1220–1236.

Ramp, S. R., et al., 2004: Internal solitons in the northeastern South China Sea, part I: sources and deep water propagation. *IEEE J. of Oceanic Engr.*, **29 (4)**, 1157–1181.

Ray, R. and E. Zaron, 2011: Non-stationary internal tides observed with satellite altimetry. *Geophysical Research Letters*, **38 (17)**, L17 609.

Riedel, K. S. and A. Sidorenko, 1995: Minimum bias multiple taper spectral estimation. *IEEE Transactions on Signal Processing*, **43 (1)**, 188–195.

Rudnick, D., et al., 2003: From tides to mixing along the Hawaiian Ridge. *Science*, **301**, 355–357.

Silverthorne, K. E. and J. M. Toole, 2009: Seasonal kinetic energy variability of near-inertial motions. *J. Phys. Oceanogr.*, **39 (4)**, 1035–1049.

Simmons, H., 2004: A study of internal wave generation, evolution and propagation in a global baroclinic ocean model.

Simmons, H., 2008: Spectral modification and geographic redistribution of the semi-diurnal internal tide. *Ocean Modelling*, **21**, 126–138.

Simmons, H. L., R. W. Hallberg, and B. K. Arbic, 2004: Internal wave generation in a global baroclinic tide model. *Deep-Sea Res II*, **51**, 3043–3068.

Thorpe, S., 1977: Turbulence and mixing in a Scottish Loch. *Philos. Trans. R. Soc. London Ser. A*, **286**, 125–181.

Wang, Y. H., C. F. Dai, and Y. Y. Chen, 2007: Physical and ecological processes of internal waves on an isolated reef ecosystem in the South China Sea. *Geophys. Res. Lett.*, **34**, doi:10.1029/2007GL030658.

Watanabe, M. and T. Hibiya, 2002: Global estimates of the wind-induced energy flux to inertial motions in the surface mixed layer. *Geophys. Res. Lett.*, **29 (8)**, 10.1029/2001GL014 422.

Weller, R. A., 1982: The relation of near-inertial motions observed in the mixed layer during the JASIN (1978) experiment to the local wind stress and to the quasi-geostrophic flow field. *J. Phys. Oceanogr.*, **12**, 1122–1136.

Wunsch, C. and R. Ferrari, 2004: Vertical mixing, energy and the general circulation of the oceans. *Ann. Rev. Fluid Mech.*, **36**, 281–314.

Zhao, Z., 2014: Internal tide radiation from the luzon strait. *Journal of Geophysical Research: Oceans*.

Zhao, Z., M. H. Alford, J. A. MacKinnon, and R. Pinkel, 2010: Long-range propagation of the semidiurnal internal tide from the Hawaiian Ridge. *J. Phys. Oceanogr.*, **40 (4)**, 713–736, doi:10.1175/2009JPO4207.1.

Zilberman, N. V., M. A. Merrifield, G. S. Carter, D. S. Luther, M. D. Levine, and T. J. Boyd, 2011: Incoherent nature of m2 internal tides at the hawaiian ridge. *J. Phys. Oceanogr.*, **41 (11)**, 2021–2036, doi:10.1175/JPO-D-10-05009.1, URL `http://dx.doi.org/10.1175/JPO-D-10-05009.1`.